

POLITECNICO DI TORINO

**Corso di Laurea Magistrale
in Ingegneria Civile**

Tesi di Laurea Magistrale

**Moment-Rotation behaviour of
shallow foundations on liquefiable soils**



Relatore:

Prof. Sebastiano Foti

Correlatori:

Prof. Antonio Viana da Fonseca

Dott. Maxim Millen

Candidato:

Martina Argeri

Luglio 2018

Table of Contents

1. Chapter: Abstract.....	7
2. Chapter: Literature review.....	9
2.1 Phenomena.....	10
2.2 Effects of liquefaction.....	14
Settlements.....	15
Tilting.....	17
2.3 Soil-Foundation-Structure Interaction (SFSI).....	19
2.4 SFSI modelling approaches.....	21
3. Chapter: PLAXIS 2D Model validation for Ultimate Bearing Capacity of Shallow Foundations.....	23
3.1 Introduction.....	23
3.2 Literature review.....	24
Bearing Capacity of shallow foundations on homogeneous soil.....	24
Bearing Capacity of shallow foundations on layered deposit.....	25
3.3 Model validation.....	27
Model inputs.....	27
Model construction.....	28
Running of the Model.....	31
Homogeneous sandy soil results.....	32
Verification of the sandy soil results.....	33
Model verification for clayey soil.....	34
3.4 Bearing Capacity of shallow foundations on a deposit with a liquefied soil layer underlaying a crust.....	36
Verification.....	41
3.5 Conclusions.....	42
4. Chapter: Moment-Rotation response of shallow foundations.....	45
4.1 Introduction.....	45
4.2 Literature review.....	47

Case 1: Elastic soil and no-tension interface	48
Case 2: Inelastic (cohesive) soil and no-tension interface.....	49
The ultimate moment capacity	50
4.3 Model Validation: No tension interface and linear elastic deposit	51
Model inputs	51
Model construction	52
Model execution	53
Output inspection.....	54
Numerical results.....	56
Verification.....	57
4.4 Moment-rotation response of a footing on a homogeneous inelastic soil: Cohesive material (clay)	59
Model inputs	59
Model construction	60
Model execution	60
Numerical results.....	62
4.5 Moment-rotation response of a footing on a homogeneous inelastic soil: frictional material (clean sand).....	67
Model inputs	67
Model construction	68
Model execution	68
Numerical results.....	70
4.6 Moment-rotation response of a shallow foundation on layered deposit	74
Model inputs	77
Model construction	78
Model execution	78
Numerical results.....	82
4.7 Conclusions	96
5. Chapter: Case Study	99
5.1 Introduction.....	99
5.2 Case study inputs	99

5.3 Estimation of the structure response	103
Calculation.....	103
5.4 Push-Over Analyses	107
Numerical Modelling.....	107
Numerical results.....	113
5.5 Dynamic numerical simulations.....	115
Ground motions selection.....	115
Numerical modelling	117
UBC3D-PLM soil model.....	119
Definition of the Rayleigh damping	122
Mesh definition.....	123
5.6 Dynamic analyses results	123
No Liquefaction.....	124
Liquefaction.....	127
Comparison between the no liquefaction and the liquefaction cases	130
5.7 Conclusions	132
6. Chapter: Final conclusions	133
7. References	137

Acknowledgements



This work is produced under the activities in the University of Porto (FEUP) of the LIQUEFACT project (Assessment and mitigation of liquefaction potential across Europe: a holistic approach to protect structures/infrastructures for improved resilience to earthquake-induced liquefaction disasters") and has received funding from the European Union's Horizon 2020 research and innovation programme under grant agreement No GAP-700748.

I would like to thank prof. Sebastiano Foti for the great chance to let me embark on a wonderful path abroad, for his extraordinary way of teaching and for the inspiring passion in his job.

Special thanks go to my supervisor in FEUP, prof. Antonio Viana da Fonseca, for giving me the opportunity to become part of a great team of researchers, for all the support and guidance throughout this project and for the constant and meticulous attention he kept on my work.

Endless thanks go to the postdoctoral researcher Maxim Millen for the effort and the great help given me in numerical modelling day by day but, more than other, for trusting my skills and abilities.

Finally, I would like to thank Politecnico di Torino for the opportunity to work on my master thesis abroad and for the economic support.

1. Chapter: Abstract

The assessment of the liquefaction induced effects on structures represents one of the main topics of interest in earthquake geotechnical engineering research with an increasing attention in the methods to account for the large number of variabilities related to the evaluation of soil-foundation-structure interaction (SFSI) in the global response.

Currently, no robust simplified analytical procedures for the estimation of seismic liquefaction effects on structures are available and numerical modelling represents one of the best ways to capture the non-linear SFSI in the evaluation of Earthquake Induced Liquefaction Damages (EILD) on structures, usually neglected in seismic design of ordinary buildings.

However, Finite Element analyses dealing with globally complex scenarios that involve the soil deposit heterogeneity, seismic excitations, structural inertial forces, pore pressure build up, etc. would require a considerable computational burden therefore, one of the main points of interest in this field of research is the use of simplified numerical models that reduce the complexity without avoiding to consider the aforementioned aspects.

The current work is focused on the use of numerical simulations, run in the FE code PLAXIS®, for the quantification of the liquefaction induced effects on shallow foundations with a particular attention on the moment-rotation response and the evaluation of the peak foundation rotations. Pseudo-static push over analyses have been performed assuming to substitute the seismic actions with static forces and making simplifying assumptions to model the liquefied soil layers.

Since most of the liquefaction induced effects on structures are attributable to mechanism of ground failure and soil shear strength degradation, a preliminary study of the ultimate bearing capacity of shallow foundations has been carried out, even because it represents a key aspect in the quantification of the ultimate moment capacity.

The results from non-linear static push over analyses in terms of moment-rotation curves and rotational stiffness degradation curves, are then proposed to describe the soil-foundation behaviour, as a key aspect in the quantification of the structure-foundation response accounting for non-linear SFSI effects, through displacements-based procedures still to be validated for the case of liquefiable soils.

Finally, a comparison between the static push over results and the dynamic analysis results has been performed to demonstrate the applicability of the moment-rotation curves

Moment-Rotation behaviour of shallow foundations on liquefiable soils

for the simplified assessment of structural response of a shallow founded structure on a liquefiable soil deposit.

2. Chapter: Literature review

Since the Niigata earthquake (1964) in Japan and the Alaskan earthquake (1964) in USA, the mechanism of soil liquefaction and its consequent effects on structures have become one of the most significant subjects of study in earthquake geotechnical engineering research.

More recently, the series of earthquake induced liquefaction damages (EILD) that had serious impact in the populations (e.g. 2012 Emilia-Romagna, northern Italy; 2011 Tohoku Oki, Japan; and particularly 2011 Canterbury-Christchurch), have intensified the research, mainly in the view of quantifying the uncertainties related to the soil behaviour and the need to consider the soil-foundation-structure interaction (SFSI) to better describe the global response of buildings and other infrastructures.



Figure 2.1- (a) Liquefaction induced rigid tilting after 1964 Niigata earthquake; (b) Liquefaction in a residential area of Christchurch, from Diaz, 2016; (c) 5-storey building tilting after Adapazari earthquake, Turkey, from Bray et al., 2001.

Currently, numerical simulations are a good help to deal with most of these aspects and the assessment of the liquefaction associated mechanisms and their effects on structures. However, the simulations taking the complete model of each and cases are extremely difficult and computationally demanding.

Before the review of the main existing procedures available to capture and simulate the liquefaction-induced structural effects and the soil-foundation-structures interacting mechanisms, it is important to understand the phenomena of liquefaction, how it develops and its effects.

Thanks to field evidence and investigations carried out in the last decades, several kinds of seismic liquefaction-induced effects on structures can be distinguished, such as superstructure deformations or rigid body movements of shallow founded structures, like settlements and tilting without any damage on superstructure; most of these effects are attributable to a mechanism of ground failure and soil shear strength degradation.

2.1 Phenomena

Soil liquefaction could be described as a sudden, considerable loss of shear strength and stiffness of saturated, loose, cohesionless granular soils due to the excess pore pressure build-up. It can be observed under both monotonic or cyclic loading as long as the drainage is impeded, partially or totally.

A more accurate definition is given by Sladen et al. (1985):

“Liquefaction is a phenomenon wherein a mass of soil loses a large percentage of its shear resistance, when subjected to monotonic, cyclic or shock loading, and flows in a manner resembling a liquid until the shear stresses acting on the mass are as low as the reduced resistance”.

Two different phenomena occur due to the pore water pressure increase, the flow liquefaction and the cyclic mobility; in the first case a static loading causes the pore pressure increase, while the second phenomenon occurs due to cyclic loads but a small percentage of shear stiffness is recovered during unloading/reloading due to the soil dilation and contraction.

Considering a horizontal ground surface in free-field conditions, an element of soil is only subjected to the confining pressure and eventually to driving stresses, τ_D ; during the seismic shaking the additional cyclic shear stresses change the initial stress conditions, and induce the loose to medium soils contraction, which is impeded by the lack of pore

water drainage. This is due to the rapid seismic load (high frequencies) that does not allow the volumetric deformation and the consequent consolidation, or at least partially. At each cycle, the pore water compresses with a consequent increase in pore pressure and decreasing of confining effective stress, p' , lowering progressively the shear strength; simultaneously, both, bulk and shear stiffness decreases, resulting in significant volumetric post-consolidation (or ejecta) compression and shear deformations which can be very high when limited area systems transmit loads to the near surface ground. Therefore, cyclic loads characterised by a sufficiently high amplitude and a consistent number of cycles promote the liquefaction the progressive development of residual strength and large compressibility and deformability in loose, saturated, cohesionless soils. Ultimately that residual shear strength in undrained conditions can reach zero.

A common parameter used to define the liquefaction triggering is the pore pressure ratio, ru , described as the ratio of the excess pore pressure to the initial vertical effective stress, which should be close to 1 in proximity of liquefaction (Ishihara, 1993).

In free field conditions, after shaking, the reversible shear deformations essentially stop, but the volumetric deformations and the soil reconsolidation due to local pore pressure redistribution continue, which results in vertical settlements of the ground surface.

In the presence of surface loads, like shallow foundations' buildings, this process leads to large settlements during the earthquake, even before full liquefaction, well before the post dissipation of the excess pore pressure process, that is before consolidation. The settlements during earthquake are due to the loss of bearing capacity or soil softening due to a decrease of the mean effective stresses in large zones of the ground beneath the foundations, subjected already to moderate to high deviatoric stress levels in static service conditions.

As suggested by Robertson (2010), the evaluation of susceptibility to strength loss and the resulting liquefied shear strength are the first most important aspects of assessing the performance of structures on liquefiable soil deposits, even though the behaviour of liquefied soils is different in free-field conditions or in presence of buildings.

According to Kramer (1996), there are several criteria to judge if a soil is susceptible to liquefaction during an earthquake:

I) *Historical Criteria*: most of the information about soil behaviour in liquefaction conditions comes from post-earthquake field investigations, which have highlighted that the phenomenon is typical of particular materials in specific conditions, like the site distance to the seismic source or the distance to the "seismic firm" (bed-rock), that is the

transition between the very high shear waves velocities (V_s), typical of hard-soils/soft-rocks, to lower ones, typical of sedimentary recent soils;

II) *Geologic Criteria*: the knowledge about the local geology is a useful mean for the identification of liquefiable soils and it involves the origin, fabric and structure of soils, which may explain a cohesive intercept in a Mohr-Coulomb type strength criterion, and even the permeability of material, which may affect the pore pressure dissipation and effective stress reduction;

III) *Compositional Criteria*: compositional characteristics of the above referred sedimentary recent soils, such as particle size, shape and gradation, which will influence the tendency to volume contraction, to which liquefaction susceptibility is directly related;

IV) *State Criteria*: the tendency to generate excess pore pressure is influenced by the initial state of the soil; this is due in granular materials to the relative density and the initial stress level, which can be integrated in a unique index, the state parameter (Been and Jefferies, 1985); this is mostly due to the fact that the key mechanism to explain how soil behaviour conditions the performance of buildings is its tendency to contract or dilate, thus increasing or decreasing the excess pore water pressure.

In this regard, the response of a soil under both monotonic or cyclic shear is different if it is behaviourally contractive or dilative. A loose soil tends to compact if sheared and in absence of water drainage the pore water pressure increases; if the applied load is monotonic and rapid the soil may reach a peak value of the shear strength, while the pore pressure increases, and after this becomes unstable moving towards residual values, exhibiting softening behaviour at high levels of strain (Lade, 1999; Viana da Fonseca and Soares, 2014). If the residual shear strength is lower than the pre-loading shear stress (zero if the driving shear is null), liquefaction occurs. By applying a cyclic shear to the same soil, without water drainage, the excess pore pressure accumulates at each cycle and the confining pressure moves from the initial value towards a lower value till the failure. The liquefaction occurs typically for saturated soils with contractive behaviour subjected to a shear of rather high magnitude or to a rather high number of load cycles (it is fundamentally an energy dependent process).

For dilative soils the monotonic shear load can even produce an excess pore pressure at small strains (until the elastic threshold), but then it is followed by a decrease of pore pressures that can become negative at large strains with a resulting increase of the effective stress and shear strength.

If the soil is subjected to cyclic loading, there is an accumulation of excess pore pressures at the very first cycles, with a resulting contractive behaviour. Then at a higher number of cycles the pore pressures can reach negative values with a resulting increase in effective stress and consequently in the shear strength. However, liquefaction triggering during cyclic loads is a more complex phenomenon controlled not just by the density but also by the stiffness and cyclic energy dissipation. Essentially, the soil stress and density state as well as the fabric control the number of cycles required to reach the liquefaction (Ishihara, 1993).

In order to estimate the susceptibility of a soil to liquefy, it is important to account that the state of the soil is represented by a combination of physical parameters with the effective stress (state in general terms), and the cyclic stress ratio (as a normalized value of the cyclic action).

The steady-state of deformation, according to Castro and Poulos (1977), is when, at large deformations, the soil reaches a constant volume at a constant shear stress and constant effective stress, which was associated to the concept of residual conditions. This may not be the same as the critical state identity, which can be associate to an ultimate frictional resistance, or a steady-state condition in undrained conditions. Both these locus, critical or steady-state (CSL or SSL), are useful to understand in which conditions a soil can be susceptible to liquefaction or not, under monotonic loading: if the state is under the SSL the soil is not susceptible, if the state is above the SSL it is susceptible only if its residual strength (or steady-state strength) is lower than the static shear stress. Following this criterion, a soil with a certain void ratio may be liquefiable at a high confining stress but not liquefiable at a low level of stress.

Been and Jefferies, 1985 developed the concept of state parameter, ψ , based on critical state soil mechanics and applied this concept to soil liquefaction. The state parameter is defined as the difference between the in-situ void ratio, e_0 , and the void ratio at critical state (or steady-state), e_{cs} , at the same mean effective stress. If it is positive, the soil has a contractive behaviour and it may be susceptible to liquefaction; if it is negative the soil tends to dilation and liquefaction cannot occur (Jefferies and Bean, 2006).

Even if a soil is potentially liquefiable, it does not mean that an earthquake can induce liquefaction; the estimation of the occurrence of liquefaction is a critical part of most procedures for the quantification of liquefaction related damages.

The triggering can be estimated by following simplified procedures that compute the cyclic stress demand and the cyclic shear resistance of a soil profile, or through advanced numerical modelling.

The first methods are based on Standard Penetration Test (SPT) and Cone Penetration Test (CPT) data or on soil shear wave velocities; moreover, Energy-based methods have been proposed to better account for the dependence on cumulative strain.

However, simplified procedures in many cases do not account for the vertical interaction between layers which is very important for the estimation of the pore pressure build up and consequently the eventual liquefaction triggering under buildings where the additional shear and confining stresses from the foundation can dramatically change the pore pressure build up.

Numerical modelling could represent the best way to capture the different mechanisms involved and analyse the effects of liquefaction on structures (Viana da Fonseca et al., 2017). Moreover, they can imply on the potential triggering because they can capture the complexity associated with a phenomenon that is basically interdependent. So, Soil-Foundation-Structure-Interaction (SFSI) for the purpose of evaluating Earthquake Induced Liquefaction Damage (EILD) will depend on the use of advanced constitutive models in numerical codes, such as FLAC® or PLAXIS®, that can run a significant number of cases that can identify how many factors can condition the vulnerability of structures.

All the constitutive models should be characterised by the simplicity in finding the parameters from in situ and laboratory tests and they should be as realistic as possible.

The estimation of liquefaction triggering is particularly worth to the evaluation of the resulting liquefaction effects, often related to a ground failure. The effects in free-field conditions could be quantified through the estimation of ground settlement and lateral spreading. The presence of superstructures overlying liquefiable soil deposits unavoidably changes the soil behaviour and its stress state in comparison with the free field condition.

2.2 Effects of liquefaction

Most of the effects of liquefaction phenomena are related to the soil shear strength degradation and the consequent soil instabilities that occur when the shear strength of the liquefied soil is below the value of the shear stress needed for an equilibrium. When the

soil reaches this condition, it keeps deforming until reaching a stable configuration when the equilibrium of stresses is restored. The amount of deformation required is dependent on the difference between the shear stresses required for the equilibrium and the soil shear strength.

Liquefaction instabilities generate some of the most problematic earthquake induced damages observed on buildings and other infrastructures like buried pipelines, embankments, abutments, etc.

In particular, liquefaction can produce rigid-body movements, including vertical settlements, total or differential, of foundations, and tilting, producing different types of damages on the superstructure and a loss of serviceability.

The assessment of earthquake-induced liquefaction damage to buildings requires:

I) An appropriate simulation of the soil behaviour and of the Soil-Foundation-Structure Interaction (SFSI) in order to account for the modification of the global dynamic response and permanent deformations on the building.

II) A definition of damage levels accounting for not only the damage experienced by the structural members but also for the loss of functionality related to rigid-body movements: global settlements and tilting.

Settlements

Liquefaction-induced settlements under shallow founded buildings represent a completely different phenomenon from the ground vertical settlements in the free-field even though in engineering practise the estimation of settlement is still based on empirical approaches originally conceived for the free-field vertical settlements, which are associated only to a volumetric deformation.

The different behaviour observed with the presence of buildings can be caught through field observation, laboratory modelling and, recently, by numerical modelling using fully coupled effective stress analysis.

First of all, settlements under buildings have been observed to be larger than in the free field.

During seismic loading the soil deforms and imposes deformations to the foundation; the foundation and the structure can move out of phase with the bedrock causing transverse forces to be applied to the soil; moreover, the incident seismic waves are reflected and scattered by the foundation which is consequently loaded developing curvatures and bending moments. The motion induced at the foundation level generates oscillations in the superstructure that develop inertial forces and overturning moments at its base

(Pecker, 2007). If the earthquake is sufficiently long-lasting, at the last phase of the shaking the static pressure prevails, leading to a possible failure mechanism with a consequent large volumetric deformation. At the end of the shaking the settlement is totally controlled by the volumetric deformations due to the soil reconsolidation.

The increased settlement is partially due to the weight of the structure that increases the compression of the soil; however, the majority of the settlement of buildings in liquefied soil is related deviatoric stresses from the building vertical load compared to reconsolidation and sedimentation (Dashti et al., 2010, Karamitros et al., 2013). The most important parameters affecting the deviatoric settlement are related to the characteristics of soil, geometry of the foundations, corresponding loading associated to the buildings characteristics and ground motion, as observed in Bray and Dashti (2010) when considering the case-study from Adapazari earthquake in Turkey.

The estimation of settlement after-shaking can be carried out with the same approaches used for the estimation of vertical settlements in free-field, as suggested by Bray and Macedo, 2017, but the fraction of settlement during shaking requires rather complex modelling strategies able to capture the SFSI effects.

Some empirical correlations have been formulated, based on the results of laboratory testing such as shaking table tests (Yoshimi and Tokimatsu, 1977) and later centrifuge tests that tend to better model the stress state of the soil. In recent years numerical analyses, mainly using fully-coupled modelling of the soil and rigid foundations with or without elastic superstructures have been carried out.

Shakir and Pak (2010) proposed a formulation for the case where there was no bearing capacity failure; the numerical model was previously calibrated by centrifuge tests conducted by other authors (Hausler, 2002). The building is modelled as a rigid block with width B and the analyses are carried out for different width ratios (L/B), observing an increase in the settlement ratio when the width ratio is lower than 0,9 and a decrease for higher values. This can be explained by the intersection of a pressure bulb (with a depth of influence equal to the width of the foundation) with Z_L , the depth of the liquefiable layer.

The settlement is found to be proportional to the pressure (by $q_f^{0,4}$) and it is not influenced by the action (PGA) and the relative density (D_r), because of the term $Z_{L,m}^{0,5}$.

Karamitros et al. (2013) proposed an analytical formulation for the dynamic settlement where it is proportional to the peak bedrock acceleration, a_{max} , the representative period

of the motion, T_s , the number of cycles and the degraded factor of safety of the foundation, FS_{deg} which depends on the excess pore water pressure ratio, r_u . They used a numerical model in which the soil is composed by two layers, the lower liquefied layer and the clayey crust that gives a beneficial contribution to the stability and represents an upper bound beyond where failure occurs entirely within the crust and does not get affected by the liquefiable layer. However, this method is difficult to apply in sites where there is no clay crust; Dimitriadi et al. (2017) refined the above approach by using a numerical model in which the crust is characterised by a cohesionless, permeable material, showing that, thanks to the permeability, an upper zone of the liquefied layer behaves as a transition zone in which there is a lower decrease of strength.

Bray and Macedo (2017) proposed a simplified procedure based on experimental tests and analytical work. A parametric set of numerical simulations have been carried out in order to show the influence of different parameters on the deviatoric settlement. Through the numerical simulations it is possible to assert the big influence of the degradation of the bearing capacity to the settlement increase and the authors suggest that for very low values of the factor of safety, the estimation of settlement is worthless. A fitting regression of all the results of the parametric analyses gives an empirical correlation for the settlement as a function of two intensity measures, CAV_{dp} is the standardised Cumulate Absolute Velocity and LBS is an index of equivalent liquefaction-induced shear strain on the free-field. Moreover, a complete procedure for the estimation of the total settlement is proposed.

Other authors (Andrianopoulos et al., 2010, Dashti and Bray, 2013, Ziotopoulou and Montgomery, 2017 among others) have conducted numerical simulations for the assessment of the liquefaction-induced settlement.

Tilting

Dynamic inertial forces in the structure or deformations in the soil can drive foundation tilt.

The phenomenon of foundation tilting may produce flexural and shear-induced damage to buildings, this being aggravated when differential settlements are involved. However, rigid-body tilt can occur without structural damage or superstructure deformations. This usually happens when the foundation and structure are relatively rigid compared to the soil stiffness.

The interaction between rigid body tilt, local foundation rotations and differential settlement is difficult to separate. The difficulty in interpreting and estimating the differential deformations is partially due to poorly defined reference points.

In this work the foundation rotation is expressed as the difference in vertical displacement of the two edges of the foundation divided by the foundation width, as clarified in the following Chapter 4.

Two types of foundation rotation can be distinguished during an earthquake: (i) the peak foundation rotation, which is the maximum rotation occurring, that is partially restored through the soil rebounding and through gravity inertia after the uplift initiation; and, (ii) the residual or permanent foundation that remains even after the earthquake ends.

Different causes lead to foundation tilting or differential settlements, such as horizontal heterogeneity of the underlying soil profile that produces distinct soil deformations under each and all the footings. This variation can also be caused by pore water flow during and after shaking that depends on the layout of the footings.

The overturning moments applied by the superstructure on the foundation can result in soil yielding by extra pressure in part of the foundation, while other parts may uplift. The contribution of foundation uplift compared to soil yielding can increase the mobilization of residual deformation. Therefore, it can be expected an aggravation of the nonlinear “elastic” deformation with foundation uplift (Chatzigogos et al., 2011) while soil yielding typically results in permanent soil deformation. The level of foundation uplift is largely controlled by the axial load on the foundation, and therefore the foundation residual tilt can be linked to the level of peak foundation rotation and the applied axial load (Deng and Kutter, 2012; Deng et al., 2014). Lateral spreading or asymmetric horizontal earth pressure results in non-uniform soil deformations and foundation tilt. The imbalance of earth pressure due to either a free-face of sloping ground results in static shear stress in the soil and favoured movement in the less supported direction. An extreme case of this is when cracks open from laterally spreading soil and part of the foundation completely loses support.

Currently, no robust simplified analytical methods for the estimation of foundation tilting exist, due to the large number of variables that contribute to the phenomenon. However, there are some empirical correlations based on the total settlement or factor of safety against overturning moment (Kiyota et al., 2014; Karimi and Dashti, 2016; Tokimatsu et al., 2017). For non-liquefied soils there are expressions that account for SFSI induced permanent tilt (e.g. Deng et al., 2012, Millen et al., 2016). For specific structures the

foundation tilt can be estimated through numerical simulation where soil heterogeneity, pore pressures, superstructure inertial forces, lateral spreading can all be modelled directly, however, parametric studies are required due to the sensitivity of the tilting behaviour to soil, foundation and structural characteristics as well as the expected ground shaking.

Another approach to estimate residual foundation tilt is to use centrifuge testing, although these studies have been very limited due to the excessive costs.

2.3 Soil-Foundation-Structure Interaction (SFSI)

The dynamic response of the structure is influenced by the soil deformations during seismic loading which are imposed to the foundation. The compliance of the supporting soil modifies the behaviour of the structure and the interplay between the soil, foundation and superstructure is called Soil-Foundation-Structure Interaction (SFSI) in literature.

The accurate estimation of the effects of SFSI is one of the biggest challenges for geotechnical and structural engineering, because of the large number of variables involved such as the geometry of the foundation, the soil and structural behaviour, and ground motion characteristics.

Due to these difficulties, SFSI is usually neglected for the seismic design of ordinary buildings even though there are conditions in which it is important to consider.

Often some approaches that simplify the problem are followed such as procedure that turn the non-linearity of the problem into an equivalent linear behaviour. For non-liquefiable soils nowadays, there is a growing support in approaches that account for nonlinear soil-foundation deformations in order to limit the shaking energy from entering the structure (Pecker and Pender, 2000, Deng et al., 2014). This is because the behaviour of the system can be predicted in terms of nonlinear stiffness, foundation moment capacity, settlements and residual tilting (Deng and Kutter, 2012)

Two separate phenomena are conventionally associated to the change in building response:

- The kinematic interaction: during the earthquake the soil layers are subjected to an excitation consisting of incident waves (P and S waves); the ground motions registered at the bedrock level are modified up to the surface through the soil layers due to the geometric and stiffness features. The seismically deforming soil transmits

the deformations to the foundation and consequently to the supported structure. Therefore, the foundation is stressed developing curvatures and bending moments. The waves also reflect of the foundation due to a contrast in stiffness between the soil and the foundation, and these waves interact with the upward propagating waves. The effects are more complex when some of these layers have liquefiable soils, both because the ground motion time series are highly conditioned by wave reflections in between the contrasting layers and the frequency contents are significantly changed, and this can have consequences in EILD, especially in deep foundations.

- The inertial interaction: the motion induced at the foundation level generates oscillations in the superstructure that induce additional dynamic displacements and overturning moments at its base. These effects produce additional dynamic forces to the foundation.

The foundation should be checked for the combined kinematic and inertial forces even if in shallow foundations many researchers have demonstrated that kinematic interaction usually de-amplifies horizontally propagating shear waves. Anyway, the complexity of the problem to solve requires numerical calculations because there are no closed form solutions capable to fully describe the phenomena. In full finite element mesh modelling the kinematic and inertial interaction are implicitly accounted for by directly modelling the soil and structural domain. If the soil domain and structural domain are decoupled into separate analyses the inertial interaction is typically modelled in the structural analysis through springs and dashpot elements to represent the soil-foundation interface dynamic stiffness and radiation damping respectively.

Other SFSI mechanisms can also influence the structural response:

- The foundation rocking potentially reduces the shaking energy entering the structure: it is based on the formation of a non-linear mechanism at the base of the structure that limits the first mode of response, which is dominant especially in rigid buildings, with raft foundations. In seismic design, the loads are often reduced thanks to the structure ductility but, if foundation rocking is the dominant deformation mode, the system may not dissipate as much energy as a yielding structure or foundation deformation the causes greater soil yielding. However, energy dissipation by non-linear soil-structure interaction effects may be unavoidable, especially during strong earthquakes, but there is a lack of approaches to account these effects (Gazetas et al., 2013).

- The liquefaction phenomena change the stiffness and strength of the supporting soil, with a consequent increase in a level of energy dissipation and deformation at the soil-foundation interface. Moreover, the reduction in stiffness in liquefied layers tends to highlight the stiffness contrast between the different materials composing the soil and making the conventional soil-foundation impedances less applicable. The possible presence of a natural or artificial stiff crust between the foundation and the liquefied soil represents a seismic isolation system (Bouckovalas, 2017, Karitzia, 2017).

2.4 SFSI modelling approaches

There are several approaches to model the soil-foundation-structure interaction:

- Direct approach: requires the use of a unique numerical simulation in which soil, foundation and structure are modelled together. The main advantage is that the kinematic and the inertial interaction together with the site effects, the material heterogeneities and eventually the liquefaction induced effects are naturally taken into account. However, there are some issues related to the choice of this approach which are in the SFS modelling itself; as suggested by ITASCA (2017) the computational time-step should be proportional to the size of the material elements and inversely proportional to the stiffness of the material; typically a structure is characterised by small stiff elements while soil is relatively weak and infinite in size thus, separate numerical models accounting for different aspects are often used to efficiently solve these problems. Moreover, the quantification of damping for simulating energy dissipation due to mechanisms not directly considered in the model represents a further difficulty together with the modelling of interfaces between soil and foundation with a single constitutive model.
- De-coupled (substructure) approach: there are two different simulations, i) soil and massless foundation are modelled in one simulation, ii) the foundation and structure are modelled together with simplified considerations of the soil behaviour but accounting the inertial effects. In particular, there are two ways of modelling the soil behaviour, following the Winkler theory or the macroelement model, later detailed in Section 4. However, currently there are no suitable macroelement or Winkler models that can simplify the effects of liquefaction on SFSI.

- Simplified analytical approach: there are mathematical formulations that capture the whole soil-foundation-structure behaviour (Paolucci, 2013, Millen, 2016). Displacement-based procedures convert the non-linear behaviour in non-liquefiable soils, providing a rapid approach to assessing SFSI effects and could be extended to liquefaction problems.

3. Chapter: PLAXIS 2D Model validation for Ultimate Bearing Capacity of Shallow Foundations

3.1 Introduction

The main objective of this chapter is to validate the numerical models in PLAXIS 2D by solving a common geotechnical problem of the ultimate bearing capacity of a rough strip footing over both homogeneous and layered soil. One of the main issues in numerical analyses is following the right procedures for the construction of the model, which should be as accurate as possible to best represent the reality. The ultimate bearing capacity of shallow foundations is a useful benchmark for verifying the correct implementation of the model. First, because there are many widely accepted closed form solutions for comparison [Vesic, 1973, Meyerhoff, 1951], and secondly the bearing capacity is a key aspect of the ultimate foundation moment capacity [ref. Deng et al., 2012, Chatzigogos, 2011].

This chapter provides a description of the steps followed to create the geometry of the domain, generate the FE mesh, execute the calculations and interpret and compare the results with analytical solutions, for two different cases of homogeneous sandy soil and homogeneous clayey soil. Following this, a parametric study was carried out to understand the behaviour of the heterogeneous deposit for different footing sizes and soil properties.

The heterogeneous deposit consisted of two layers of different materials: the upper layer, whose thickness was varied, was characterised by a stiff sandy soil, having the same properties of the material used for the model validation and representing a “crust” between the shallow foundation and the lower weaker layer.

The lower layer was modelled with strength and stiffness parameters typical of a liquefied or partially-liquefied soil. In this condition a temporary bearing capacity degradation and an increase in settlements could be expected for the shallow foundation. For these reasons a degraded internal friction angle was calculated for the lower layer, following the analytical relationships in Cascone and Bouckovalas (1998), while the shear modulus was

decreased proportionally to a reduction of the shear wave velocity according to Karatzia et al. (2017).

At the end of the chapter a comparison between the results from the homogeneous soil model and the results from the layered deposit model is presented in order to demonstrate the decay in ultimate bearing capacity and the increase in settlements of shallow foundations laying on liquefied soils and how the crust thickness influences the behaviour.

3.2 Literature review

Bearing Capacity of shallow foundations on homogeneous soil

In 1948 Terzaghi proposed a theory to determine the ultimate bearing capacity of a shallow, rough, rigid, continuous (strip) foundation supported by a homogeneous soil layer, supposing a general and rigid body shear failure.

The ultimate load per unit area of the foundation, for a soil with cohesion, friction and weight is given by the Equation 3.1:

$$q_u = cN_c + qN_q + \frac{1}{2}\gamma BN_\gamma \quad (3.1)$$

where B is the width of the foundation and N_γ , N_c , N_q bearing capacity factors, defined as:

$$N_q = \frac{e^{2\left(\frac{3\pi}{4} - \frac{\varphi}{2}\right)\tan\varphi}}{2\cos^2\left(45 + \frac{\varphi}{2}\right)} \quad (3.2)$$

$$N_c = \cot\varphi(N_q - 1) \quad (3.3)$$

$$N_\gamma = \frac{1}{2}K_p\gamma\tan^2\varphi - \frac{\tan\varphi}{2} \quad (3.4)$$

Several theories are then proposed for the estimation of the bearing capacity factors and one of the more widely adopted is Meyerhof approach according to which the bearing capacity factors depend on the degree of mobilization of shear strength on the equivalent free surface. For surface foundation conditions they are defined as follows:

$$N_q = e^{\pi\tan\varphi\frac{1+\sin\varphi}{1-\sin\varphi}} \quad (3.5)$$

$$N_c = (N_q - 1)\cot\varphi \quad (3.6)$$

$$N_\gamma = (N_q - 1)\text{tg}(1,4\varphi) \quad (3.7)$$

Where N_c and N_q are taken by Prandtl's solution. Several are the theories about the estimation of N_γ and here the one by Hansen is proposed:

$$N_\gamma = 1,5N_c\text{tg}^2\varphi \quad (3.8)$$

Another important approximation of N_γ is given by Vesic, even though there is an exceeding error of about 5% compared to the exact solution.

Bearing Capacity of shallow foundations on layered deposit

A theory for estimating the ultimate bearing capacity of a shallow continuous foundation supported by a strong soil layer underlain by a weaker soil layer has been developed by Meyerhof and Hanna, 1978. This theory is valid when the ratio H/B is relatively small (where H is the thickness of the upper layer and B is the width of the footing) so that the top layer is involved in a punching shear failure while the bottom one, the weaker, is involved in a general shear failure.

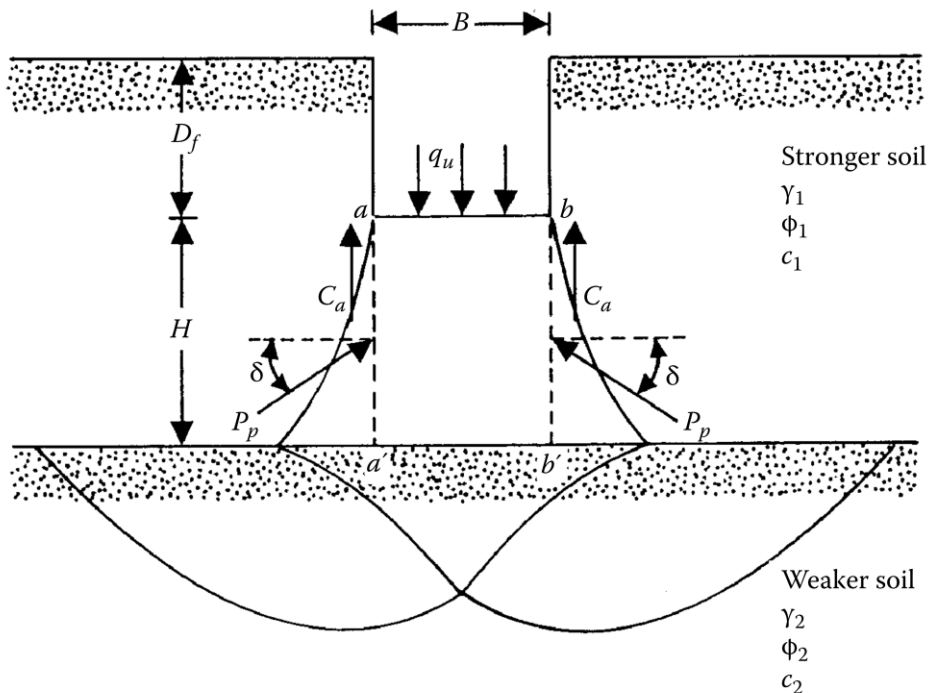


Figure 3.1- Continuous foundation on layered soil: stronger over weaker.

The general solution for the ultimate bearing capacity is given by the equation:

$$q_u = q_b + \frac{2c_a H}{B} + \gamma_1 H^2 \left(1 + \frac{2D_f}{H} \right) \frac{K_s \tan \phi_1}{B} - \gamma_1 H \leq q_t \quad (3.9)$$

Where,

c_a is the unit adhesion;

γ_1 is the unit weight of the upper layer;

D_f is the depth of the foundation;

H is the difference between the upper layer thickness and D_f ;

K_s is the punching shear coefficient that can be determined from the plot in Figure 3.2 below, in function of the variation of the upper layer friction angle, ϕ_1 , and of the q_2/q_1 .

The quantities q_1 and q_2 are, respectively, computed as follows:

$$q_1 = c_1 N_{c(1)} + \frac{1}{2} \gamma_1 B N_{\gamma(1)} \quad (3.10)$$

$$q_2 = c_2 N_{c(2)} + \frac{1}{2} \gamma_2 B N_{\gamma(2)} \quad (3.11)$$

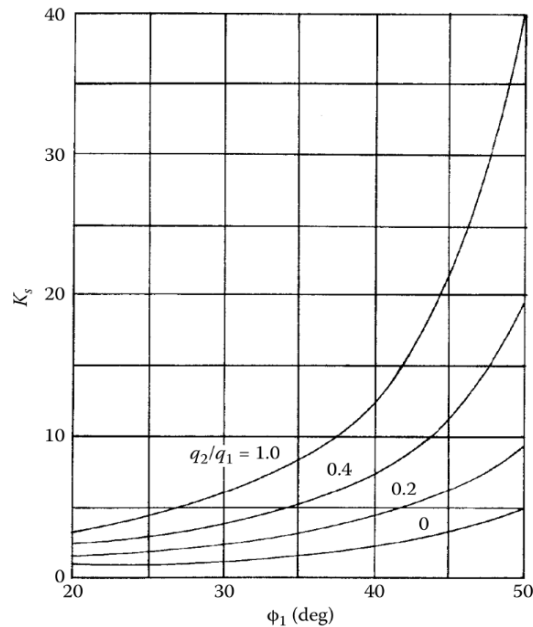


Figure 3.2- Variation of K_s with ϕ_1 and q_2/q_1 .

The terms q_b and q_t represent the bearing capacity of the bottom and top layer and they are computed with the following expressions:

$$q_b = c_2 N_{c(2)} + \gamma_1 (D_f + H) N_{q(2)} + \frac{1}{2} \gamma_2 B N_{\gamma(2)} \quad (3.12)$$

$$q_t = c_1 N_{c(1)} + \gamma_1 D_f N_{q(1)} + \frac{1}{2} \gamma_1 B N_{\gamma(1)} \quad (3.13)$$

In case of sands, the expression for the ultimate bearing capacity turns to the expression below:

$$q_u = q_b + \left(1 + \frac{B}{L}\right) \gamma_1 H^2 \left(1 + \frac{2D_f}{H}\right) \frac{K_s \tan \phi_1}{B} - \gamma_1 H \leq q_t \quad (3.14)$$

3.3 Model validation

The numerical analyses were performed using the FE code PLAXIS 2D, and the model was validated considering the case of a strip footing placed on a homogeneous deposit.

Model inputs

The first step relates to the choice of the context to simulate, the soil features, the water table conditions, the geometry and the material properties of the footing.

The footing was modelled as a rigid, massless plate with a rough interface in order not to be allowed sliding. In Table 1 below the footing features are summarised.

Parameter	Symbol	Value
Material type		elastic isotropic
Width of the foundation	B [m]	1
Depth of the foundation	D [m]	0
Unit weight	γ [kN/m ³]	0
Axial rigidity	EA [kN/m]	5E+06
Flexural rigidity	EI [kN/m/m]	1E+06
Weight	W [kN]	0
Poisson's ratio	ν	0,3

Table 1 – Footing features.

Two types of soils were considered for the validation procedure. The first type was a sandy soil whose parameters were taken from a well-known granular soil in literature, the loosely packed Houston sand; the second one was a stiff clay. Both were modelled by using the Hardening Soil constitutive model but the sand was considered in drained conditions, while the clay was modelled as an undrained system.

The base layer was supposed to be a very stiff rock that represented a natural boundary but it was not included in the model because it could be replaced by an appropriate ‘rigid-base’ boundary condition. The water table was assumed to be below the base of the model and therefore was neglected. The input data about the soils parameters are shown in Table 2 below.

Parameters	Sand	Clay
Soil Model	Hardening	Hardening
Drainage type	Drained	Undrained (B)
γ_u [kN/m ³] dry unit weight	17	17,5
γ [kN/m ³] saturated unit weight	19	19,5
e_0 [-] void ratio	0,8	0,7
ϕ [°] angle of internal friction	34	-
ψ [°] angle of dilatancy	4,3	-
c [kPa] cohesion	0	-
S_u [kPa] undrained shear strength	-	85
OCR over-consolidation ratio	-	2

Table 2 – Materials properties.

Model construction

The numerical project started by creating the geometry of the model and by setting the project properties. For these analyses the properties are the default ones and a plane strain deformation was chosen. The full domain was considered rather than using an axisymmetric boundary, because the following analyses that involve foundation rotation would require the full domain to be modelled.

One of the most important goals of the validation is the definition of the domain size. In this regard, the external boundaries should be far enough to avoid any interference in the stress-strain involved volume and to ensure the geostatic conditions in points sufficiently distanced. Therefore, after a set of simulations about the model width changing, a length of 15 times the base of the footing was adopted for each side of the domain. The thickness of the soil layer varies from a minimum value of 6 metres to the maximum value of 14 meters in order to find the most suitable one. The lower boundary was fully fixed in order to simulate the stiff rock below; the side boundaries were fixed perpendicularly while the upper boundary was not fixed to simulate the free field. The water head was defined equal to the minimum vertical coordinate in order to avoid the presence of water in the model.

Once the geometry and the boundary conditions were decided, a definition of the soil stratigraphy was needed. Information about the soil layers was entered in the *Borehole* box in PLAXIS. *Borehole* is a tool that allows the user to create different layers characterised by different thickness and different properties. In this case of homogeneous soil only one layer was defined and the top and bottom coordinates were introduced.

The “Hardening” model was selected for the sandy soil and all the properties were entered as referred in Table 2. The “Hardening Soil” model is an advanced model for simulating different types of soils, both soft and hard soils (Schanz, 1998). It follows the hyperbolic relationship between the axial strain ε_I and the deviatoric stress q in primarily an elemental triaxial loading.

The effective cohesion, c' , was taken to zero in order to reproduce a purely frictional soil; the dilatancy cut-off was not selected and the earth pressure coefficient, K_0^{NC} , was automatically computed by Jaky’s law. The tension cut-off was selected and a tensile strength equal to zero was defined. The definition of the stiffness parameters was also required. In PLAXIS Hardening model reference values were needed for the elastic stiffness which means elastic moduli in correspondence of a value of 100 kPa of the confining pressure, p_{ref} , in a triaxial test. The secant modulus at the 50% of the peak shear strength, E_{50}^{ref} was set equal to 30 MPa for the sand, the same as the oedometric modulus, according to the “default” option (Schanz and Vermeer, 1998), while the unloading/reloading stiffness modulus, E_{ur}^{ref} was set equal to 3 times the secant, as it is suggested by default in material model manual (PLAXIS, 2017).

A secant modulus at the 50% of the maximum deviatoric stress was considered instead of the initial elastic Young’s modulus, E_i , as suggested by the PLAXIS manual, due to the strong decrease of stiffness from the very small strains.

The exponential power parameter for the stress-level dependency, m , defined as the slope of trend line in $\log(\sigma_3/p_{ref})$ - $\log E_{50}$ space was set equal to 0,54 because it is usually in the range of 0,4-0,7 for sands, for the clayey soil it was set equal to 1.

The Poisson’s ratio for unloading/reloading was left with its default value equal to 0,2.

The footing is added to the model as a structural element called Plate. It was placed in the centre of the plan and it was delimited by two vertices. The footing properties were defined according to Table 1. As a massless element it does not induce a change in soil stresses and strains thus the application of a vertical load was imposed. Either a line load or a distributed load could be used since the foundation was modelled as essentially rigid,

in this simulation a distributed load was chosen and made equal to the analytical ultimate load.

To complete the definition of the soil model, an interface element under the foundation was added to model the soil-footing interaction. The interface was set as *rigid* with a corresponding unit value of the factor R_{inter} and the gap closure was not considered.

Usually the interface parameters could be modelled as the adjacent soil if it has a frictional behaviour, otherwise it's possible to create a specific material for the interface by using the same properties of the adjacent soil but changing the strength parameters. In this case the interface properties were set equal to the adjacent soil just because it had frictional behaviour.

The Finite Element mesh was created with a medium detail in terms of size of the elements but taking care to first intensify the density mesh in correspondence of the structural or interface elements and in correspondence of the material interface in order to let the computation continuously follow the strains and stresses changes from an element to the adjacent one.

Moreover, it was worth to check the symmetry of the element mesh around the foundation to avoid numerical instabilities or deformations not coherent with the loading conditions, as explained in Figure 3.3 below.

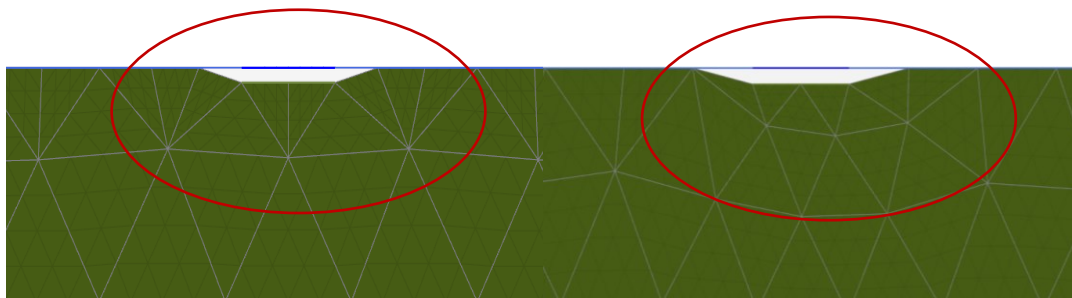


Figure 3.3 – Right and wrong geometry of the mesh at the foundation contour.

The first image represents a right mesh distribution, symmetric with respect to the vertical axis, while the second image shows a wrong mesh distribution that could affect the analysis results.

The following Figure 3.4, Figure 3.5 and Figure 3.6 show the FE models for three different sizes adopted in these tests.

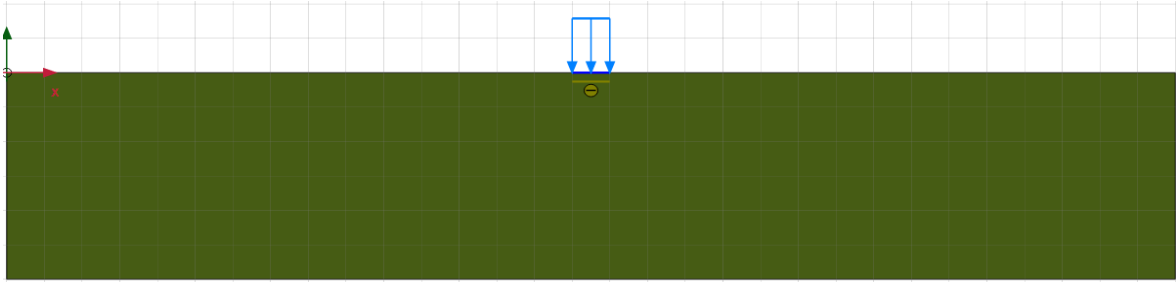


Figure 3.4- Numerical model of the soil-foundation system H=6 meters.

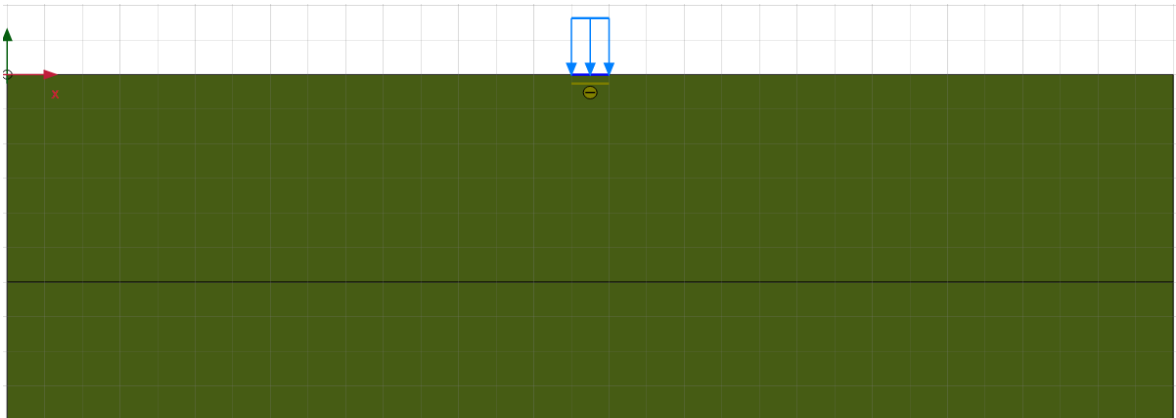


Figure 3.5- Numerical model of the soil-foundation system H=10 meters.

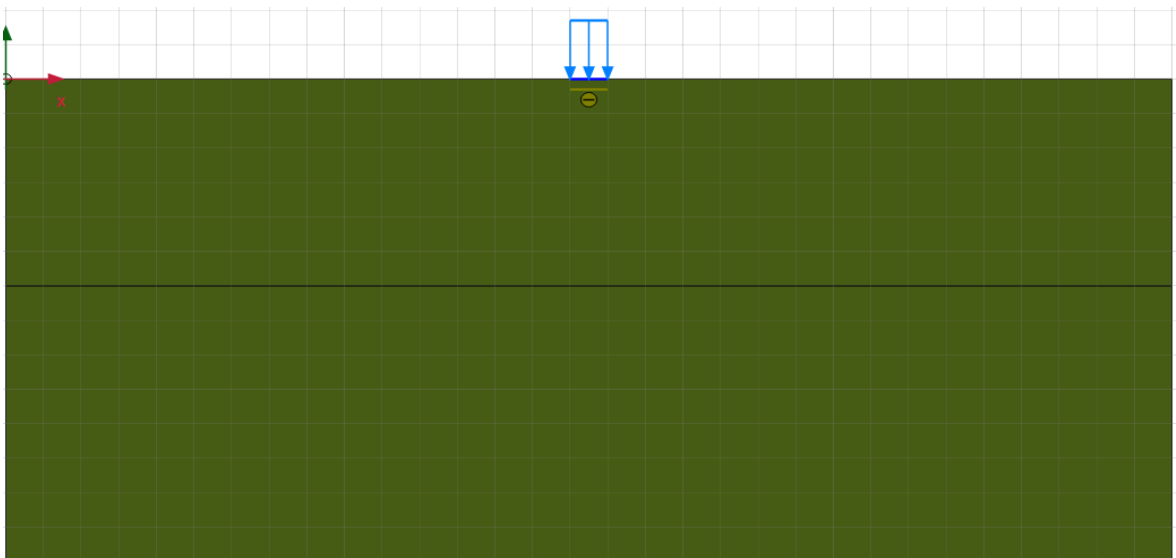


Figure 3.6- Numerical model of the soil-foundation system H=14 meters.

Running of the Model

Once the procedures for creating the model were completed, the execution of the calculation started, divided into different phases.

The final goal was the load-displacements response of the footing therefore, two different stages of computation were considered:

- Initial phase: the calculation type is “K₀ procedure” in which there was the direct generation of initial effective stresses, pore pressure and state parameters, according to PLAXIS manual. In this stage all the loads, structures and interfaces were deactivated.
- Phase 1: the calculation type was “Plastic” which means an elastoplastic drained (or undrained) analysis. This phase started at the end of the initial phase and it was used to simulate the response of the system subjected to a pure vertical load, N_{app}, so the structural elements, the interface element and the vertical line load were activated. The numerical parameters were the default ones except for the tolerated error that was decreased to a value equal to 0,01. For this stage the displacements and strains developed in the previous phase were reset to zero and the option “use line search” was activated. The applied load, in the vertical direction, was set as the analytical bearing capacity calculated from Vesic (1973) solution. If the applied load was not high enough for reaching the soil collapse, the analysis was re-run with an increased load until no additional load could be tolerated, resulting in collapse.

Homogeneous sandy soil results

The calculation process was carried out for the three mentioned geometries and the load-displacements curves are presented and compared in the Figure 3.7 below. They were built as follows:

- A central point of the footing was chosen to be queried;
- The “plastic” calculation allowed to generate increments of the prescribed load that has been applied (ΣM_{stage}) as the ratio of the incremental value over the applied one. This ratio varied from 0 to 1, 1 meaning that the total load was applied;
- The incremental values of the vertical load were computed multiplying each ΣM_{stage} by the applied load;
- The aforementioned load increments were plotted against the vertical displacements registered in each step as shown in Figure 3.7 for the three model geometries.

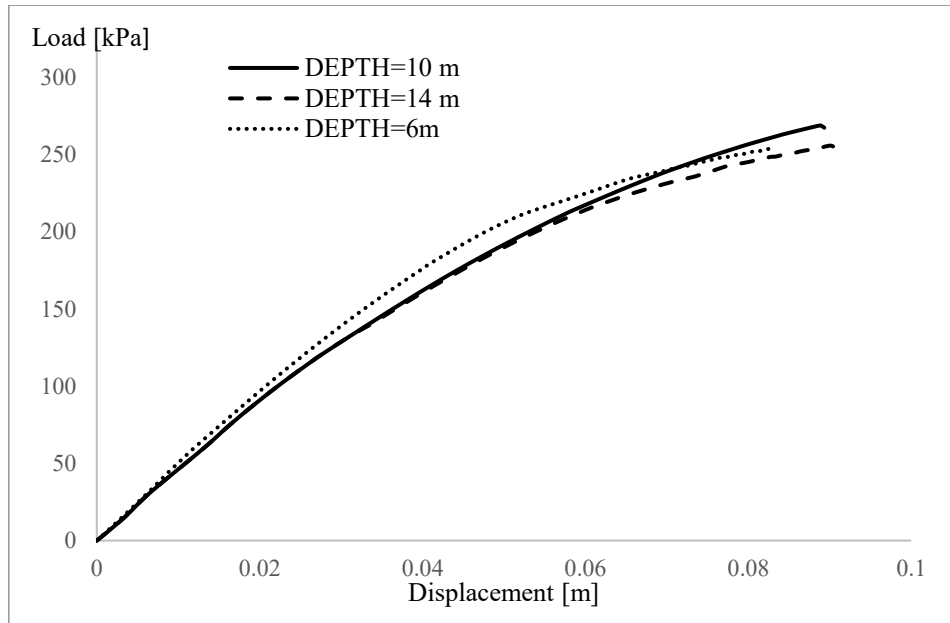


Figure 3.7- Load-displacement response for different geometries of the FE model.

The plotted curves show that the results from the model of 14 metres depth and the ones from the model of 10 metres depth are in good agreement for almost 90% of the applied load and then there is a slight discrepancy in the two trends which results in two different values of the maximum vertical load. However, the results from the calculations in the two models provided values of stresses and strains in the soil quite similar between each other. The calculations from the model of 6 metres depth gave results far from the other two models both in terms of vertical displacements and maximum vertical load, as shown in Figure 3.7, Therefore, it was a priori excluded, suggesting that the proximity of the rigid boundary condition influenced the results.

Finally, the model of 10 metres depth was chosen as the most appropriate, since it conciliated the smallest sized in which the boundaries no longer affected the results and also because there was a good agreement with the ultimate axial load value analytically computed by the theories described in the following section.

Verification of the sandy soil results

The numerical results about the ultimate vertical load were compared with Meyerhof solution; by using the theoretical relationship, the ultimate bearing capacity for a depth of 10 metres below the base of the footing is equal to 265 kPa which is in good agreement with the one obtained by PLAXIS calculation equal to 268 kPa.

Model verification for clayey soil

In order to confirm the validity of the numerical model, other cases are proposed by changing the geometry of the problem or the soil conditions.

In the first case there is only a changing of soil properties, considering a homogeneous layer of clay whose parameters are summarised in Table 2. The soil was characterised by an angle of shearing resistance equal to zero thus it was needed to add an interface element between the footing and the soil layer which did not allow null friction. For this purpose, a new material was created with the same general properties of the clay but changing the value of the cohesion to an arbitrary value of 5 kPa, in order to model the interface with a non-purely frictional behaviour and the value of the angle of shearing resistance in 34°. The secant modulus at the 50% of the peak shear strength, E_{50}^{ref} was set equal to 7,9 MPa for the clay, the same as the oedometric modulus, while the unloading/reloading stiffness modulus, E_{ur}^{ref} was set equal to 3 times the secant, as suggested by Schanz and Vermeer (1998). The Poisson's ratio was set equal to 0,495, to approximate an undrained condition of the soil.

The analytical ultimate bearing capacity for the strip footing was computed referring to Salencon and Pecker, 1995 equation:

$$q_u = (N_c + \pi)S_u B \approx 437 \text{ kPa} \quad (3.15)$$

The numerical load-displacement curve shows that the ultimate load is equal to 435 kPa in the clayey soil, in good agreement with the theoretical value.

The plot in Figure 3.8 includes a comparison with the theoretical elastic vertical stiffness, calculated from Gazetas (1991) solution, as follows:

$$K_{NN,0} = 0,73 \frac{G \cdot B}{(1 - \nu)} \quad (3.16)$$

The term G represents the elastic shear modulus that was calculated from the unloading/reloading elastic modulus, E_{ur} , with the relationship valid in the elastic field, in undrained conditions ($\nu \approx 0,5$):

$$G = \frac{E_{ur}}{3} \quad (3.17)$$

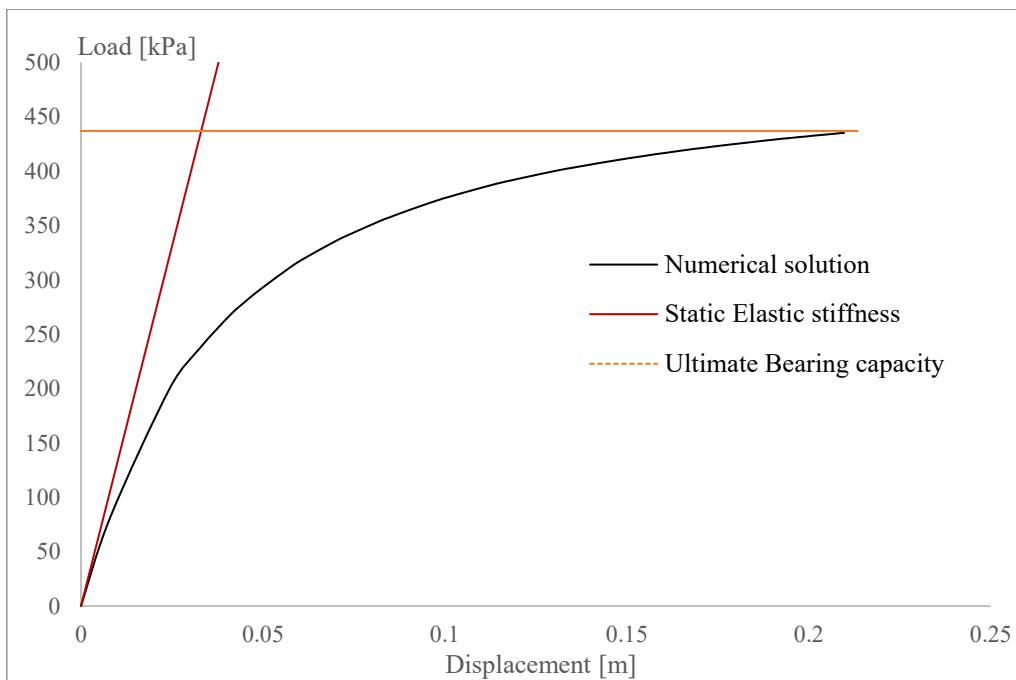


Figure 3.8- Load-displacement response in a clayey soil vs Analytical elastic stiffness.

The elastic response is overlapping the numerical solution in the very first part of the plot, showing that the soil elastic behaviour is limited to low values of the vertical load. Due to the choice of the hardening soil model in PLAXIS using a continuous plastic response (or hyperplastic) it's possible to represent the material non-linearity better than using other simplified material models such as Mohr-Coulomb.

The second case approaches the effect of a change in the width of the foundation to a value of 4 meters, leaving the same soil properties of the validation case. If the geometry of the problem changed, it was necessary to change also the size of the domain proportionally, thus the width of the FE model was increased to 60 meters wide while the depth was increased to 40 meters.

The obtained analytical ultimate load was equal to 1058 kPa while, according to the plot shown in Figure 3.9, the numerical simulation resulted in a value of about 4% higher.

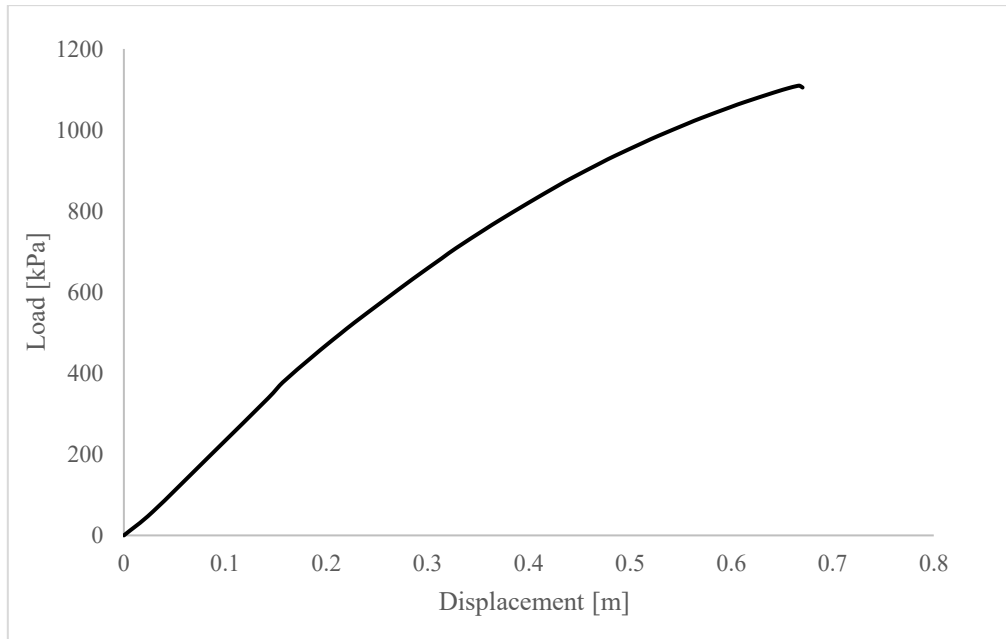


Figure 3.9- Load-displacement response in a sandy soil (Foundation width=4 m).

3.4 Bearing Capacity of shallow foundations on a deposit with a liquefied soil layer underlying a crust

This section is focused on the bearing capacity verification of a shallow footing on a two-layered deposit, with a surface crust layer and a supposed liquefied layer below.

The upper layer had the same properties of the soil used for the homogeneous clay model and represented the stiff crust, while the lower layer simulated the condition of a hypothetically liquefied or partial liquefied soil under seismic actions.

As explained in previous chapters, the phenomenon of liquefaction induces a shear strength reduction in non-cohesive saturated soils due to the excess pore pressure build up associated to earthquake actions. It leads to a temporary static bearing capacity degradation for the supporting soil underlying shallow foundations and potentially a soil shear failure during the seismic excitation resulting in very large settlements.

Since the modelling was loaded statically, the soil was set to approximate values for strength and stiffness, assuming a specific level of pore pressure build up.

As a matter of fact, the potential of soil to develop excess pore pressure is altered by the presence of the overlying structure in comparison with the free-field condition. In fact, the mean effective stress in the soil increases due to the presence of the building, leading to lower increment of pore pressures in the liquefiable layer during the cyclic action. In order to take into account of this aspect, it was supposed that the fully liquefaction in the

lower layer of the deposit corresponded to a value of the excess pore pressure build-up ratio, U , equal to 0.95 instead of 1.

The shear strength reduction in the weaker (liquefied) layer was achieved through a degradation of the angle of shearing resistance, corresponding to a degradation of the Factor of Safety during the shaking. The reduced angle of shearing resistance was calculated as a function of the actual angle of shearing resistance in pre-liquefaction condition, and of the excess pore pressure ratio, using the analytical expression suggested by Cascone and Bouckovalas, 1998:

$$\varphi_{\text{deg}} = \tan^{-1}[(1 - U)\tan\varphi] \quad (3.18)$$

Considering that the excess pore pressure ratio represents a common parameter to quantify the liquefaction triggering, its values were assumed proportional to the stiffness degradation. The stiffness degradation was simulated through a reduction in the shear wave velocity, thus proportional to G_{max} . This maximum value of the shear modulus reduction followed the suggestions of Karatzia et al., 2017 who was investigating the change in foundation impedance due to liquefaction.

The initial value of the shear wave velocity was calculated equal to 233 m/s ($V_{s,\text{ini}}$), according to the characteristic stiffness value of the crust and it was reduced first of 4 times and then of 10 times to represent respectively the partial and the total liquefaction in the lower layer.

The two resulting values of the shear wave velocity were adopted for the calculation of the shear moduli in partially and totally liquefied layer, as follows:

$$G_{\text{liq},1} = \rho \left(\frac{V_{s,\text{ini}}}{4} \right)^2 \quad (3.19)$$

$$G_{\text{liq},2} = \rho \left(\frac{V_{s,\text{ini}}}{10} \right)^2 \quad (3.20)$$

Where ρ is the soil density. Their values were equal to 5,9 MPa and 0,95 MPa.

The corresponding excess pore pressure ratios assumed for the partial and total liquefaction were chosen respectively equal to 0,8 and 0,95, leading to the resulting degraded angles of shearing resistance of 8° and 2° , respectively, according to the

equation 3.18. The assumed values of the excess pore pressure ratios for each value of the degraded stiffness derived from a rough approximation of the real behaviour of a liquefied soil. The cyclic behaviour of a liquefied soil (conceptually described in Figure 3.10) is different from non-liquefiable soils. In fact, in non-liquefied soils the initial tangent shear stiffness smoothly decreases with the increasing strain, as illustrated in Figure 3.10.

In liquefiable soils the increasing number of cycles leads to a pore pressure build-up therefore, for a specific cycle corresponding to a specific value of the excess pore pressure ratio, the stiffness measured at very low strains drops to very small values and conversely increases at high strain levels.

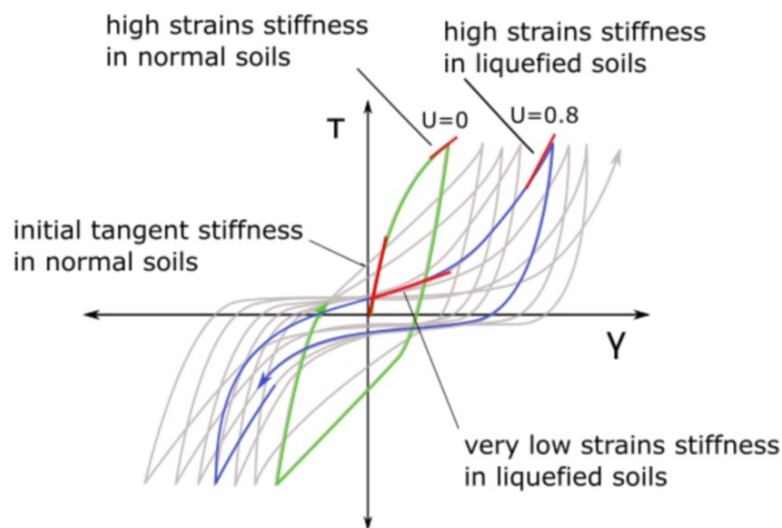


Figure 3.10 – Non-liquefied and liquefied soil behaviour.

In order to capture this condition, an equivalent behaviour was assumed in between the two extreme stiffness levels in correspondence of $U=0,8$ and between the two stiffness levels in correspondence of $U=0,95$ and a new stiffness at very low strains was assumed for the partially liquefied soil and for the totally liquefied soil. In Figure 3.11 an illustration was presented for the sole purpose of clarifying. This is deliberately inconsistent with shear modulus to vertical effective stress relationships that are commonly adopted in non-liquefying conditions (Equation 3.21) that could be adapted to account for pore pressure build up (Equation 3.22) (Kramer, 2016). This equation would only predict a stiffness reduction of 10% at a $U=0,9$. This level of reduction is inconsistent

with experimental results which show dramatic reduction at lower levels of U (e.g. Ishihara 1985), and therefore the suggested values from Karatzia et al., 2017 were adopted.

$$G_{\max} = G_0 \left(\frac{\sigma'_m}{p_a} \right)^n \quad (3.21)$$

$$G_{\max} = G_0 \sqrt{\left(\frac{\sigma'_{m0}(1-U)}{p_a} \right)} \quad (3.22)$$

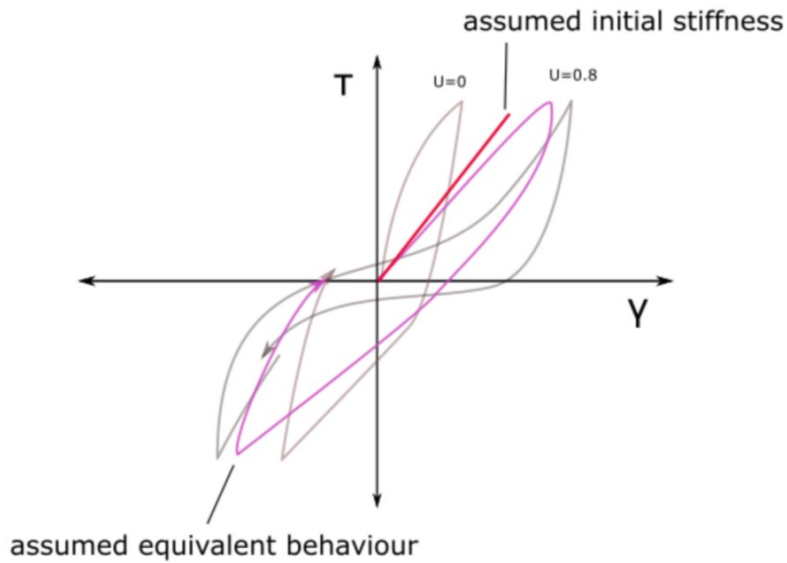


Figure 3.11 – Example of the assumed equivalent liquefied behaviour.

Moreover, the liquefied layer was characterised by a null angle of dilatancy in order to represent the purely contractive behaviour of the soil.

A parametric study was performed by changing the soil parameters in the lower layer (corresponding to the partial and total liquefaction) and the top layer thickness. The crust height varied from 1,5 meters to 3 meters, and for each variation two different deposit conditions were considered.

The crust properties for all the analyses were set exactly the same as in the validation section for the sandy soil.

Supposing that in static analyses the initial stiffness represented by G_{\max} for the crust and $G_{\text{liq},1}$ and $G_{\text{liq},2}$ for the partially and totally liquefied layer can be confused with the respective G_{ur} and assumed as the real elastic stiffness of the soil layer, it was possible to compute the input parameter for the HS model in PLAXIS, $E_{\text{ur}}^{\text{ref}}$, with the relationship:

$$E_{ur}^{ref} = 2G_{ur}(1 + \nu) \quad (3.23)$$

and from it, E_{50}^{ref} and E_{oed}^{ref} dividing by 3, both for the crust layer and for the liquefied layer.

In all the analyses, the FE mesh in correspondence of the material interfaces was increased of 4 times compared with the model mesh because of high differences in stiffness and strength of the materials that lead to stresses and strains gradients, which implies higher stress-strain distribution.

As in the previous analyses the applied vertical load corresponded to an approximation of the value calculated from analytical relationships thus, before performing any numerical computation a theoretical solution was required.

The geometry of the models is shown in Figure 3.12 and Figure 3.13 below.

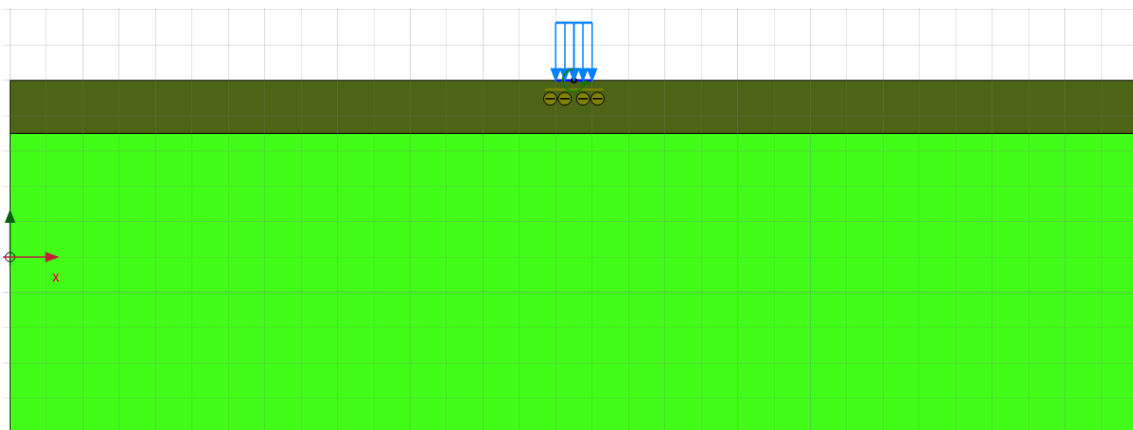


Figure 3.12- Numerical model of the layered deposit. H crust=1,5 meters.

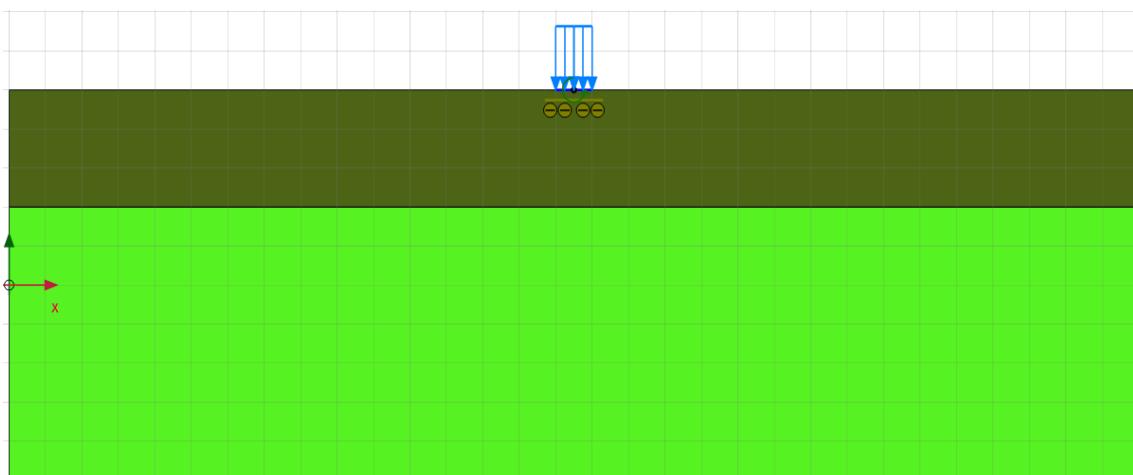


Figure 3.13- Numerical model of the layered deposit. H crust=3 meters.

Verification

In the Table 3 and Table 4 below the analytical solutions, obtained with Meyerhof and Hanna, 1978 and the numerical results are summarised and compared, for partially and totally liquefaction conditions and in function of the crust thickness.

	Meyerhof and Hanna (1978) [kPa]	Numerical solutions [kPa]	Percentage difference [%]
$V_{s,1}/V_{s,liq}$	Crust height [m]		
	1,5		
4	83	82	1,2
10	53	51,6	1,9

Table 3 – Analytical and numerical solutions for H crust= 1,5 meters.

	Meyerhof and Hanna (1978) [kPa]	Numerical solutions [kPa]	Percentage difference [%]
$V_{s,1}/V_{s,liq}$	Crust height [m]		
	3		
4	225	217	3,7
10	164	160	2,5

Table 4 – Analytical and numerical solutions for H crust= 3 meters.

For all the analysed cases the difference between the analytical and numerical solutions is less than 5%, meaning a good agreement.

Finally, a comparison between the load-displacements responses from the homogeneous soil model and from the layered deposit, where the top layer has the same properties of the homogeneous soil, was done and the results are presented in Figure 3.14.

It is evident that all the values of displacements obtained from the layered soil analyses are higher than the displacements recorded in the homogeneous case, due to the increase of deformability of the lower layer. In particular, in correspondence of a stiffness reduction of 10 times the original one, meaning “total” liquefaction, the foundation measured vertical displacements are very high for moderate values of the applied load. In fact, this condition represents an extreme reduction in stiffness that potentially can be reached during the earthquake shaking.

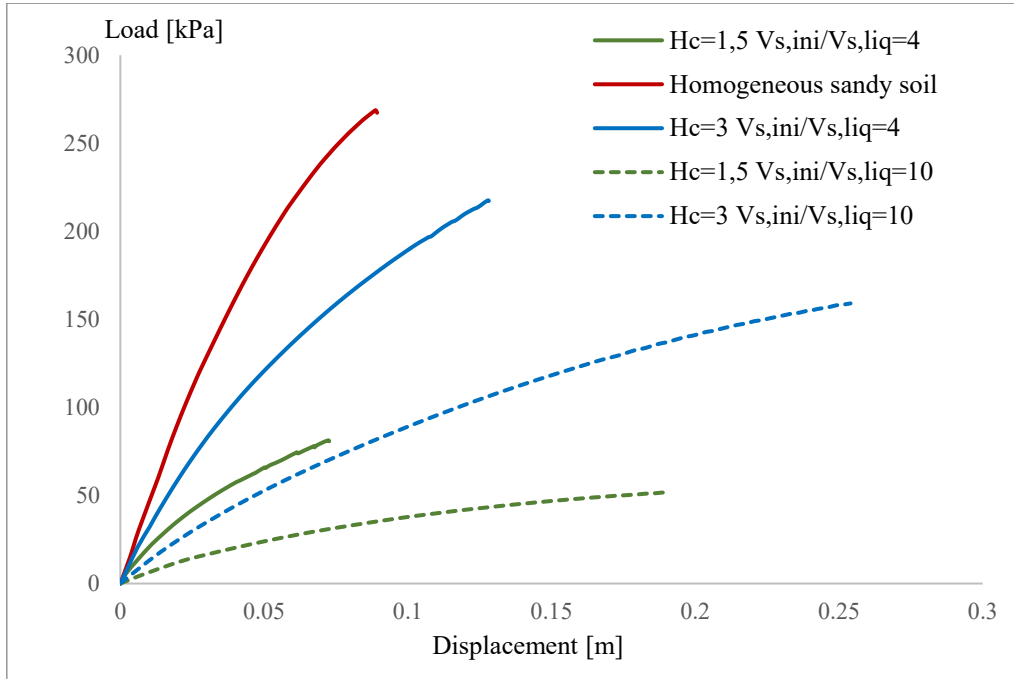


Figure 3.14- Load-displacements curve for two layered deposits with liquefied layers.

Moreover, in correspondence of the same stiffness reduction, a degraded angle of shearing resistance equal to 2° was set, meaning a decrease of more than 15 of the actual value for the bottom layer. However, the degradation of the bearing capacity is not linearly proportional thanks to the presence of the stiffer layer at the top of the model. In fact, the higher the height of the crust is, the lower the decrease in the foundation bearing capacity, which is a consequence of the reduction of the soil strength and stiffness parameters as a simplification of the liquefaction development in the lower layer.

The presence of the “crust” mitigates the consequences of the liquefaction on the supporting soil, and thus, the use of shallow foundations is possible in liquefiable soils, as far as the natural surface layers (the crust) are sufficiently stiff and resistant, or they are artificially improved (Bouckovalas, 2017).

3.5 Conclusions

Common geotechnical problems about the ultimate bearing capacity of shallow foundations have been performed, both to validate the numerical model of a layered deposit with a liquefiable layer, useful for modelling the soil in the following push-over analyses and for verify the accuracy of the numerical results in terms of maximum axial load. Simplified soil models and geometries have been used in order to make the final

results as general as possible, without differing too much from analytical solutions. The liquefaction of the lower layer in the analyses involving 2-layered deposits has been simulated making a simple assumption of the strength and stiffness of the liquefied soil because the modelling of the excess pore pressure build-up that causes liquefaction in granular saturated soils, currently represents one of the main challenges in this field of research.

It was concluded that:

- All the results obtained from the parametric study show a good agreement with the analytical solutions through consolidated theoretical formulations (Meyerhof and Hanna, 1978).
- The presence of a totally or partially liquefied layer tends to reduce the soil mechanical features with a consequent decrease of bearing capacity, less accentuated and almost null with an increase in the height of the upper stiffer layer.
- the plots in Figure 3.14 show an evident increase of the amount of vertical settlement with the increase of $V_{s,ini}/V_{s,liq}$ ratio, meaning the transition from partial to full liquefaction even though the achievement of a lower value of the ultimate bearing capacity. The ground failure is achieved earlier in the cases where the liquefied layer has a significant influence on the whole soil behaviour (in the full liquefaction case or when the stiff crust is relatively thin) with a corresponding greater accumulation in settlements.
- Further numerical analyses are required, dealing with different values of the stiff crust thickness in order to find the influence of liquefaction on bearing capacity and settlement.

4. Chapter: Moment-Rotation response of shallow foundations

4.1 Introduction

Current seismic design approaches of structure-foundation systems assume a linear or equivalent-linear elastic soil behaviour and perfect contact between foundation and soil, without considering non-linear phenomena that inevitably affect the response of the whole soil-foundation-structure system during earthquake excitations potentially producing large displacements and changes to the distribution of stresses in the structure (Behnamfar, F., & Banizadeh, M. (2016). Recently, there is a considerable evidence that the soil-foundation behaviour can be reliably predicted in terms of nonlinear stiffness, foundation moment capacity, level of settlement and residual tilt (Deng and Kutter, 2012; Liu et al., 2013), although these estimations of that performance have not yet been developed for liquefiable soils.

In a general case, the estimation of foundation rotational stiffness and residual tilt can be determined based on the contributions from three separate rotation mechanisms (elastic deformation, foundation uplift and soil yielding (see Figure 4.1):

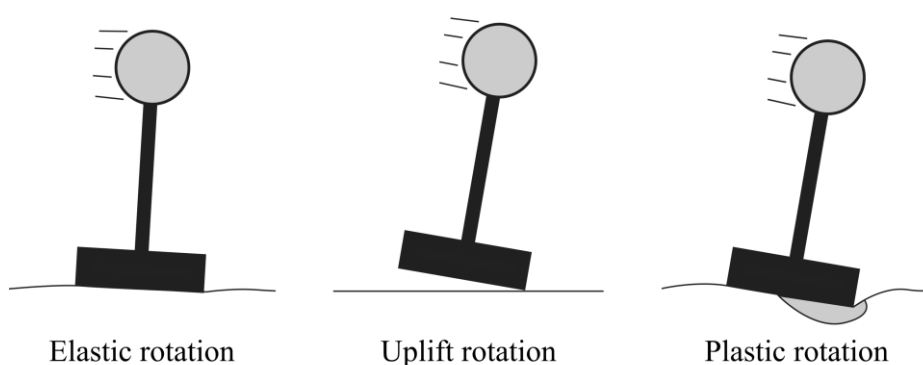


Figure 4.1- Mechanisms of foundation rotations.

- Elastic rotation, a linear elastic mechanism. The removal of the load allows the full recovery of the rotation and the elastic stiffness depends only on the footing dimensions, the initial shear modulus (G) and Poisson's ratio (ν) of the soil.

- Foundation uplift is a geometric non-linearity mechanism. Also, in this condition the deformation is fully recoverable, but the rotational stiffness is characterised by a progressive reduction of stiffness due to the change in contact between the soil and foundation.
- Soil yielding is a non-linear inelastic mechanism. The deformation is not recoverable and the stiffness changes as the soil yields.

Finite Element simulations are one way to account for the SFSI effects in the response assessment of shallow founded buildings and to catch the complexity of the phenomena. The scope of this chapter is to present the results for the non-linear static moment-rotation response and the rotational stiffness degradation curves of shallow foundations on both homogeneous and layered soil deposits obtained through finite element push-over analyses. Simplified models with pseudo static loads in place of seismic excitation (Figure 4.2) and simplified models to describe the soil behaviour have been adopted in order to find results as generalised as possible.

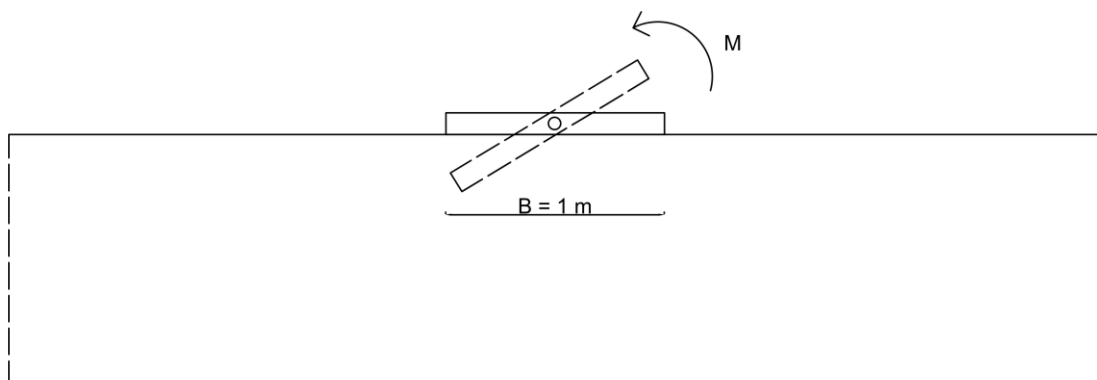


Figure 4.2- Cross section of the problem.

The moment-rotation curves represent a key step in the quantification of the system response accounting for non-linear SFSI effects, through displacements-based procedures (e.g. Millen, 2018), currently not easily available in literature, especially in the specific case of layered deposits with a liquefiable soil layer.

The first step of the study has been the validation of the numerical model through the comparison with analytical simplified models described in the literature such as the models presented in Chatzigogos et al. (2011) and Gazetas et al. (2013), belonging to the group of macroelement formulations, for the cases of linear elastic soil behaviour and inelastic cohesive soil deposit. The work exposed in Gazetas et al. (2013) has been useful

also as a reference for the development of the effective rotational stiffness degradation curves, but only for cohesive soils in undrained conditions.

However, the main objective of the current work is to provide a series of numerical solutions for the moment-rotations response of shallow foundations on soils with frictional behaviour, typical of sands and potentially sensitive to the phenomena of liquefaction.

Therefore, various numerical analyses have been performed considering shallow foundations on purely frictional soil deposits and on a two-layered deposit where the lower layer was modelled with strength and stiffness parameters typical of a liquefied or partially-liquefied soil, in the same way explained in section 3.4 for the ultimate bearing capacity problems. In particular, the potentially liquefiable soil layer when subjected to earthquake actions, has been modelled by decreasing the reference values of stiffness and strength as described previously.

At the end, a parametric study was carried out varying the upper stiffer layer (also called “crust”) thickness and demonstrating how this parameter affected the foundation response in layered deposits where the lower layer is the weaker one (the liquefied one).

4.2 Literature review

There is a rich literature on simplified models for the description of soil-foundation system behaviour that can be distinguished in two main groups: the macroelement models and the models based on Winkler theory. In the first case the shallow foundation and the underlying soil are considered as a single “macroelement” and a 3 degree-of-freedom, DOFs, 2D model is formulated describing the resultant force-displacement behaviour of the centre of the footing in vertical, horizontal and rotational directions; in the second case the soil is treated as a bed of decoupled springs each one with an appropriate constitutive law. The Winkler theory is subjected to a number of limitations such as the description of the coupling of the vertical/rotational and horizontal displacements of the foundation. Therefore, the macroelement models are the one followed for modelling shallow foundations behaviour in the reference models used for the validation procedure in the current study.

According to Chatzigogos (2011), each mechanism involved in shallow foundation and soil interaction is modelled independently and then, the mechanisms that are relevant for the specific application are coupled together in order to achieve the ultimate condition as

their combined result. The model has been formulated for strip or circular rigid shallow foundations subjected to static forces (Figure 4.3); it has been implemented and validated for static loads and for cohesive behaviour of the soil.

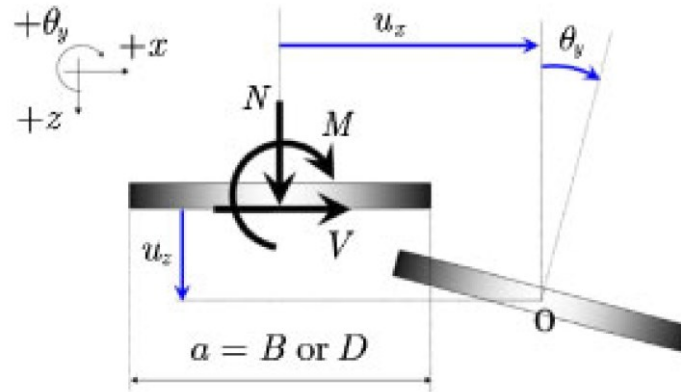


Figure 4.3-Forces and displacements for the macroelement model (adapted from Chatzigos, 2011).

Case 1: Elastic soil and no-tension interface

One of the simplest cases analysed in Chatzigos (2011), considers a strip footing subjected to a vertical force and moment, overlying a linear elastic half-space; the soil-foundation interface is modelled as rough and with zero tensile strength, in order to avoid the foundation sliding but to allow the vertical detachment from the soil surface. In this way, even with the soil linearity, there is a geometric non-linearity due to the uplift that modifies the contact area and consequently the static impedances of the foundation; in fact, before the foundation vertical detachment the response is linear with a constant tangent elastic stiffness matrix $[K]=[K_0]$; once the uplift starts, modifying the soil-foundation contact area, the tangent elastic stiffness matrix becomes a function of the elastic displacements, ϑ_{el} .

The moment of uplift initiation can be estimated with a linear relationship:

$$M_{\text{uplift}} = \pm \frac{1}{\alpha} N_{\text{app}} B \tag{4.1}$$

where N_{app} is the vertical applied load, B is the foundation width and α is a numerical parameter depending on the foundation shape; the moment-rotation non-linear response can be determined using the following expression:

$$\frac{M}{M_{\text{uplift}}} = \beta - (\beta - 1) \left(\frac{\vartheta_{\text{el}}}{\vartheta} \right)^{\frac{1}{\beta-1}} \quad (4.2)$$

where M is the applied moment, ϑ is the foundation rotation after the uplift initiation, β is a numerical parameter depending on the foundation shape and ϑ_{el} is the elastic rotation computed as the ratio between M_0 and the tangent elastic rotational stiffness K_0 whose formulation is presented in Gazetas (1991), being for a strip footing equal to:

$$K_0 = \frac{\pi G \cdot B^2}{8(1 - \nu)} \quad (4.3)$$

Where G is the soil shear stiffness.

Case 2: Inelastic (cohesive) soil and no-tension interface

In a condition where the shallow foundation with no tensile strength is placed on a soil whose behaviour is characterised by a specific strength criterion, meaning a limitation in admissible stresses, a different kind of non-linearity takes place. In cohesive soils in undrained conditions, when the shear strength, represented by the cohesion c , is exceeded due to the foundation load, the soil develops plastic deformations and dissipates energy, introducing a non-linearity of material origin in the system, coupled to the geometric one produced by the uplift. The coupling is achieved considering that for each increment in forces there is a correspondent increment in displacements that can be composed by an elastic part and a plastic one. Moreover, the combination of material and geometric non-linearity means a non-linear trend since the very low values of the applied forces, making more complex the estimation of the uplift initiation. Crémer et al. (2001) proposed an analytical formulation for the estimation of the moment of uplift initiation:

$$M_{\text{uplift}} = \pm \frac{N_{\text{app}} B}{\alpha} e^{-\zeta \frac{N_{\text{app}}}{N_{\text{max}}}} \quad (4.4)$$

where N_{max} is the ultimate vertical load in the soil and ζ is a parameter depending on the soil plasticity law and varies in the range 1,5÷2,5.

A useful study to catch the main elements for a numerical push-over analysis in an inelastic homogeneous soil was carried out in Gazetas (2013), but is limited, as already referred, to the case of cohesive soils in undrained conditions. According to the

aforementioned study, there is a strong dependency between the $M-\vartheta$ response and the applied axial load, meaning a more or less marked superposition of the two types of non-linearities that affects the chance to identify the right value of the angle of rotation in correspondence of the uplift initiation and the detachment of the foundation from the soil surface.

Through a set of numerical simulations on different models with various foundations shapes, the rotational effective stiffness curves have been generated and a normalisation has been proposed. In particular, the effective stiffness was normalised by the numerical value of the small-strains rotational stiffness in correspondence of the specific N_{\max}/N_{app} ratio investigated, showing one of the main issues of this kind of analyses to find out a common analytical relationship to describe the rotational stiffness degradation for all the loading conditions.

However, the study by Gazetas (2013) show a low dependency of the response on the foundation shape when the stiffness reduction curves are normalised and this is the reason why in the current work of this section a strip foundation has been chosen for simplicity.

The ultimate moment capacity

The ultimate moment capacity represents the maximum moment that the foundation can experience immediately before a failure. In Deng et al. (2014) an empirical relationship (Equation 4.5) has been proposed for rectangular shallow foundations to compute the ultimate moment capacity of shallow foundations overlying homogeneous soil deposits, depending on the Critical Contact Area ratio, ρ_{ac} . This one is the ratio between the minimum area required to support the applied vertical load when the soil's ultimate bearing capacity is fully mobilized, called Critical Area, A_c , and the entire foundation area.

$$M_u = \frac{N_{\text{app}}B}{2} \left(1 - \frac{A_c}{A} \right) \quad (4.5)$$

The ultimate moment capacity is a function of the applied vertical load, in case of a strip footing where $L \rightarrow \infty$, the ratio is expressed in terms of the foundation base (Equation 4.6) where B represents the total width of the foundation base and B_c is the partial width of the foundation kept in contact with the soil surface in a condition of eminent overturning due to the application of M_u .

$$M_u = \frac{N_{app}B}{2} \left(1 - \frac{B_c}{B}\right) \quad (4.6)$$

The Critical Contact Area ratio, ρ_{ac} , is not directly related to the factor of safety due to the dependence of bearing stress on foundation size, but Deng and Kutter, 2012, through results from centrifuge model tests of rocking foundations embedded in dry sands, proved that in many cases the ratio, ρ_{ac} , is related to the factor of safety as its inverse, as shown in Equation 4.7, but in some cases it is different. They asserted that the formula in Equation 4.5 is more appropriate and the results obtained in the current work and explained in section 4.6 demonstrate it.

$$M_u = \frac{N_{app}B}{2} \left(1 - \frac{1}{FS}\right) \quad (4.7)$$

4.3 Model Validation: No tension interface and linear elastic deposit

The push-over analyses were performed with the commercial code PLAXIS 2D. This software, based on finite element method, is able to capture soil-foundation-structure non-linearity. The validation was executed on a model characterised by the presence of a strip footing, of unit width, on a linear elastic half-space and verified through the comparison with the model of Chatzigogos (2011), presented in Section 4.1.

Model inputs

The footing was modelled as a rigid, massless plate with a rough interface characterised by a null tensile strength in order to be not allowed to slide but to be able to detach from the soil surface. The foundation features are the same used in the bearing capacity problem presented in the previous chapter (Table 1). The soil was modelled as a linear elastic half-space and its features are summarised in Table 5.

Parameters	
Soil Model	Linear elastic
Drainage type	Drained
γ_u [kN/m ³] dry unit weight	17,5
γ [kN/m ³] saturated unit weight	19,5
e_0 [-] void ratio	0,7
E [MPa] Young's modulus	23,8

ν [-] Poisson's ratio	0.3
G [MPa] Shear modulus	10

Table 5 – Soil input parameters.

In PLAXIS 2D the elastic stiffness modulus, E_i , and the Poisson's ratio, ν , are the input stiffness parameters for the Linear Elastic model and for the Linear Elastic Perfectly Plastic (Mohr Coulomb) Model. According to the manual (PLAXIS, 2017) the input value of the elastic stiffness modulus is the Young's modulus.

The earth pressure coefficient was automatically computed through Jaky's Law.

Model construction

As in the previous analyses, the numerical project started by creating the geometry of the model and by setting the project properties. For the push over analyses a plane strain deformation was chosen, leaving the other initial project properties as the default ones. The full domain was modelled rather than using an axis symmetric boundary, due to the loss in symmetry related to the foundation rotation. The domain size was chosen equal to the one used for the bearing capacity problems, with a 15 metres length for each side starting from the external corner of the plate and a depth of 10 metres, as validated in previous models. Actually, in push-over analyses the domain could even be smaller compared with the one of bearing capacity problems but for simplicity it has been chosen the same.

The lower boundary was fully fixed and the side boundaries were normally fixed while the upper boundary was free to simulate the free field.

Once the geometry and the deformation conditions were defined, a definition of the soil stratigraphy was needed, through the *Boreholes* tool in PLAXIS 2D. In this case of linear elastic half-space only one layer was defined and the top and bottom coordinates were introduced.

The "linear elastic" model was selected and all the properties were entered as referred in Table 2. The tension cut-off was selected and a tensile strength, σ_t , equal to zero was defined in order to promote the detachment after the uplift initiation.

The footing was added to the model as a structural element called Plate. It was placed in the centre of the plan and it was delimited by two vertices. The footing properties were defined according to Table 1. As a massless element it does not induce a change in soil stresses and strains, therefore, in order to follow the macroelement model explained in Chatzigogos (2011), a vertical point load was added in the model together with a moment

applied in the central point of the foundation. The vertical load represented the gravitational component while the moment represented all the possible perturbations that combined together lead to the foundation tilting. The input parameters are the ones summarised in the Table 6.

Parameters	Interface
Soil Model	Hardening
Drainage type	Drained
γ_u [kN/m ³] dry unit weight	17,5
γ [kN/m ³] saturated unit weight	19,5
e_0 [-] void ratio	0,7
ϕ [°] angle of internal friction	35
E_{ur}^{ref} [MPa] unload/reload. stiffness modulus	23,8
E_{50}^{ref} [MPa] secant stiffness in standard triaxial tests	7,9
ν [-] Poisson's ratio	0.3
σ_t [kPa] tensile strength	0
K_0 [-] earth pressure coefficient	0,441

Table 6 – Soil/foundation interface input parameters.

To complete the definition of the soil model, an interface element under the foundation was added to model the soil-footing interaction. The interface was set as *rigid* with a corresponding unit value of the factor R_{inter} and the gap closure was not considered. The material model chosen for the interface was hardening soil model with a null tensile strength in order to be able to reproduce the detachment from the soil surface after the uplift initiation. The angle of internal friction was deliberately set high in order to limit the horizontal displacements.

The Finite Element mesh was created with a finer discretization but taking care to first assure the mesh in correspondence to the elements of the structural or interface elements, in correspondence with the material interface in order to let the computation continuously follow the strains and stresses changes from an element to the adjacent one.

Model execution

The numerical simulation of the moment-rotation response was performed considering the footing subjected to a fixed normal load applied in the centre, as a fraction of the ultimate bearing capacity depending on the factor of safety chosen, and to a moment increasing step by step from zero to a value close to the ultimate condition (M_u , computed

with Equation 4.7). However, in elastic conditions, the ultimate vertical load is never reached thus, an arbitrary value of 150 kN was chosen for the vertical force and a value of 75 kNm/m² was set as the maximum moment to apply. The analysis was performed in 3 different stages:

- Initial phase: the calculation type was “K₀ procedure” in which there is the direct generation of initial effective stresses, pore pressure and state parameters, according to PLAXIS, 2017 manual. In this stage all the loads, structures and interfaces were deactivated.
- Phase 1: the calculation type was “Plastic” meaning an elastoplastic drained (or undrained) analysis. This phase started at the end of the initial phase and it was used to simulate the response of the system subjected to a pure vertical load, N_{app}, so the plate, the interface element and the vertical load were activated. The numerical parameters were the default ones, the displacements and deformations were reset to zero and the tolerated error was set to a value equal to 0,01.
- Phase 2: for this stage the calculation type was “plastic”; however, only for the examined case of linear elastic soil because, since it did not deal with the plasticisation of the points, so as to the failure never be reached. For the cases of elastoplastic materials, the plastic calculation was not sufficient to follow the deformation process with accuracy, for what a “dynamic” calculation had to be chosen.

This phase was subsequent to the Phase 1, even though the displacements and the deformations were reset to zero. The vertical load, the structural elements and the interface elements were already activated from the previous stage, while the moment being activated in correspondence, with a value of 75 kNm/m².

Three different points were monitored for the final results, the central point and the two corners.

Output inspection

After the execution of the numerical simulation the inspection of the output results was done to check if the model worked correctly. In Figure 4.4 (a) a focus on the deformed system (200 times amplified) is illustrated.

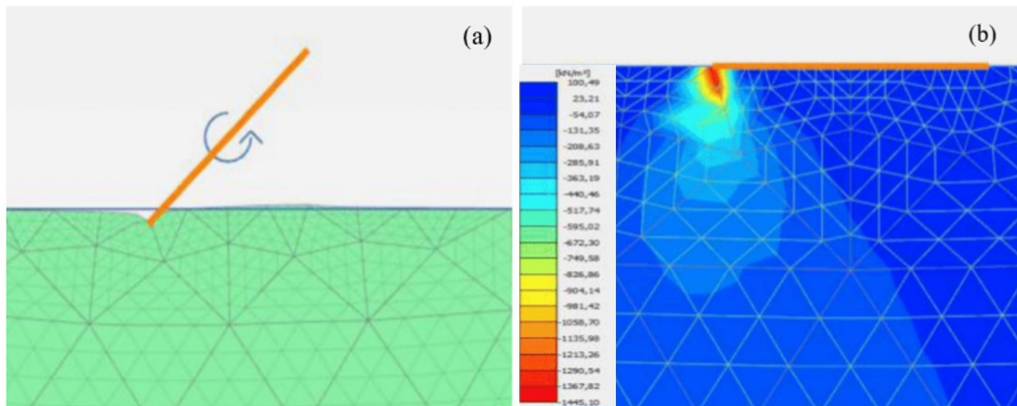


Figure 4.4 – (a) Output of the numerical analysis; (b) State of stress below the foundation.

As expected, the detachment of the foundation from the soil occurred and the contact area has been greatly reduced. It means that the applied moment exceeded the moment of uplift initiation equal to 37,5 kNm (see Figure 4.5), producing a high reduction in the static impedance of the soil-foundation system, but never reaching the ultimate state because of the elastic soil constitutive law.

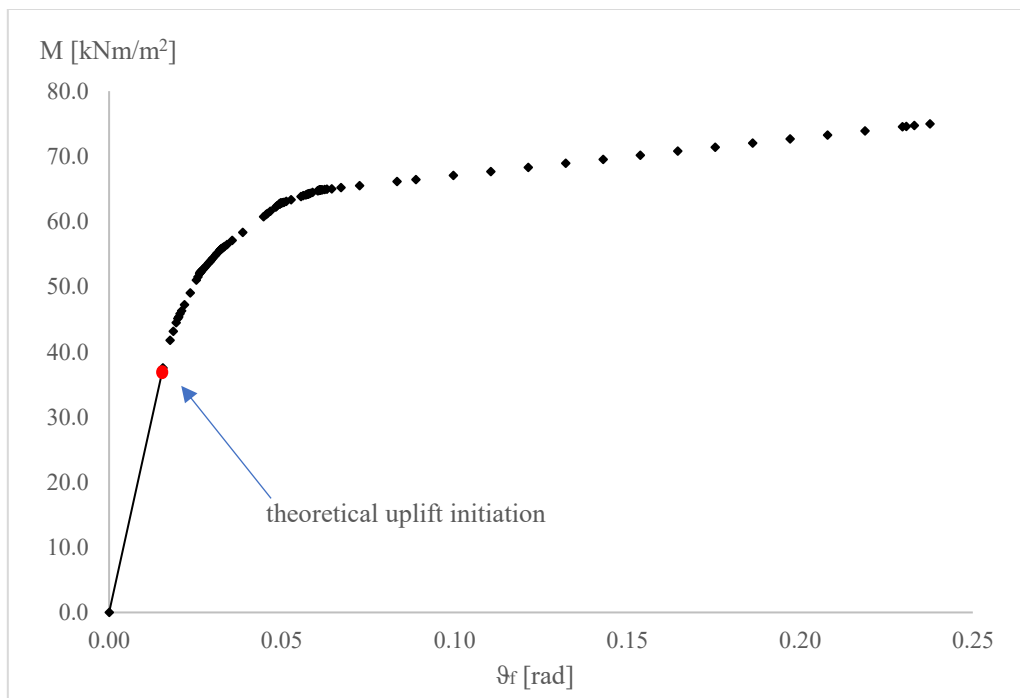


Figure 4.5- Moment-rotation behaviour and theoretical uplift value.

Moreover, the cartesian vertical stresses (σ_y) was verified in order to check the tension cut-off in correspondence of the detached corner; it showed zero values, accounting for

the small error in the right corner (Figure 4.4(b)) and an accentuated compressive state of stress in the left corner.

Numerical results

The moment-rotation response was indirectly estimated from the analysis results; the final results from a “plastic” calculation were expressed through $\Sigma Mstage$ -vertical displacements plots in the specific monitored point for the specific stage of interest (*Phase 2*). $\Sigma Mstage$ represented a percentage of the applied resultant load, meaning a combination of the vertical force and the moment; its value ranged between 0 and 1, where 1 represented the 100% of the applied resultant load. The incremental values of the foundation rotation were calculated for each i-step as the difference between the incremental vertical displacements registered in the two edges of the foundation base, divided by the base width, counting on the perfect flexural rigidity of the foundation, which will result:

$$\vartheta_{f,i} = \frac{(u_{yi}^L - u_{yi}^R)}{B} \tag{4.8}$$

The incremental values of the moment, $M_{f,i}$ were calculated, only considering the “plastic” analysis validated as described, as the product of each $\Sigma Mstage$ by the input value of the moment equal to 75 kNm/m². The plot in Figure 4.6 shows the foundation rotational response on a linear elastic half-space.

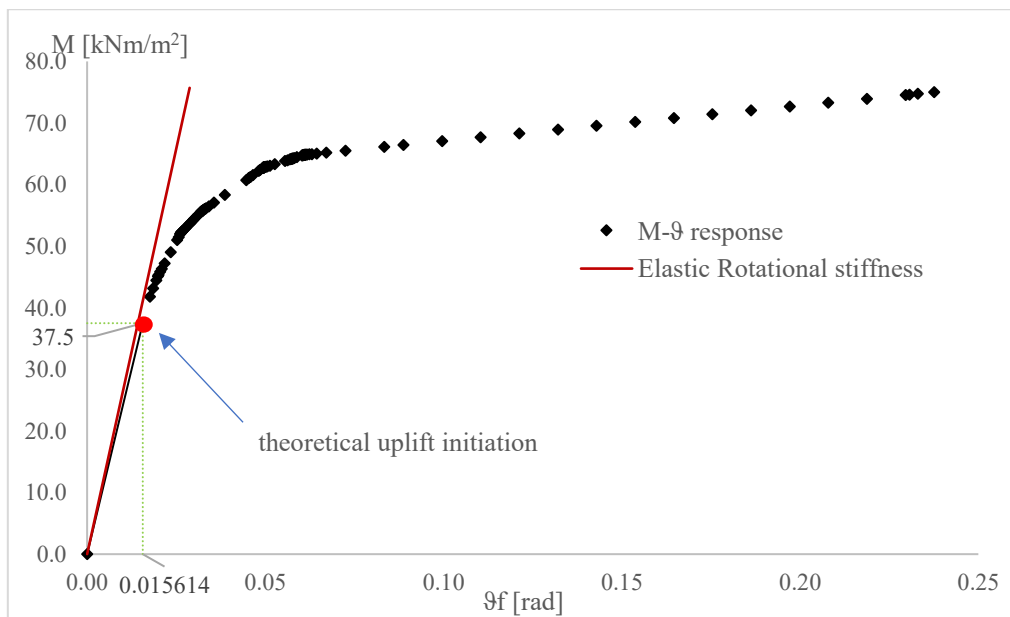


Figure 4.6 – Moment-rotation response of a shallow foundation on a linear elastic half-space.

Since the system displacements and rotation take place without any detachment from the soil surface, the response is linear, as expressed by the first part of the plot, then a progressive and clear drop of the tangent rotational stiffness with a nonlinear trend proves the initiation and progress of the foundation uplift. According to the numerical results, the value of the moment at the uplift initiation is about 37 kNm/m².

Verification

First, the flexural rigidity of the foundation was verified in order to avoid structural deformation and to be sure of the procedure applied for the rotation estimation. For this purpose, the moment-rotation response of the two halves of the entire foundation basis were plotted and superimposed, computing the rotation as the difference between the central point vertical displacement and the right/left corner vertical displacement divided by half of the foundation width. As shown in Figure 4.7 there is a perfect superposition, meaning a perfect flexural rigidity EI.

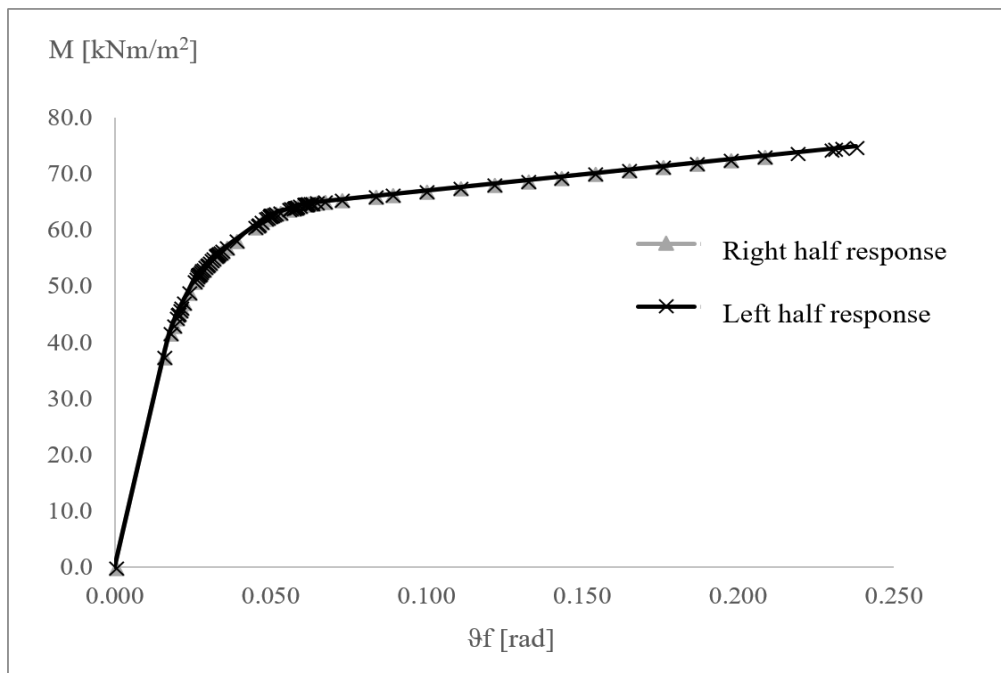


Figure 4.7 – Verification of the footing flexural rigidity.

Then, the numerical results were checked through the comparison with the analytical model proposed in Chatzigogos (2011). The tangent elastic rotational stiffness, K_0 , was calculated following the relationship 4.3 in function of the shear modulus, G . The analytical value was equal to 2620 kNm; it was used to compute the analytical values of the incremental moment which were superimposed in the plot in Figure 4.6 (red line)

showing a satisfying congruence between the analytical elastic response and the numerical one. The numerical rotational stiffness estimated was about 2410 kNm, a value close to the analytical one taking into account the calculation errors in numerical simulations.

The formulation 4.1 was used to calculate the moment corresponding to the uplift initiation, resulting in a value of 37,5 kNm/m² in good agreement with the numerical one. Finally, the numerical moment-rotation response was compared with the analytical one, estimated by Equation 4.2 for the calculation of the moment values after the uplift initiation, when the non-linear behaviour started and the static impedances were modified. The results are illustrated in Figure 4.8.

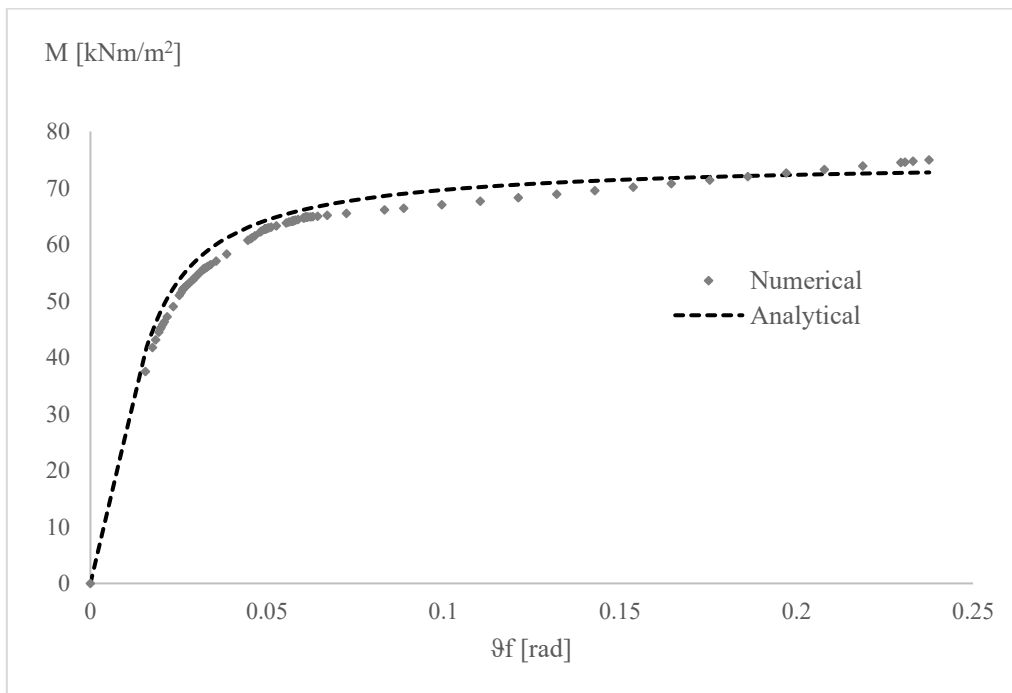


Figure 4.8 – Comparison between numerical results and analytical solution.

The agreement between the finite element solution and the reference model is very satisfactory showing a maximum deviation not exceeding the 4%, proving that the developed validation procedure was successful and the numerical model built was suitable for the following, more complex analyses.

4.4 Moment-rotation response of a footing on a homogeneous inelastic soil: Cohesive material (clay)

In this section a description of a set of push-over analyses performed with PLAXIS 2D about shallow strip foundations over an inelastic homogeneous soil was carried out.

Each analysis differs for the amount of the applied resultant load, as a fraction of the ultimate one in order to capture how the foundation behaviour strongly depends on the factor of safety (FS).

Model inputs

This study deals with a shallow strip foundation overlying a 10 metres depth homogeneous cohesive soil layer, with an undrained shear strength S_u and a maximum shear modulus G_0 . The footing was modelled as a rigid, massless plate with a rough interface characterised by a null tensile strength as in the previous analysis (section 4.1) and all the features are summarised in Table 1. The water table was neglected.

The cohesive soil was modelled with a material following the classical Tresca criterion in which the shear strength S_u varies linearly with depth. The material model chosen in PLAXIS 2D to better describe the soil behaviour was the Hardening Soil Model (HSM), an advanced model for simulating different types of soil, both soft and hard soils (Schanz, 1998), which is formulated using hyperbolic stress-strain curves with stress dependent stiffness inputs to simulate realistic soil behaviour. In PLAXIS Hardening model reference values were needed for the elastic stiffness which means elastic moduli in correspondence of a value of 100 kPa of the confining pressure, p_{ref} , in a triaxial test. Therefore, the values of the stiffness were expressed in terms of the unloading and reloading stiffness modulus E_{ur}^{ref} and the secant modulus at the 50% of the peak shear strength, E_{50}^{ref} set equal to the oedometer modulus. The Poisson's ratio for unloading/reloading was left with its default value equal to 0,2.

The input soil parameters are collected in Table 7.

Parameters	Interface
Soil Model	Hardening
Drainage type	Undrained (B)
γ [kN/m ³] dry unit weight	17,5
γ_u [kN/m ³] saturated unit weight	19,5
e_0 [-] void ratio	0,7

S_u [kPa] undrained shear strength	85
E_{ur}^{ref} [MPa] unload./reload. stiffness modulus	23,8
E_{50}^{ref} [MPa] secant stiffness in standard triaxial tests	7,9
ν [-] Poisson's ratio in unloading condition	0,2
σ_t [kPa] tensile strength	0
OCR over-consolidation ratio	2
p_{ref} [kPa] reference confining pressure	100
m [-] power for stress level dependency of stiffness	1

Table 7- Cohesive soil input parameters.

Model construction

All the project properties, the geometry and size of the domain and the boundaries conditions are the same described in the previous analysis. The soil stratigraphy was defined by the *Boreholes* tool, creating a new material described by HSM. The input properties were entered according to Table 7 and the tension cut-off was selected in order to promote the detachment after the uplift initiation. The drainage type was set to Undrained (B).

The footing was added to the model. It was placed in the centre of the surface and it was delimited by two vertices. The footing properties were defined according to Table 1. As a massless element it does not induce a change in soil stresses and strains, therefore, a vertical point load was added in the model together with a moment applied in the central point of the foundation.

An interface element was then entered under the plate in order to better model the soil-foundation interaction. It was modelled as a rigid element with no tensile strength and described by Hardening soil in drained conditions. The interface stiffness properties remained the same of the cohesive soil while the strength properties changed, considering a value of 35° for the angle of shearing resistance and a cohesion of 5 kPa. Due to the interface roughness, no lateral displacements were allowed to develop, limiting the increase of the shear force.

The Finite Element mesh was created with a medium discretization but the density mesh in correspondence of the structural or interface elements.

Model execution

As introduced before, a series of numerical analyses were performed starting from a very high value of the factor of safety, FS, defined as the ratio between the ultimate bearing capacity and the applied axial load (simulating all the possible gravitational loading

conditions such as the foundation weight). Then, in each analysis the factor of safety has been gradually decreased until a minimum value of 1,5, getting close to failure.

Before any numerical analyses, an analytical value of the soil ultimate bearing capacity, N_{max} , and of the ultimate moment capacity, M_u , were estimated. The first was calculated following the relationships in Section 3 about the Bearing Capacity of a homogeneous soil deposit, while the ultimate moment capacity was estimated in function of the applied vertical load (in function of the factor of safety) according to Equation 4.6 in section 4.2. There was no need to calculate the shear resistance due to the negligible value of the shear force developing at the soil-foundation interface.

The maximum tolerable vertical load, equal to 436 kN, was used to determine the vertical point load, N_{app} , to apply in the central point of the footing base in each analysis together with each specific value of the maximum moment (designated M in the numerical results) in correspondence to a certain value of the factor of safety. The Table 8 below collects all the input values of the static vertical load and moment for each case; the moment, M, represents the loading condition in the state of imminent failure.

N. Analysis	FS	Input N_{app} [kN]	Input M [kNm/m²]
1	20	21.8	10
2	10	44	19.5
3	5	87	35
4	3	145.5	48
5	2	218.5	54
6	1.5	291	48

Table 8 – Input parameters for the foundation loads.

As in the previous analysis of the linear elastic soil, the numerical simulations were performed in three different stages; the first and the second stages of each analysis were exactly the same performed in the numerical simulation about the linear elastic soil case. The last phase, in which the vertical load and the applied moment were combined together, followed the so called *dynamic* calculation in PLAXIS 2D. This type of calculation developed a gradual process of deformation of the points under the footing with accuracy, avoiding the instability in the response. Using this type of calculation, the vertical force, N_{app} , was kept as a static load while the moment, M, was switched to a dynamic action and applied step-by-step to the system. Therefore, a dynamic value at each time step was set equal to the input value of the load times the multiplier (chosen equal to 1). At the starting of the dynamic process the force was equal to zero; at the maximum time step the

input value of the action was equal to the maximum desired for the analysis. After a trial and error procedure the total dynamic time was set proportional to the value of the applied load, for instance a time equal to 100 seconds was chosen for an applied moment of 10 kNm/m². It is necessary to clarify that the dynamic time did not correspond to the real computational time, due to the number of sub-steps run in each time step, automatically defined by the software. Three different points were monitored for the final results, the central point and the two corners of the foundation base.

Numerical results

The moment-rotation response of the strip footing over a cohesive soil was indirectly obtained from the numerical results of the Phase 3, the last one calculated; the incremental values of the foundation rotation were computed as the difference between the incremental vertical displacements registered in the two corners of the foundation base, divided by the base width. The incremental moment for each i-step of Phase 3 was calculated multiplying the input value of the moment in the analysis, considered the highest possible for the specific factor of safety, by the ratio between the i-step and the last step:

$$M_i = \frac{\text{Step}_i}{\text{last Step}} M \quad (4.9)$$

Figure 4.9 shows the plot of the moment-rotation response of the footing for each factor of safety.

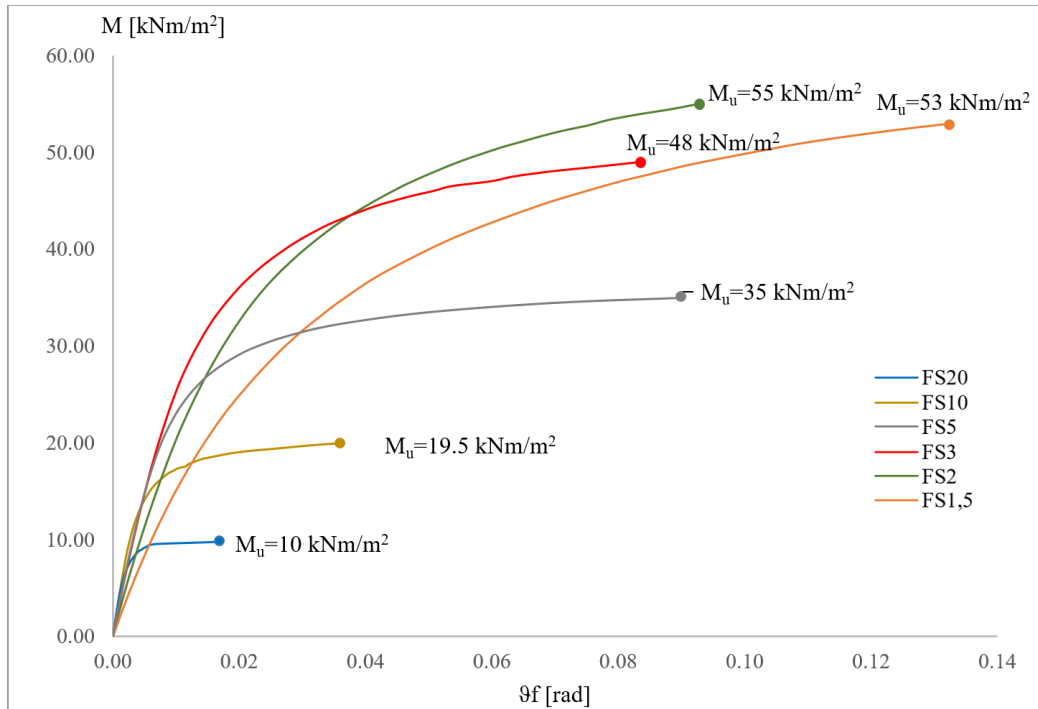


Figure 4.9- Moment-rotation response of a strip footing on a cohesive soil.

The plots have also been normalised by the ultimate moment capacity (Deng and Kutter, 2012) and uplift angle from Cremer (2001). The normalised behaviour (Figure 4.10) shows a clear trend which presents a new opportunity for generalising the behaviour compared to using stiffness reduction curves.

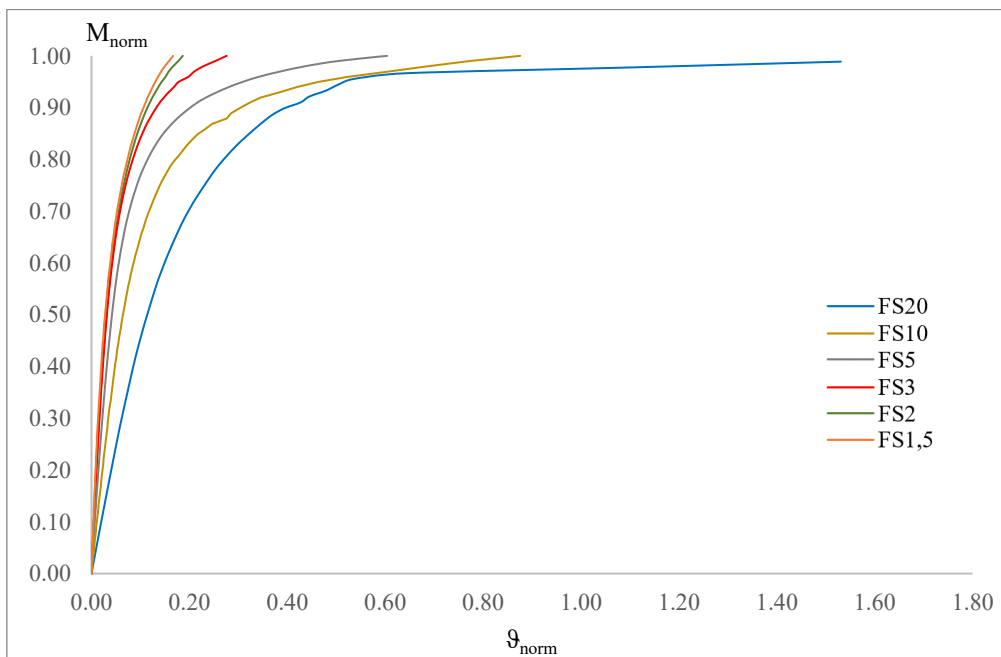


Figure 4.10- Moment-rotation response of a strip footing on a cohesive soil.

Another purpose of the analysis was the development of solutions for the rotational stiffness of the footing. The effective rotational stiffness of the $M-\vartheta_f$ response can be estimated as:

$$K_R = \frac{M}{\vartheta_f} \quad (4.10)$$

It depends on the shear stiffness of the soil, on the shear strength parameters - the undrained shear strength in this case - and on the geometry of the foundation, and, more than the other factor, it is a function of the ratio between the ultimate bearing capacity and the applied vertical load. In Figure 4.11 the stiffness vs. rotation curves, derived from the processing of the previous numerical results, are plotted, from the very small strains levels corresponding to values of the foundation rotation of the order of 10^{-4} .

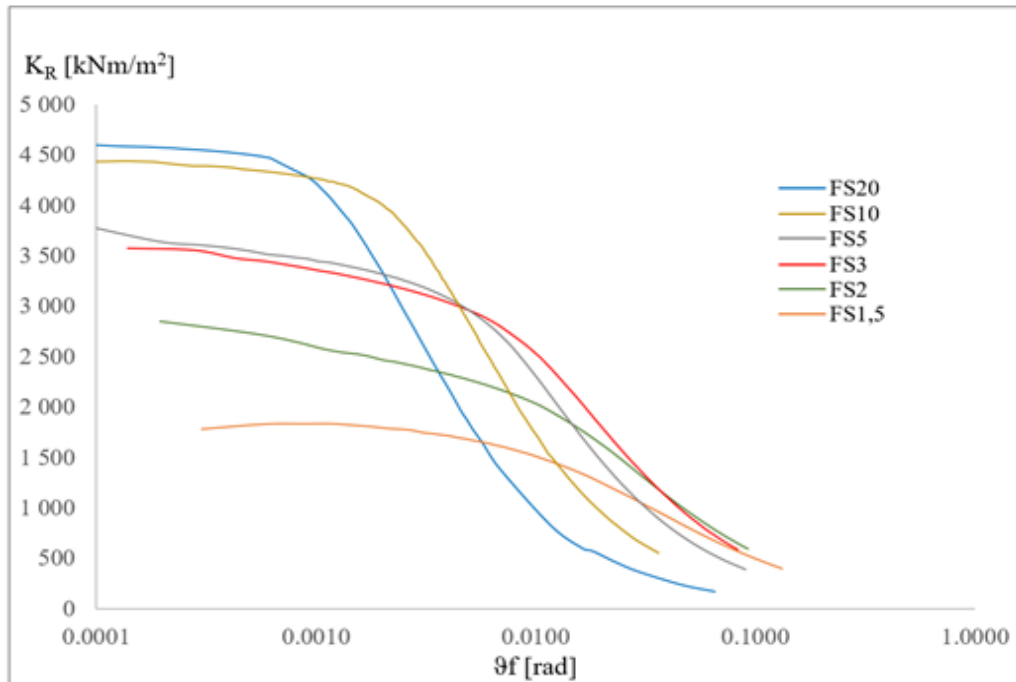


Figure 4.11- Rotational stiffness vs. rotation curves.

Finally, a normalisation of the numerical rotational stiffness and of the numerical angle of rotation is herein proposed for each factor of safety (Figure 4.12), finding no common solutions for all the different loading conditions. The normalised rotational stiffness was estimated dividing each value computed through the equation 4.10 by the very small strains stiffness, $K_{(0,FS)}$, numerically defined as the $M-\vartheta_f$ plot slope in correspondence of

the specific factor of safety. The normalisation through the theoretical elastic rotational stiffness expressed by the 4.3 was not suitable as the initial stiffness was influenced by the level of axial load and was only consistent for the highest factor of safety (FS=20), where the rotational response of the foundation could be comparable to the case of the linear elastic behaviour before the uplift initiation, meaning that the foundation was so lightly loaded that the material inelasticity and plastic deformations didn't take place at very low deformation levels.

The angle of rotation was normalised by the angle of uplift, $\vartheta_{\text{uplift}}$. The angle of uplift, defined as the angle of foundation rotation in correspondence to the uplift initiation, was calculated as the ratio between the analytically computed moment of uplift initiation, M_{uplift} , (see Equation 4.4) to the specific applied load and the numerical solution of the small strains rotational stiffness (K_0). It could not be dependent on the theoretical value of the elastic rotational stiffness because of its strong dependency on the loading condition, as it will be later explained.

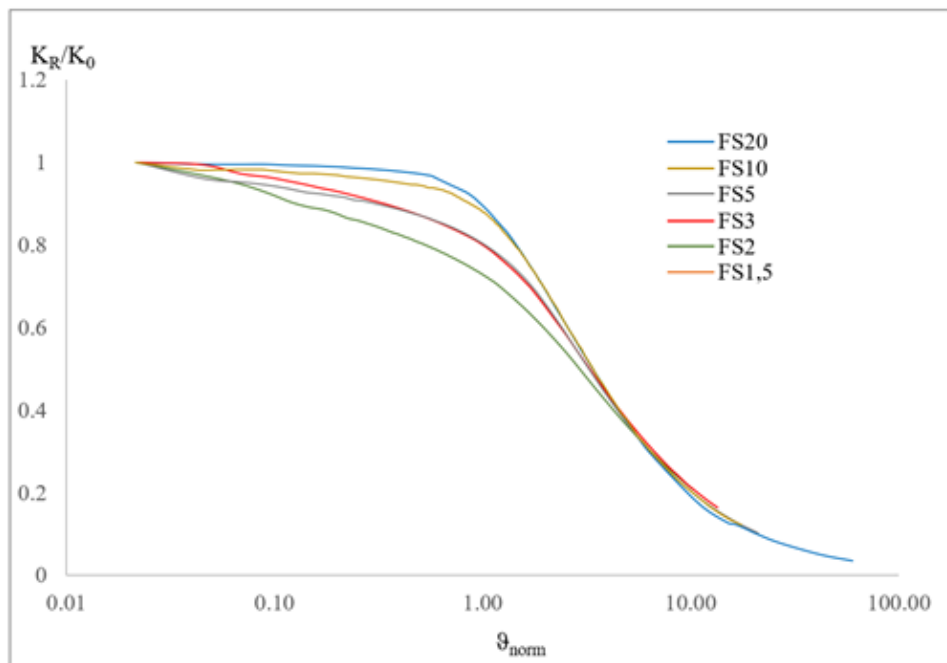


Figure 4.12- Normalised rotational stiffness vs. normalised angle of rotation.

Some resulting considerations are here presented.

The M - ϑ_f plots in Figure 4.9 show an evident dependency of the response on the $N_{\text{max}}/N_{\text{app}}$ ratio; due to the change in the level of soil plasticity and the point of uplift. Linear elasticity describes soil behaviour only at very small angles of rotation in correspondence

of high values of the factor of safety, meaning that closed-form expressions, available in literature, can be used to determine the elastic rotational stiffness of shallow foundations. Figure 4.13 proves what was just explained, by comparing the normalised rotational stiffness curve for a linear elastic material and the normalised rotational stiffness curve of a cohesive soil in a $N_{max}/N_{app}=20$ condition.

However, despite the highest small strain stiffness of the FS=20, the ultimate moment capacity of the foundation is the smallest one because of its dependency on the amount of the applied vertical load, N_{app} .

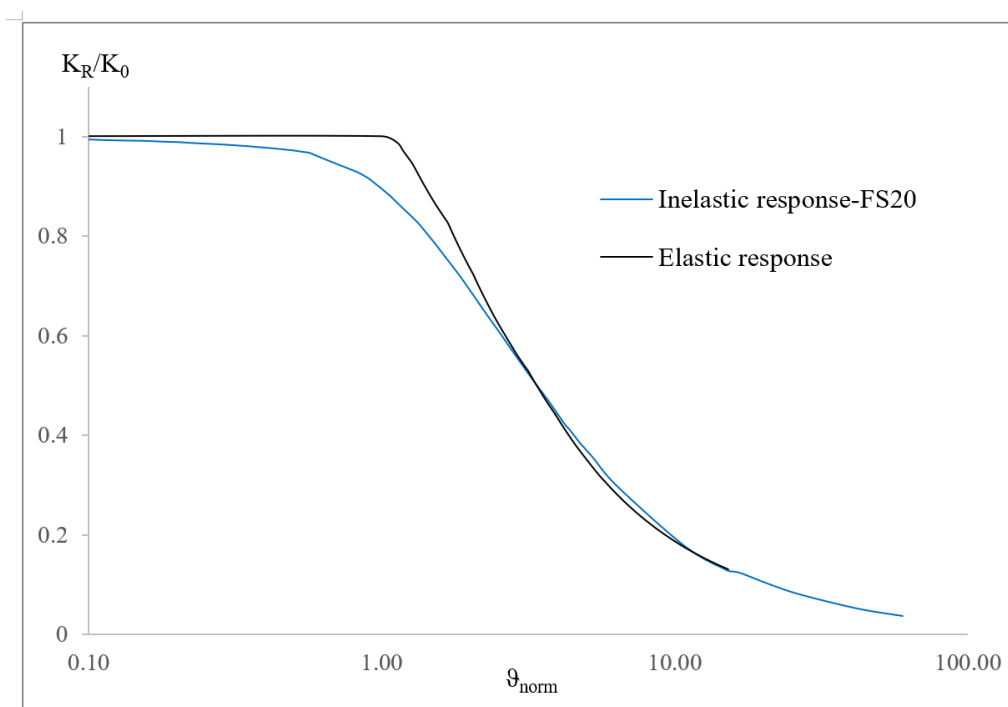


Figure 4.13- Inelastic response (FS=20) vs. Elastic response.

Moreover, Figure 4.9 shows that as the factor of safety decreases, the extent of uplifting reduces and the material inelasticity increases; looking carefully to the plots in Figure 4.9, the uplift initiation and the rotational stiffness degradation is more accentuated for the highest factors of safety while in the other cases it is more complex to discern the material inelasticity from the geometric one.

However, in all the cases it is evident that at large angles of rotation the development of non-linear deformations is strongly accentuated, even though the superposition of the plots means a common response for all the loading conditions. The lack of a single law to normalise all the different cases, especially the trends at small angle of rotation, is just

related to the different moments of uplift initiation that induce the strong degradation of the rotational stiffness.

All the models analysed in this section were qualitatively validated through a comparison with the proposed models in Gazetas et al. (2013), for the specific case of a strip footing, finding the numerical results of the current study in line with the ones in literature.

4.5 Moment-rotation response of a footing on a homogeneous inelastic soil: frictional material (clean sand)

The case here deals with the shallow foundation response on a purely frictional soil deposit, characterised by an angle of internal friction, ϕ' , and a non-tension interface.

As in the previous analysis different configurations were considered, depending on the N_{max}/N_{app} ratio, in order to highlight both the difference in the increasingly loaded foundation responses and the difference with the purely cohesive soil.

Model inputs

A shallow strip foundation overlying a 10 metres depth purely frictional soil layer was modelled in PLAXIS 2D. A zero value was assigned to the soil cohesion, making the failure behaviour depending only on the angle of shearing resistance, ϕ' , according to Mohr-Coulomb failure criterion. The footing was modelled as a rigid, massless plate with a rough interface characterised by a null tensile strength as in the previous analysis and all the features are summarised in Table 1. The water table was neglected.

The material model chosen in PLAXIS 2D to describe the soil behaviour was the Hardening Soil Model (HSM) and all the input parameters are collected in Table 9. The strength parameters were expressed in terms of the cohesion, c' , and the angle of shearing resistance, ϕ' , while the stiffness parameters in correspondence of a value of 100 kPa of the confining pressure, p_{ref} , in a triaxial test were defined in terms of the unloading and reloading stiffness modulus, E_{ur}^{ref} and the secant modulus at the 50% of the peak shear strength, E_{50}^{ref} set equal to the oedometer modulus. A value of 0,54 was set for the power of the hyperbolic stress-strain law and a failure ratio equal to 0,9 was entered.

Parameters	Clean Sand
Soil Model	Hardening
Drainage type	Drained
γ_u [kN/m ³] dry unit weight	17

γ [kN/m ³] saturated unit weight	19
e_0 [-] void ratio	0,8
φ' [°] angle of internal friction	34
ψ [°] angle of dilatancy	4,3
c [kPa] cohesion	0
K_0 [-] earth pressure coefficient	0,441
E_{ur}^{ref} [MPa] unload./reload. stiffness modulus	90
E_{50}^{ref} [MPa] secant stiffness in standard triaxial tests	30
ν [-] Poisson's ratio in unloading condition	0,2
p_{ref} [kPa] reference confining pressure	100
m [-] power for the stress level dependency of stiffness	0,54

Table 9 – Frictional soil input parameters in PLAXIS 2D.

Model construction

All the project properties, the geometry and size of the domain and the boundaries conditions are the same described in the previous analysis. The soil stratigraphy was defined by the *Boreholes* tool, creating a new material described by HSM. The input properties were entered according to Table 9 and the tension cut-off was selected in order to promote the detachment after the uplift initiation. The drainage type was set to 'drained' in order to model the typical drainage behaviour of a clean sand under a static monotonic load.

The footing was placed as a plate in the centre of the surface and it was delimited by two vertices. The footing properties were defined according to Table 1. It was modelled as a massless element; thus, a vertical point load was added in the model together with a moment applied in the central point of the foundation.

An interface element was then entered under the plate in order to better model the soil-foundation interaction. It was modelled as a rigid element with no tensile strength and described by HSM in drained conditions. The interface input parameters were set as the same of the adjacent soil with a frictional behaviour. Due to the interface roughness, no lateral displacements were allowed to develop, limiting the arising of the shear force.

The Finite Element mesh was created with a medium density but taking care to first intensify the density mesh in correspondence of the structural or interface elements.

Model execution

As in the previous analyses, a set of numerical simulations were performed starting from a very high value of the factor of safety, FS, and gradually decreasing it till the minimum value of 1,5, getting close to the failure.

Before any numerical analyses, the analytical value of the soil ultimate bearing capacity, N_{max} , and of the ultimate moment capacity, M_u , were estimated. The first one was calculated following the relationships in Section 3 for the bearing capacity of a homogeneous soil deposit, while the ultimate moment capacity was estimated in function of the applied vertical load (in function of the factor of safety) (see Equation 4.7).

The shear resistance was not estimated due to the negligible value of the shear force developing at the soil-foundation interface.

The maximum tolerable vertical load, equal to 265 kN, was used to determine the vertical point load, N_{app} , to apply in the central point of the footing base in each analysis together with the specific value of the maximum moment, M , in correspondence of its own factor of safety. The Table 10 below collects all the input values of the static vertical load and moment for each case; the moment, M , represents the loading condition in the state of incipient failure.

N. Analysis	FS	Input N_{app} [kN]	Input M [kNm/m ²]
1	20	13	6
2	10	27	11
3	5	53	18
4	3	88	24,5
5	2	133	29
6	1,5	177	28,5

Table 10 - Input parameters for the foundation loads.

The numerical simulations were performed in three different stages, correspondent to the stages run in the previous analysis in section 4.3, with the last phase, in which the vertical load and the applied moment were combined together, performed through a so called *dynamic* calculation in PLAXIS 2D. Using this type of calculation, the vertical force, N_{app} , was kept as a static load while the moment, M , was switched in a dynamic action and applied step-by-step to the system. Therefore, a dynamic value at each time step, equal to the input value of the load times the multiplier (chosen equal to 1) was defined. Dynamic time started with the force equal to zero, while at the maximum time step the input value of the action was equal to the maximum desired for the analysis. After a trial and error procedure the total dynamic time was set proportional to the value of the applied load, for instance a time equal to 60 seconds was chosen for an applied moment of 6 kNm/m².

Each time-step was characterised by a certain number of sub steps, automatically set by the software, making the computational dynamic time different from the real one.

Three different points were monitored for the final results, the central point and the two corners of the foundation base.

Numerical results

The moment-rotation response of the strip footing over a purely frictional soil was indirectly obtained from the numerical results of the Phase 3, the last one calculated; the incremental values of the foundation rotation and the incremental moment for each i-step of Phase 3 were calculated following the same procedure described in the previous cases of study.

Figure 4.14 shows the plot of the moment-rotation response of the footing for each factor of safety.

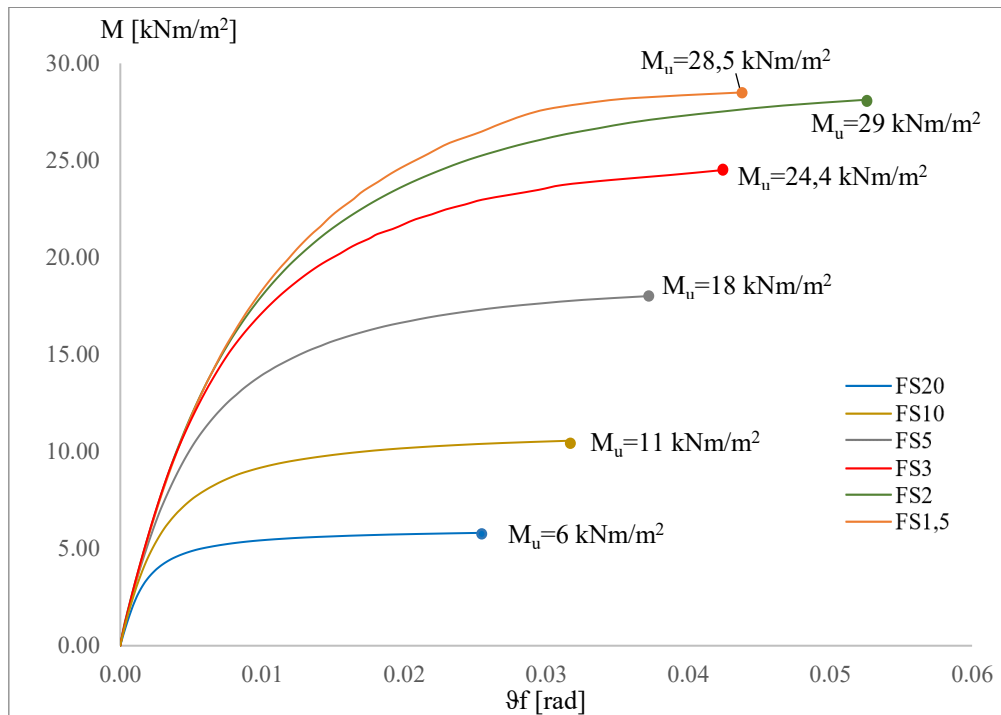


Figure 4.14- Moment-rotation response of a strip footing on a purely frictional soil.

Another purpose of the analysis was the development of solutions for the rotational stiffness of the footing. The effective rotational stiffness of the $M-\vartheta_f$ response can be estimated following Equation 4.10. The shear stiffness of the soil, the shear strength parameters, the angle of shearing resistance in this case, and the geometry of the foundation affect the results. However, the main factor influencing the rotational stiffness of the foundation is the ratio between the ultimate bearing capacity and the applied

vertical load. In Figure 4.15 the stiffness vs. rotation curves, derived from the processing of the previous numerical results, are plotted, since very small strains levels corresponding to values of the foundation rotation of the order of 10^{-4} rad.

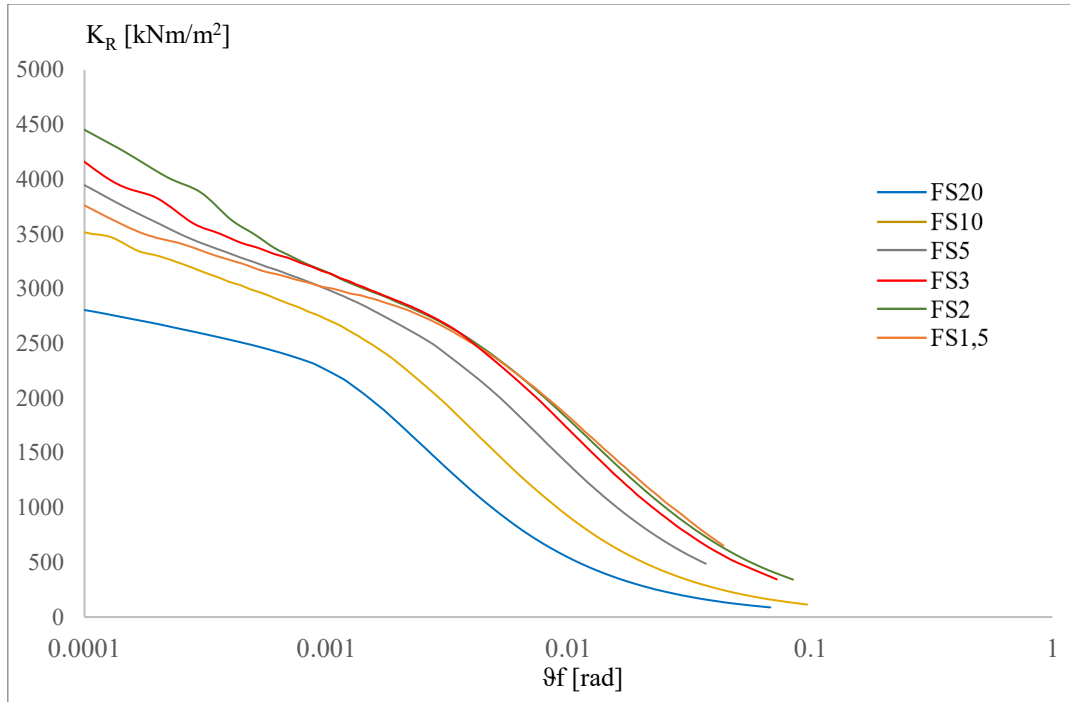


Figure 4.15- Rotational stiffness vs. rotation curves for homogenous sandy soil.

Finally, the numerical rotational stiffness and the numerical angle of rotation were normalised as herein proposed (Figure 4.16) in correspondence of each factor of safety, finding no common solutions for all the different loading conditions. But it can be observed that the normalised stiffness is lower for the heavily loaded footings due to the greater soil non-linearity.

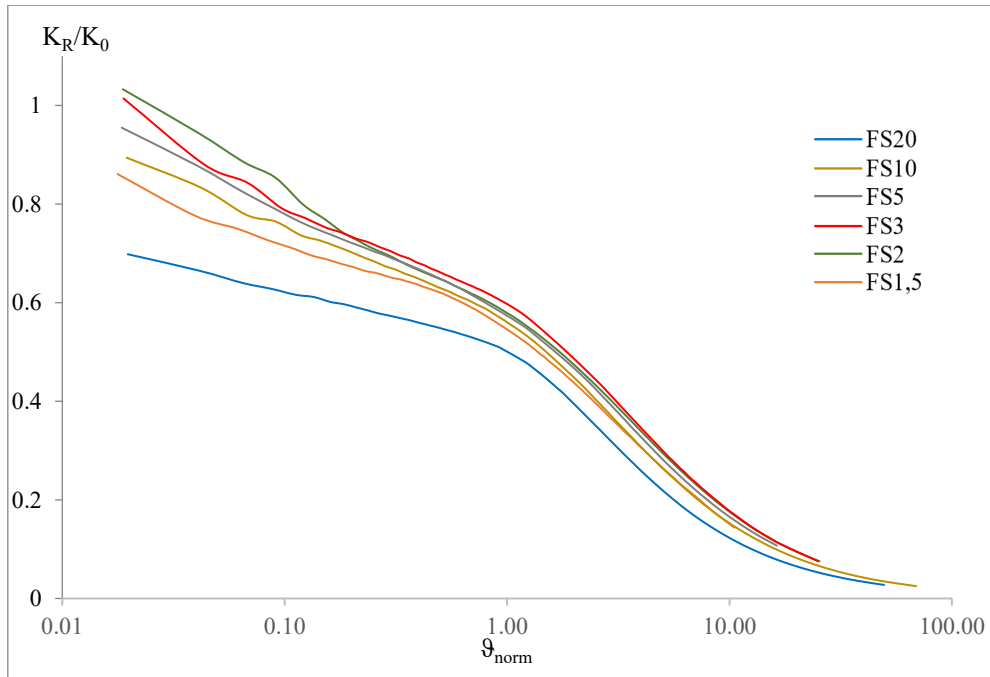


Figure 4.16- Normalised rotational stiffness vs. normalised angle of rotation.

The normalised rotational stiffness was estimated dividing each value computed through the Equation 4.10 by the very small strains stiffness, $K_{(0,FS)}$, numerically defined as the $M-\vartheta_f$ plot slope in correspondence of the specific factor of safety. The theoretical elastic rotational stiffness expressed by the 4.3 was not possible to use to normalise the numerical results (see Figure 4.17) because of the strong non-linearity in the response since very small values of the angle of rotation; in fact, the initial rotational stiffness is a function of the shear stiffness expressed by the shear modulus, G , that does not remain constant but changes with the level of load, as observed in the numerical results. Therefore, it is hard to refer to an analytical value of the elastic rotational stiffness due to its strong variability from lightly to heavily loaded foundations. The plot in Figure 4.17 shows that the behaviour is completely different at very small strains followed by a strong approaching among the trends, probably meaning that after a certain point the loading conditions dependency reduces more and more.

Furthermore, the angle of rotation was normalised by the angle of elastic uplift initiation, $\vartheta_{\text{uplift}}$, defined as the uplift moment divided by the elastic stiffness. It was calculated as the ratio between the analytically computed moment of uplift initiation, M_{uplift} , (see expression 4.4) for the specific applied load and the numerical solution of the small strains rotational stiffness ($K_{(0,FS)}$). It could not be dependent on the theoretical value of the elastic

rotational stiffness, computed through Equation 4.3 because of its strong dependency on the loading condition.

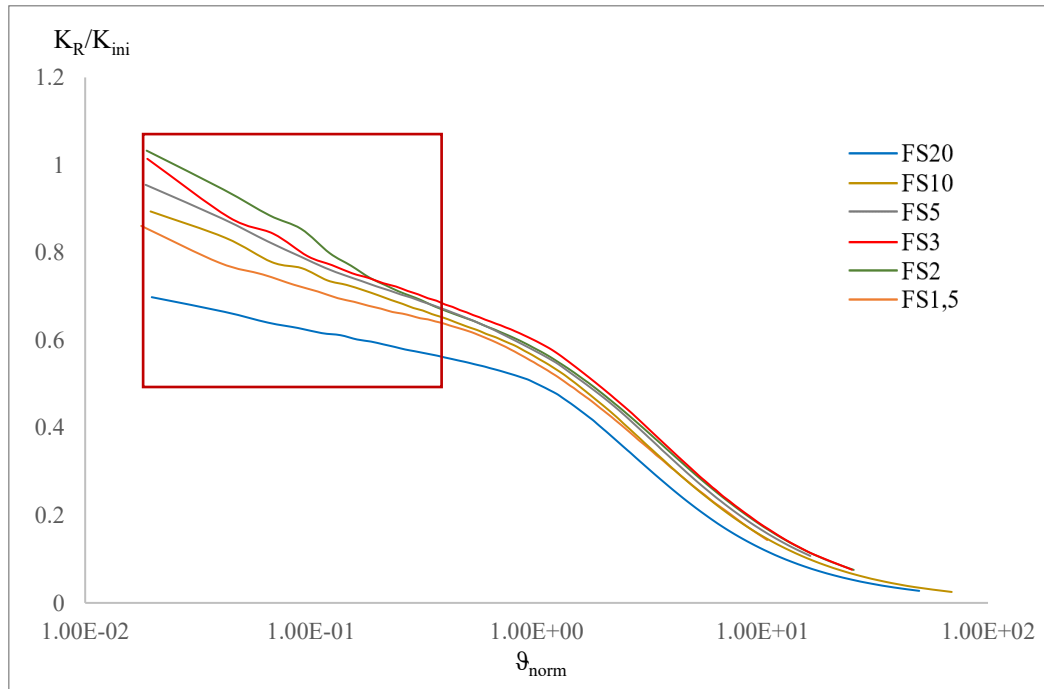


Figure 4.17- Normalised rotational stiffness by the analytical elastic stiffness vs. normalised angle of rotation.

Some resultant considerations are here exposed.

The main and most evident difference between the previous case and the current one of a purely frictional soil is expressed by the opposite initial stiffness response in correspondence of each factor of safety; the decrease of the factor of safety and the increment in loading leads to an increase in the rotational stiffness of a sandy soil, that may be observed both in the plots of Figure 4.11 where the $M-\vartheta_f$ plot slope at low values of the angle of rotation is less pronounced in correspondence of the $FS=20$ than in $FS=2$ and in Figure 4.12 where the stiffness degradation curve at $FS=20$ starts from an initial value almost half of the initial stiffness recorded at $FS=2$.

In Figure 4.18 the sand model and the clay model are compared. Differently from the cohesive soil model, the material non-linearity is in this case much more accentuated from the early small applied loads, making it much more difficult to identify the uplift initiation; in fact, there is no chance to observe any initial plateau in the rotational stiffness curves and in their normalisation (see Figure 4.18). It means that the normalisation of the angle of rotation could be affected by a percentage of error related to the use of the analytical value of the moment of uplift initiation, M_{uplift} , due to the continuous plasticity of the

model combined with the material type (more frictional or more cohesive) and thus, the difficulty in the attribution of the correct value of the parameter ζ in Equation 4.4.

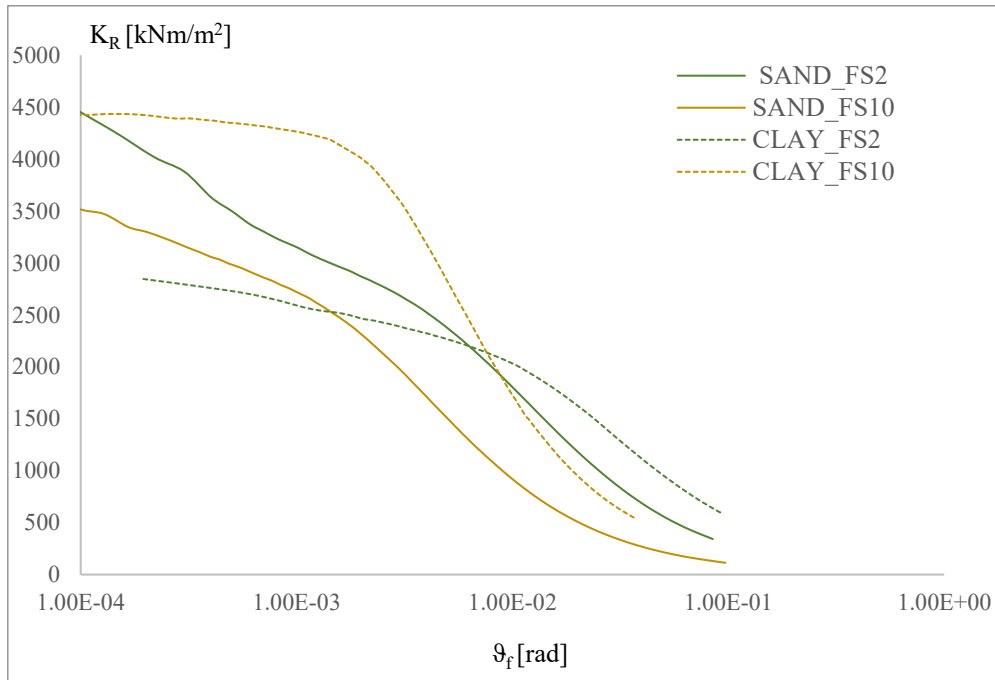


Figure 4.18- Comparison between clay and sand rotational stiffness degradation.

Finally, in the current case it is easy to notice for each factor of safety the strong decay of the rotational stiffness much more pronounced at low values of the factor of safety resulting also in a separation of the curves since the beginning, and in correspondence of large values of the angles of rotation, meaning the development of plastic deformations. The second half of the plot in Figure 4.17 is characterised by a superposition of the curves, suggesting that after a certain value of the foundation rotation the response is not affected by the factor of safety.

4.6 Moment-rotation response of a shallow foundation on layered deposit

The last performed numerical analysis dealt with a shallow foundation on a two-layered deposit, with a surface crust layer and a supposed liquefied layer below.

Different configurations have been investigated, based on a variation of the upper layer soil strength and stiffness properties and on the level of liquefaction assumed to be achieved in the lower layer under seismic actions.

The aim is to define the moment-rotation behaviour of the foundation in a deposit in which a part of the soil has been subjected to liquefaction, losing part of the shear strength and shear stiffness, and to find useful solutions for the rotational stiffness in a condition where the material non-linearity is further accentuated.

As explained in previous chapters, the phenomena of liquefaction lead to a temporary static bearing capacity degradation for the supporting soil underlying shallow foundations and potentially a soil shear failure during the seismic excitation resulting in very large settlements and tilting. For the simulation of this particular condition, since the modelling was done statically, the lower layer material was set to an approximated reduced strength and stiffness by assuming a level of pore pressure build up. Therefore, the same procedure described and detailed in Section 3.4 has been followed to calibrate the input material parameters for the lower liquefiable layer.

Two main studies were carried out distinguished by the material type, respectively a stiff clay and/or a stiff clean sand, in the upper layer; for each of the two cases two different levels of liquefaction were analysed, a partial and a total liquefaction of the lower layer; finally, a parametric study was carried out based on the crust thickness. The flow chart in Figure 4.19 summarises the procedure.

The condition of partially or fully liquefied lower layer is expressed through the ratio between the shear waves velocity of the upper stiffer layer ($V_{s,1}$) and the shear waves velocity of the lower one ($V_{s,liq}$) together with the excess pore pressure build-up ratio, U , in the specific case of stiff sand overlying the liquefied layer. In the second macro condition where the deposit is characterised by an upper cohesive soil layer and a lower liquefied layer, the reduced stiffness and strength parameters are the ones used to model the lower weaker layer in the aforementioned model.

This choice is in line with what was explained and justified in Section 3.4; the partial liquefaction was modelled by a $V_{s,1}/V_{s,liq}=4$ and a $U=0,8$ while the total liquefaction was modelled with $V_{s,1}/V_{s,liq}=10$ and a $U=0,95$.

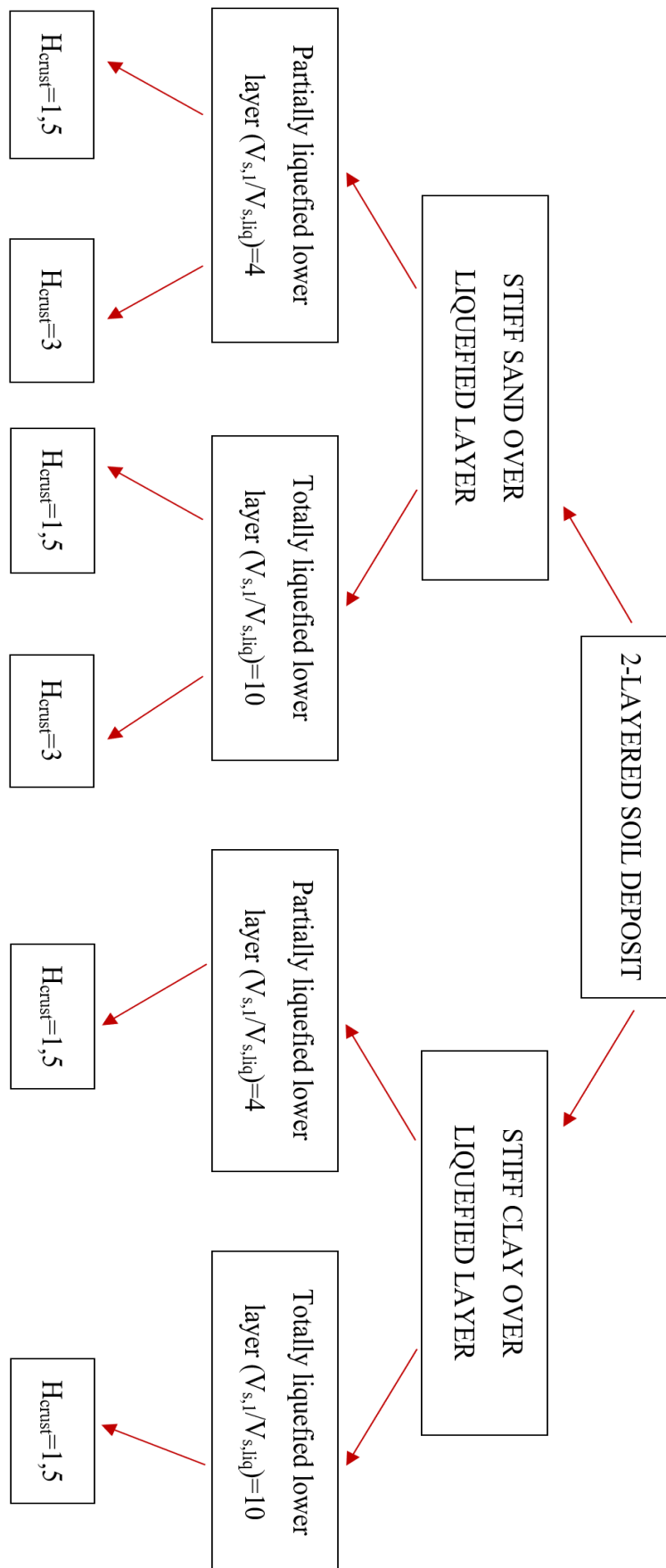


Figure 4.19- Flow chart of the procedure followed in the 2-layered deposit.

Model inputs

The input properties of the shallow foundation were the same of the other numerical analyses previously exposed and summarised in Table 1. The materials input parameters are collected in Table 11, referring only to the partially or totally liquefied layer materials because the stiff clayey crust and the stiff sandy crust were modelled through the material parameters used respectively for the analyses in Section 4.4 and 4.5, and summarised in Table 7 and Table 9.

Parameters	Partial liquefaction	Total Liquefaction
Soil Model	Hardening	Hardening
Drainage type	Drained	Drained
γ_u [kN/m ³] dry unit weight	17	17
γ [kN/m ³] saturated unit weight	19	19
e_0 [-] void ratio	0,8	0,8
ϕ'_{liq} [°] angle of internal friction	8	2
ψ [°] angle of dilatancy	0	0
G_{liq} [MPa] Reduced shear modulus	5,9	0,95
ν [-] Poisson's ratio in unloading condition	0,2	0,2
p_{ref} [kPa] reference confining pressure	100	100
m [-] power for the stress level dependency of stiff.	0,54	0,54

Table 11- Input material parameters of the lower liquefied layer.

The reduced angle of shearing resistance was calculated as a function of the actual angle of internal friction in pre-liquefaction condition (corresponding to the angle of internal friction in the upper non-liquefiable layer), and of the excess pore pressure ratio, using the Equation 3.18 in section 3.4.

The stiffness degradation was simulated through a reduction in the shear wave velocity and thus, proportionally to G_{max} , the original maximum value of the shear modulus equal to 233 m/s ($V_{s,ini}=V_{s,1}$), according to the characteristic stiffness value of the crust and it was reduced first of 4 times and then of 10 times to represent respectively the partial and the total liquefaction in the lower layer. The reduced shear modulus was calculated following the Equations 3.19 and 3.20.

Moreover, the liquefied layer was characterised by a null angle of dilatancy in order to represent the purely contractive behaviour of the soil.

Model construction

All the project properties, the geometry and size of the domain and the boundaries conditions are the same described in the previous analysis. The soil stratigraphy was defined by the *Boreholes* tool, creating two different layers and assigning each one the thickness value and the material parameters in the Hardening Soil Model (HSM).

The footing was placed as a plate in the centre of the surface and it was delimited by two vertices. The footing properties were defined according to Table 1. It was modelled as a massless element; thus, a vertical point load was added in the model together with a moment applied in the central point of the foundation.

An interface element was then introduced under the plate in order to better model the soil-foundation interaction. It was modelled as a rigid element with no tensile strength and described by the HSM in drained conditions. The interface input parameters were set as the same of the adjacent soil in the case of the upper sandy layer while in the other case of cohesive soil crust the interface was modelled according to Section 4.4.

The interface element was added between the two layers, too, in order to better model the material interaction during the numerical simulations. It was modelled imposing the material properties of the upper layer.

The Finite Element mesh was created with a medium density but in correspondence of the material interfaces it was increased 4 times compared with the model mesh because of the high differences in stiffness and strength of the materials that lead to stresses and strains gradients, which implies higher stress-strain distribution.

Model execution

The numerical analyses were performed in accordance with the model variation, the level of liquefaction set in the lower layer and the crust thickness. For each case considered in the parametric study, different loading conditions have been investigated, starting from a very high value of the factor of safety, FS, and gradually decreasing it until the minimum value of 2.

A previous analytical computation was carried out to estimate the two-layered deposit ultimate bearing capacity, N_{max} , and the ultimate moment capacity, M_u . The bearing capacity was computed using Meyerhof and Hanna (1973) solution expressed by Equation 3.14 in presence of the sandy crust and Equation 3.9 in presence of clayey crust. The moment capacity was originally calculated using the equation based on the factor of safety (Equation 4.7), however, the numerical results were inconsistent with this theoretical value. Instead the moment capacity, M_u , was also computed assuming the

bearing capacity for a homogeneous soil, which produced much more consistent results. This is in-line with the equation by Deng et al. (2014) that uses the critical area (Equation 4.5), and conceptually can be explained in Figure 4.20, where the stress bulb at ultimate moment stays within the crust layer and therefore develops the same behaviour as the homogeneous soil. This choice was made after an analytical procedure aimed to compare the results from a model of a shallow foundation on a layered deposit and a model of a shallow foundation on a homogeneous deposit. They developed approximatively the same level of ultimate moment and, therefore, the $\frac{A_c}{A}$ ratio was approximatively the same in the condition of eminent failure produced by M_u .

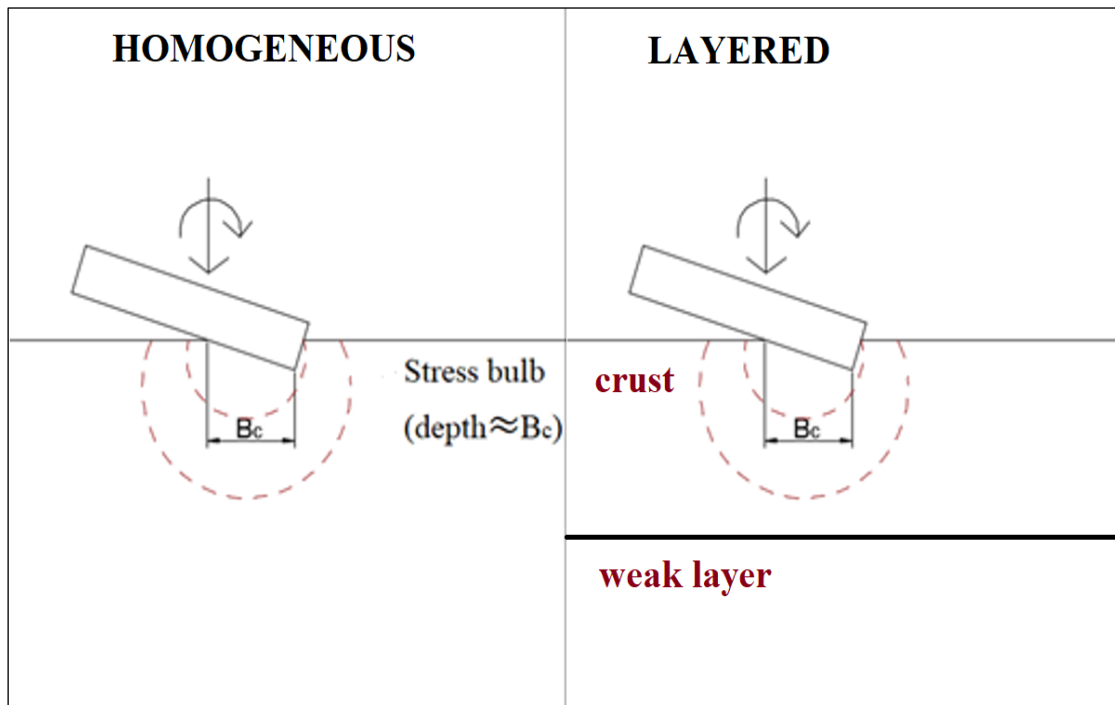


Figure 4.20-Comparison between homogeneous deposit and layered deposit.

The maximum tolerable vertical load, N_{max} , different for each numerical model investigated, was used to determine the vertical point load, N_{app} , to apply in the central point of the footing base in each analysis, together with each specific value of the maximum moment, M , in correspondence of its own applied vertical load.

The Tables 12÷17 below collect all the input values of the applied vertical loads and moments for each case.

1. Stiff sand over partially liquefied layer with $H_{crust}=1,5$ m.

Ultimate Bearing capacity of the 2-layered deposit: $N_{max}= 82$ kN.

N. analysis	Input N_{app}	Input M
1	8,2	3,6
2	16,4	7,5
3	27,3	12
4	41	15,5

Table 12- Input parameters for the foundation loads in Stiff sand over partially liquefied layer deposit ($H_{crust}=1,5$ m).

2. Stiff sand over partially liquefied layer with $H_{crust}=3$ m.

Ultimate Bearing capacity of the 2-layered deposit: $N_{max}= 220$ kN.

N. analysis	Input N_{app}	Input M
1	22	9,2
2	44	17
3	73,3	23
4	110	30

Table 13- Input parameters for the foundation loads in Stiff sand over partially liquefied layer deposit ($H_{crust}=3$ m).

3. Stiff sand over totally liquefied layer with $H_{crust}=1,5$ m.

Ultimate Bearing capacity of the 2-layered deposit: $N_{max}= 53$ kN.

N. analysis	Input N_{app}	Input M
1	5,2	2,5
2	10,6	5
3	17,3	8
4	26	11

Table 14- Input parameters for the foundation loads in Stiff sand over totally liquefied layer deposit ($H_{crust}=1,5$ m).

4. Stiff sand over totally liquefied layer with $H_{crust}=3$ m.

Ultimate Bearing capacity of the 2-layered deposit: $N_{max}= 160$ kN.

N. analysis	Input N_{app}	Input M
1	16	7
2	32	13,5
3	53,3	20,5
4	80	25

Table 15- Input parameters for the foundation loads in Stiff sand over totally liquefied layer deposit ($H_{crust}=3$ m).

5. Stiff clay over partially liquefied layer with $H_{crust}=1,5$ m.

Ultimate Bearing capacity of the 2-layered deposit: $N_{max}= 200$ kN.

N. analysis	Input N_{app}	Input M
1	20	9,5
2	40	18
3	66,7	28
4	100	39

Table 16-Input parameters for the foundation loads in stiff clay over partially liq. layer deposit ($H_{crust}=1,5$ m).

6. Stiff clay over totally liquefied layer with $H_{crust}=1,5$ m.

Ultimate Bearing capacity of the 2-layered deposit: $N_{max}= 110$ kN.

N. analysis	Input N_{app}	Input M
1	11	5,5
2	22	10,5
3	36,7	17
4	55	26

Table 17- Input parameters for the foundation loads in stiff clay over totally liq. layer deposit ($H_{crust}=1,5$ m).

The numerical simulations were performed in three different stages, corresponding to the stages run in the previous analyses, with the last phase, in which the vertical load and the applied moment were combined together. The vertical force, N_{app} , was kept as a static load while the moment, M , was switched in a dynamic action and applied step-by-step to the system.

Three different points were monitored for the final results, the central point and the two corners of the foundation base.

Numerical results

The moment-rotation responses of the shallow strip foundation over two-layered soil deposits were indirectly obtained from the numerical results of each Phase 3, the last one calculated (Figures 4.21, 4.24, 4.28, 4.31, 4.34, 4.37); the incremental values of the foundation rotation and the incremental moment for each i-step of Phase 3 were calculated following the same procedure described in the previous cases of study.

The effective rotational stiffness curve of the $M-\vartheta_f$ responses are herein presented (Figures 4.22, 4.26, 4.29, 4.32, 4.35, 4.38). They have been derived from the processing of the $M-\vartheta_f$ numerical results, since very small strains levels corresponding to values of the foundation rotation of the order of 10^{-4} . Finally, Figures 4.23, 4.27, 4.30, 4.33, 4.36, 4.39 show the normalisation of the numerical rotational stiffness and of the numerical angle of rotation for each factor of safety in each specific case of investigation, finding no common solution for all the different loading conditions. The normalisation has been carried out following the same procedure described in Section 4.6. The normalisation through the theoretical elastic rotational stiffness expressed by the 4.3 was not possible to apply because of the strong non-linearity in the response since very low values of the angle of rotation, both for the cases of sandy layered deposits and for the cases of the clayey crust over the liquefied layer. The angle of rotation was normalised by the angle of uplift, $\vartheta_{\text{uplift}}$.

1. Stiff sand over partially liquefied layer with $H_{\text{crust}}=1,5$ m.

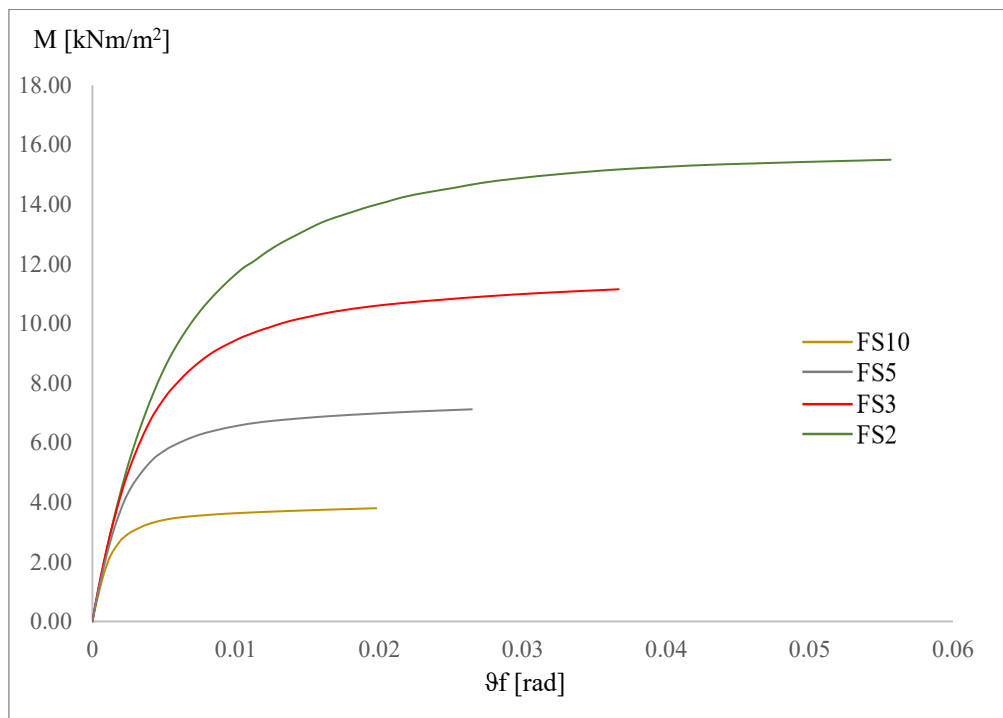


Figure 4.21 - Moment-rotation response of a strip footing on a 2-layered deposit.

The plot above (Figure 4.21) shows the moment-rotation behaviour of the foundation until the ultimate moment condition is reached. In correspondence of each applied vertical load, chosen as a part of the ultimate bearing capacity in this specific layered deposit ($N_u=82$ kN), the ultimate moment capacity achieved is almost the same achieved in the homogeneous sandy soil, associated to the same applied load but a lower factor of safety. It means that for layered soil deposits it is possible to estimate the ultimate moment capacity using the critical area-based formulation expressed by Equation 4.5. This is because the degradation of the lower layer reduces bearing capacity but doesn't change the critical area and also doesn't change the moment capacity. A simpler alternative would be to compute the moment capacity using the factor of safety value for the homogenous case, provided that the crust layer is sufficiently thick that the stress bulb at failure would be within the crust. For example, considering a degraded factor of safety of 2, and a degraded ultimate bearing capacity, N_u , the applied vertical load, N_{app} , is equal to 41 kN, meaning that the use of Equation 4.7 based on the factor of safety associated to the layered deposit leads to a value of the ultimate moment capacity equal to 10,3 kNm while the use of the factor of safety associated to the homogeneous sandy soil (with the same properties of the crust in the layered deposit), 3 times higher than $FS=2$, leads to a

value of the ultimate moment capacity equal to 17 kNm, very close to the numerical solution shown in Figure 4.21.

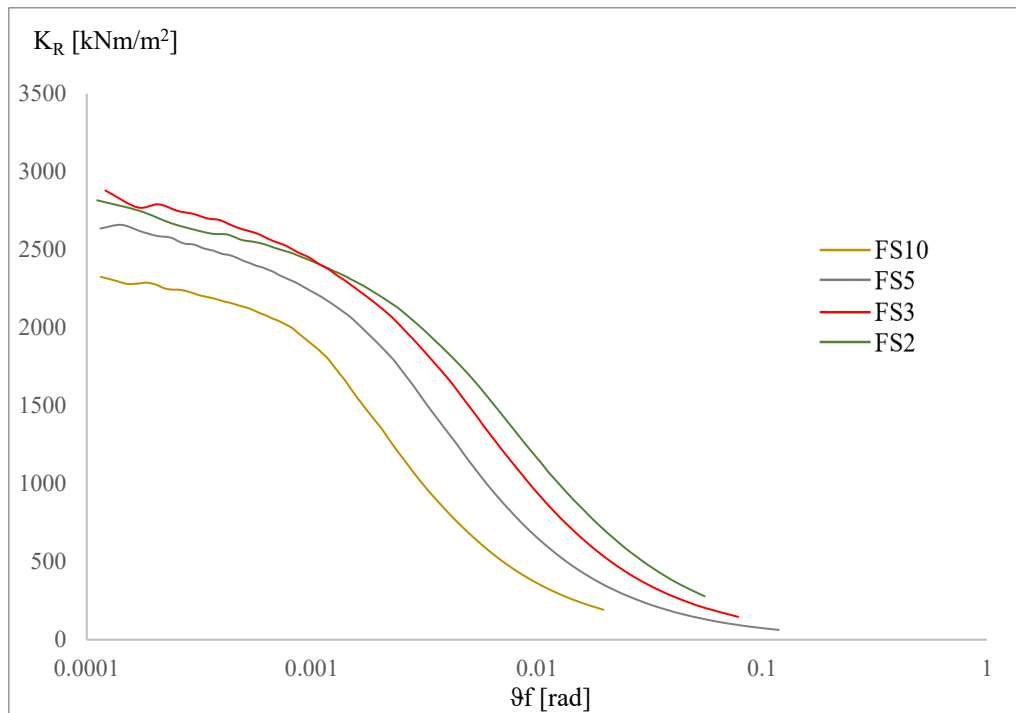


Figure 4.22- Rotational stiffness vs. rotation curves.

As in the case of homogeneous sandy soil, the $M-\theta_f$ curves initial slope is less accentuated in correspondence of high factors of safety and then increasing with the increase in loading, shown also in the plot in Figure 4.22 where the highest initial elastic stiffness is associated to the lowest factor of safety.

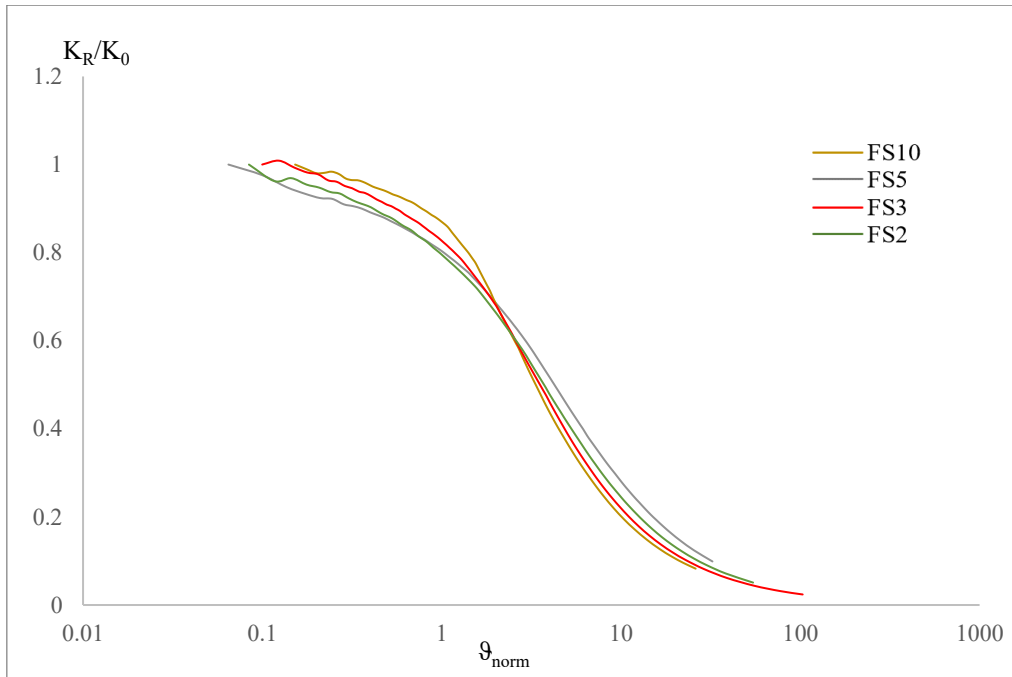


Figure 4.23- Normalised rotational stiffness vs. normalised angle of rotation.

The superposition of the normalised stiffness vs. normalised rotation curves looks pretty good in Figure 4.23, even though the use of the same formulations used in case of homogeneous sandy soil.

2. Stiff sand over partially liquefied layer with $H_{crust}=3$ m.

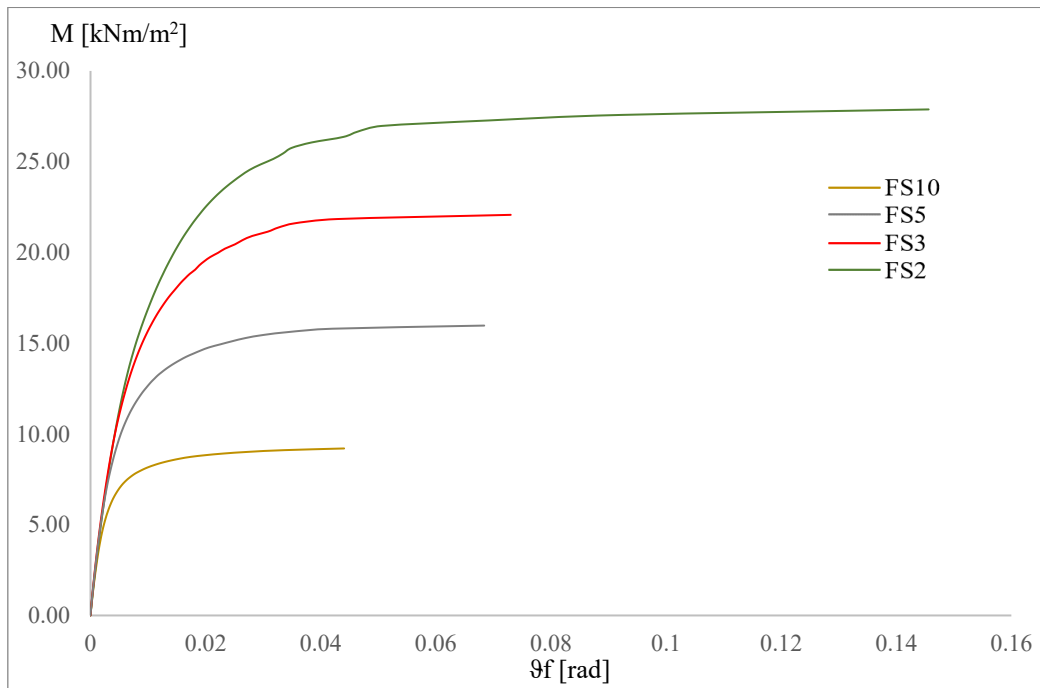


Figure 4.24 - Moment-rotation response of a strip footing on a 2-layered deposit.

The ultimate moment capacity achieved, for the different loading conditions, is higher when the crust thickness was doubled; in accordance with the ultimate bearing capacity problems shown in section 3, it means that the stress bulb at overturning moment is almost totally inside the upper layer and the ultimate moment conditions achieved are almost the same achieved in the homogeneous sandy soil deposit. In contrast the foundation rotations measured in the current case are higher than the ones in the homogeneous sandy deposit (Figure 4.25).

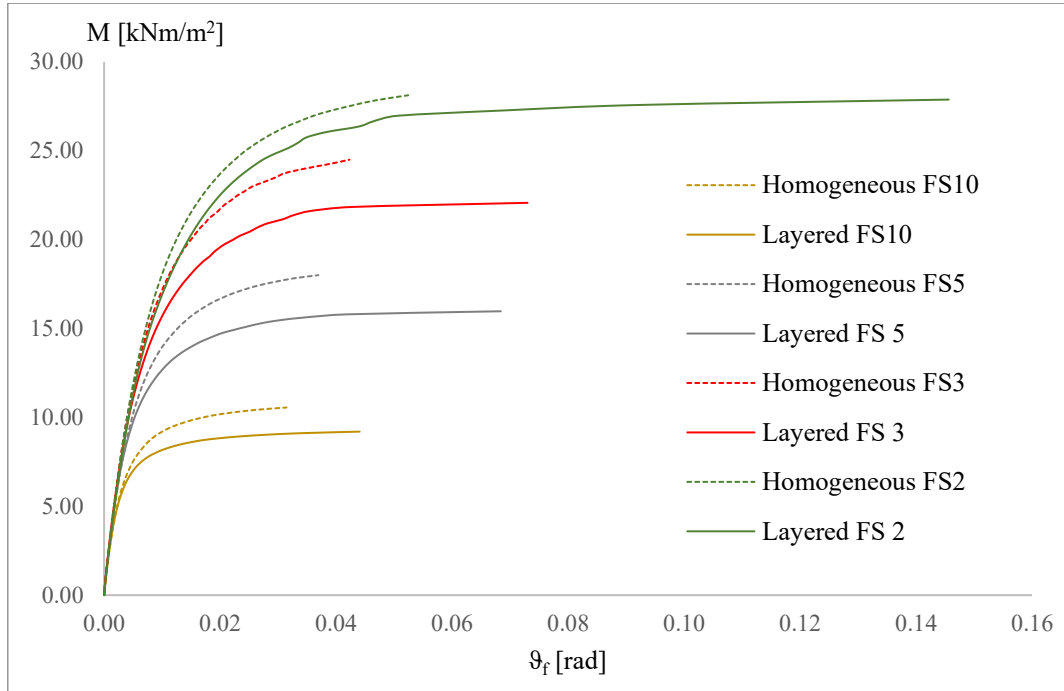


Figure 4.25 – Comparison between $M-\vartheta_f$ in the homogeneous sand deposit with $M-\vartheta_f$ in layered deposit with $H_{crust}=3$ m and $V_{s1}/V_{sliq}=4$.

The stiffness degradation curves in Figure 4.26 show the usual s-shape of the other cases but in this case the curve corresponding to FS=2 starts from a lower initial value compare to the others. It could depend on a computational error in the numerical analysis related to the dynamic time chosen or the number of sub-steps, because the other initial values follow the same usual order seen in all the other cases of sandy soil. It could also be related to the reduction in stiffness with depth; the size of the stress bulb decreases as uplift starts because the foundation contact area decreases, getting a possible reduction in the initial stiffness.

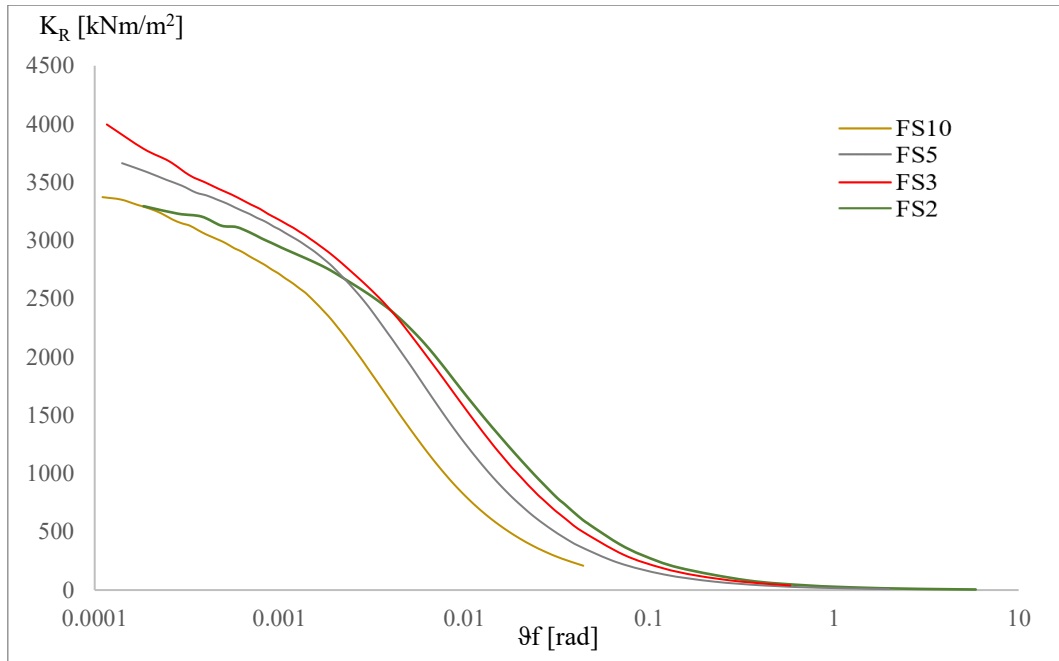


Figure 4.26- Rotational stiffness vs. rotation curves.

The normalised stiffness-rotation curves in Figure 4.27 are almost perfectly superimposed, from the beginning at very low values of the normalised rotation to the end. It suggests that the procedure used to normalise the results, based on the numerical value of the initial rotational stiffness, results right.

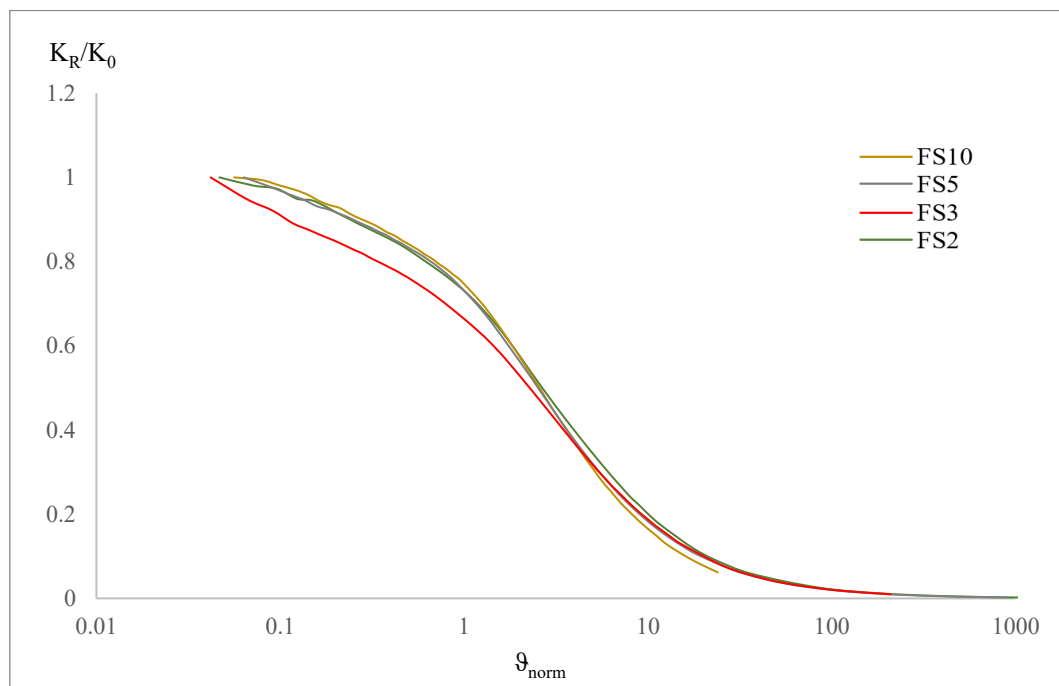


Figure 4.27- Normalised rotational stiffness vs. normalised angle of rotation.

3. Stiff sand over totally liquefied layer with $H_{crust}=1,5$ m.

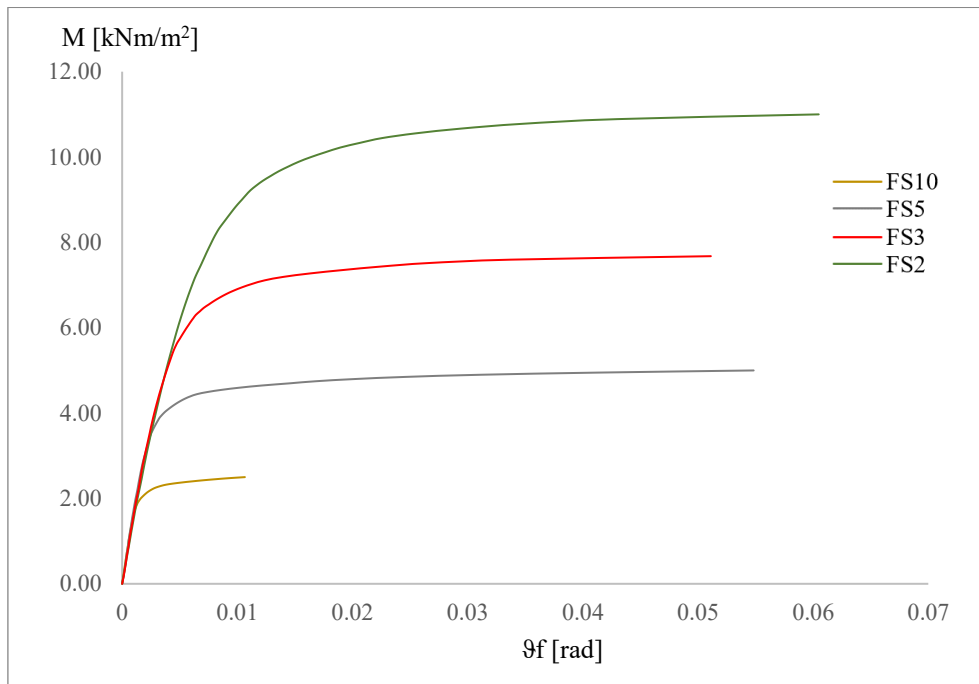


Figure 4.28 - Moment-rotation response of a strip footing on a 2-layered deposit.

The total liquefaction in the lower sandy layer leads to a significant decrease of the ultimate moment capacity of the soil-foundation system, as shown in Figure 4.28 which is accentuated compared to the following case because of the low value of the upper layer thickness. The stiffness degradation curves in Figure 4.29 show an unusual behaviour, highlighted also in the normalised curves in Figure 4.30, where the plots start from an initial value of the rotational stiffness, then go up to higher values and then go on decreasing more and more as usual. It looks a not common behaviour that could depend on the big instabilities recorded during the numerical analyses due to the very low values of stiffness and strength attributed to the lower liquefied layer, that do not represent real possible values to associate to the soil mechanical parameters.

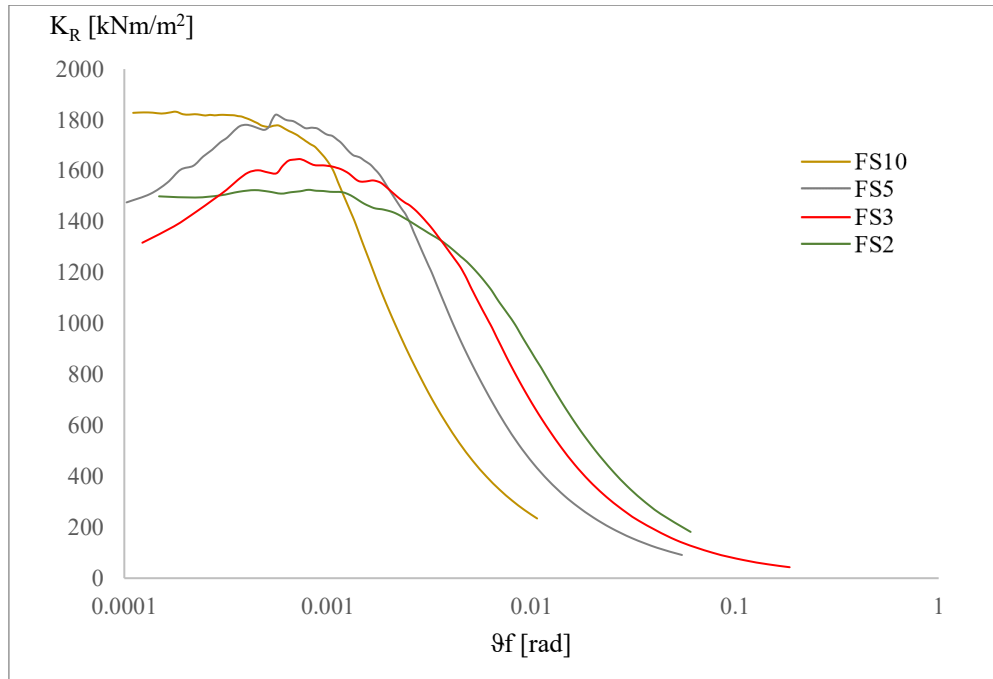


Figure 4.29- Rotational stiffness vs. rotation curves.

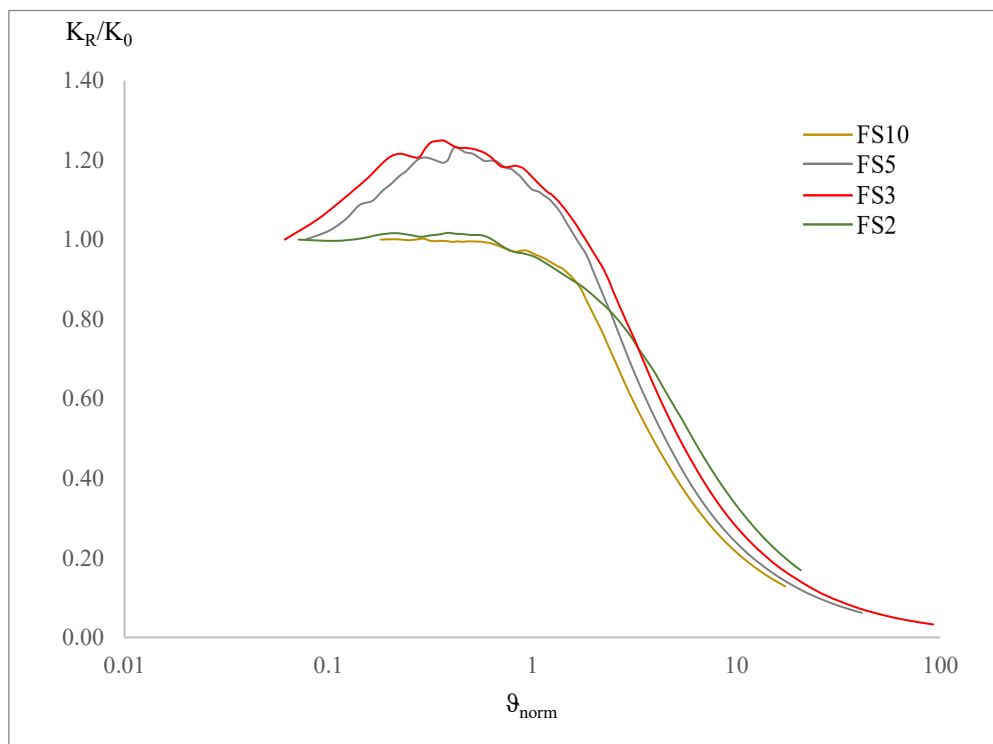


Figure 4.30- Normalised rotational stiffness vs. normalised angle of rotation.

4. Stiff sand over totally liquefied layer with $H_{crust}=3$ m.

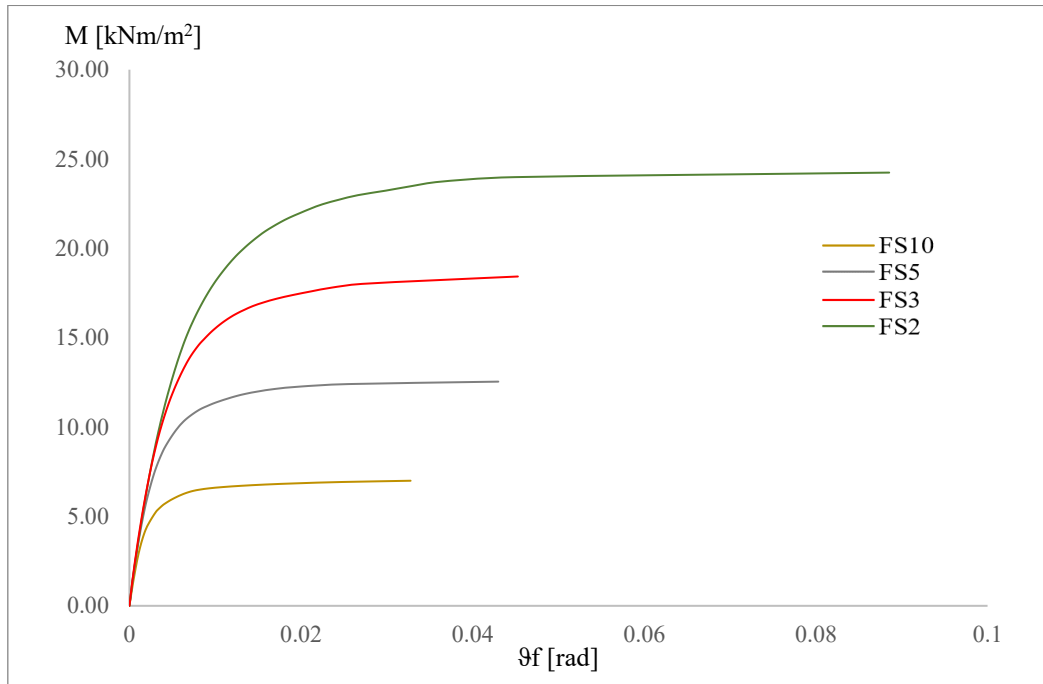


Figure 4.31 - Moment-rotation response of a strip footing on a 2-layered deposit.

The results obtained in these soil conditions show that the total liquefaction in the lower layer would influence relatively the high values of ultimate moment capacity achieved in the previous case of partial liquefaction with a $H_{crust}=3$ m. In fact, the results of the ultimate moment in the current case are not so far from the case of partial liquefaction, considering the large decrease in stiffness and strength associated to a higher value of the excess pore pressure ratio, U . It proves the importance of the upper “crust” thickness can be enough to mitigate the effects of liquefaction on the foundation.

The stiffness degradation curves in Figure 4.32 obtained from the interpretation of the numerical results are better than the ones of the previous case of $H_{crust}=1,5$ m, showing less instability in the initial values. Moreover, compared to the other cases, the strong decrease related to the development of plastic deformations together with the uplift starts in this case at very small values of the foundation rotation, especially for heavily loaded foundations.

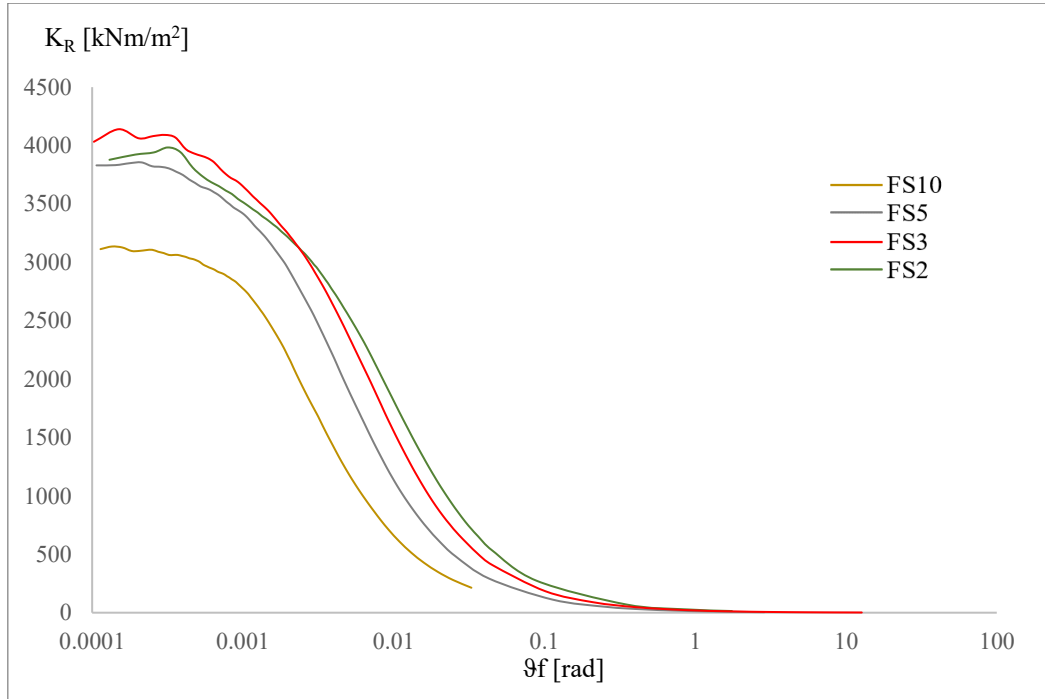


Figure 4.32- Rotational stiffness vs. rotation curves.

Also, in this case the normalisation of the stiffness-rotation curves looks managed.

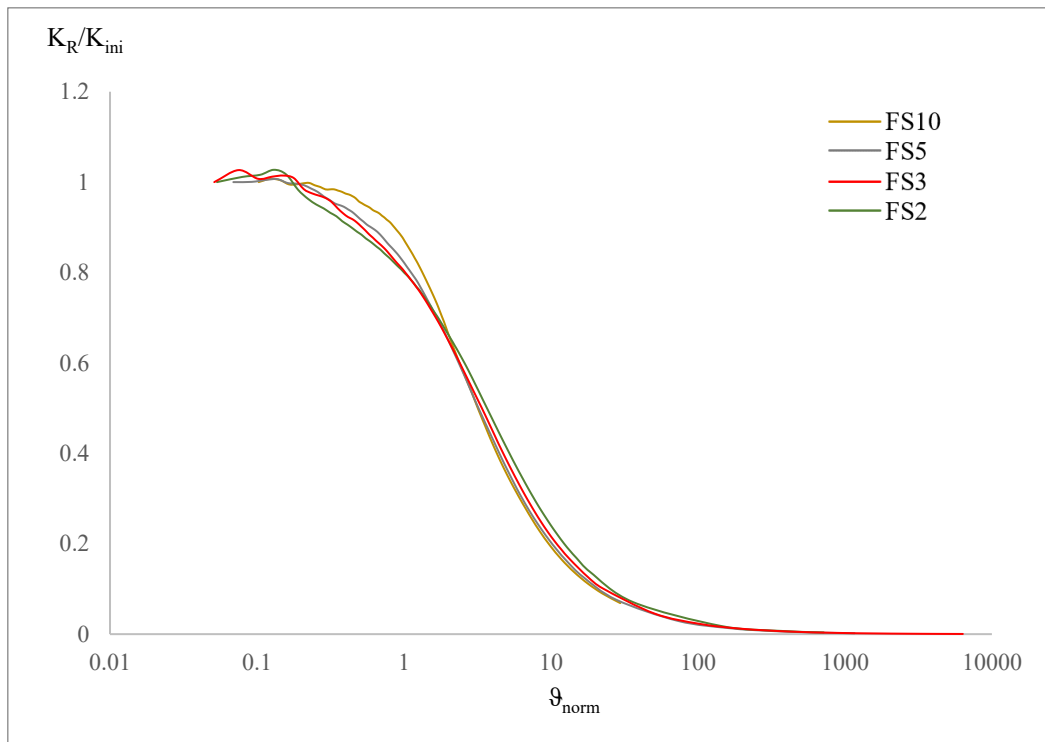


Figure 4.33- Normalised rotational stiffness vs. normalised angle of rotation.

5. Stiff clay over partially liquefied layer with $H_{crust}=1,5$ m.

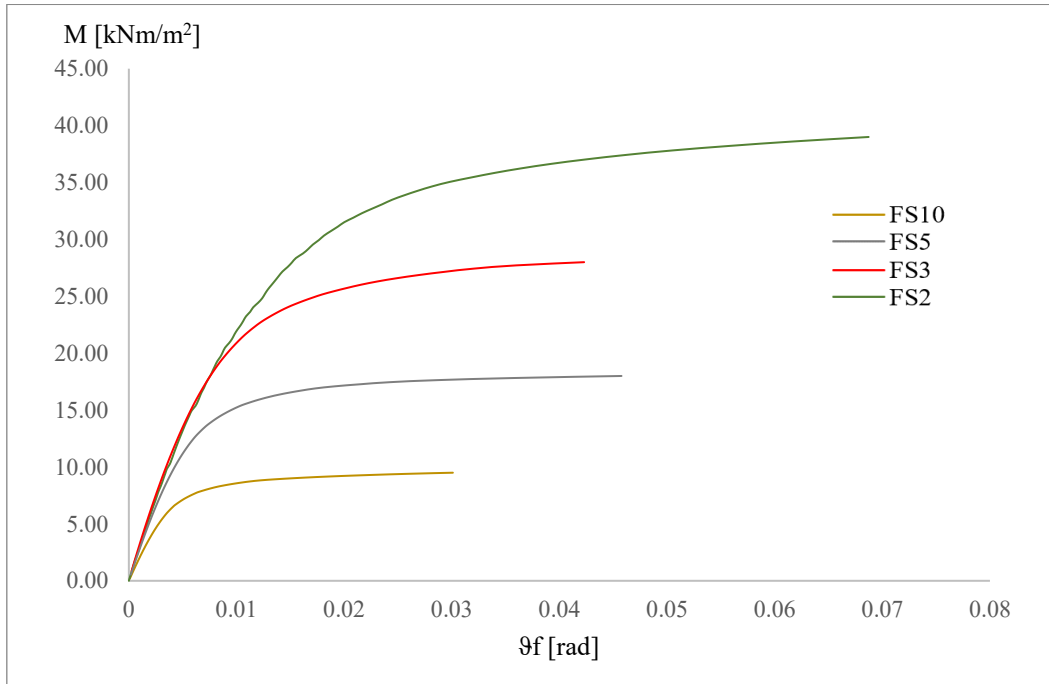


Figure 4.34 - Moment-rotation response of a strip footing on a 2-layered deposit.

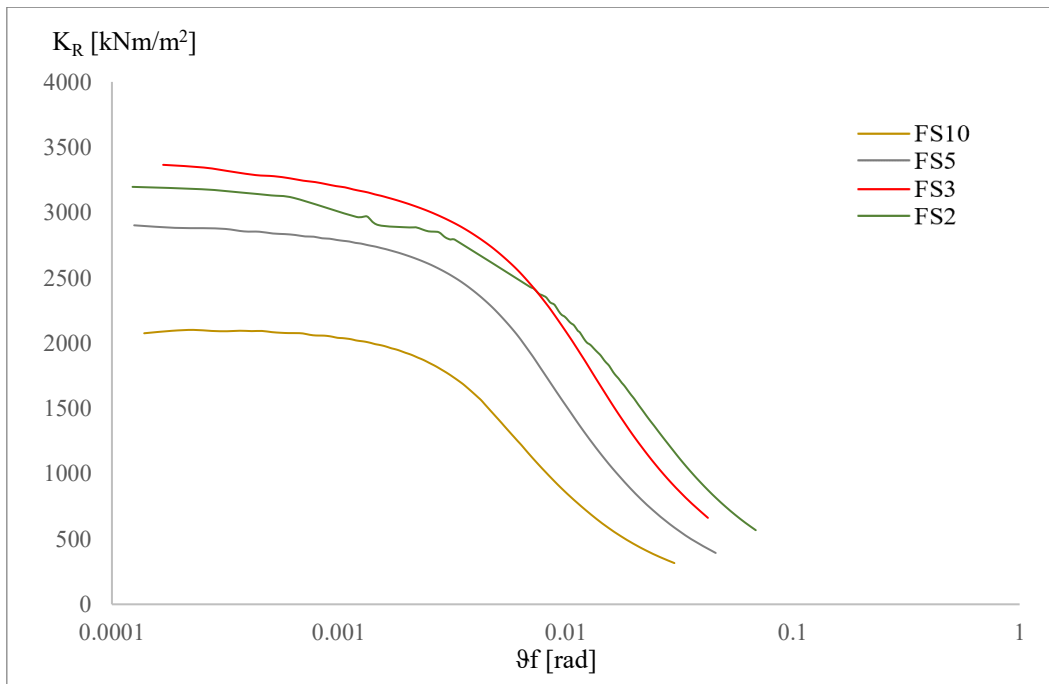


Figure 4.35- Rotational stiffness vs. rotation curves.

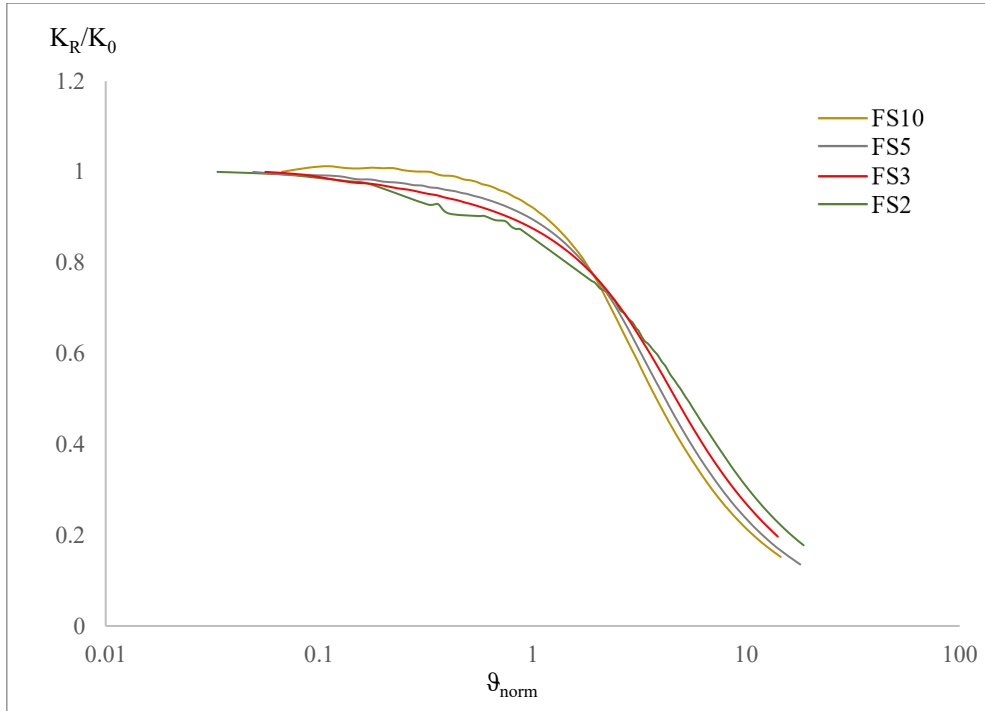


Figure 4.36- Normalised rotational stiffness vs. normalised angle of rotation.

6. Stiff clay over totally liquefied layer with $H_{crust}=1,5$ m.

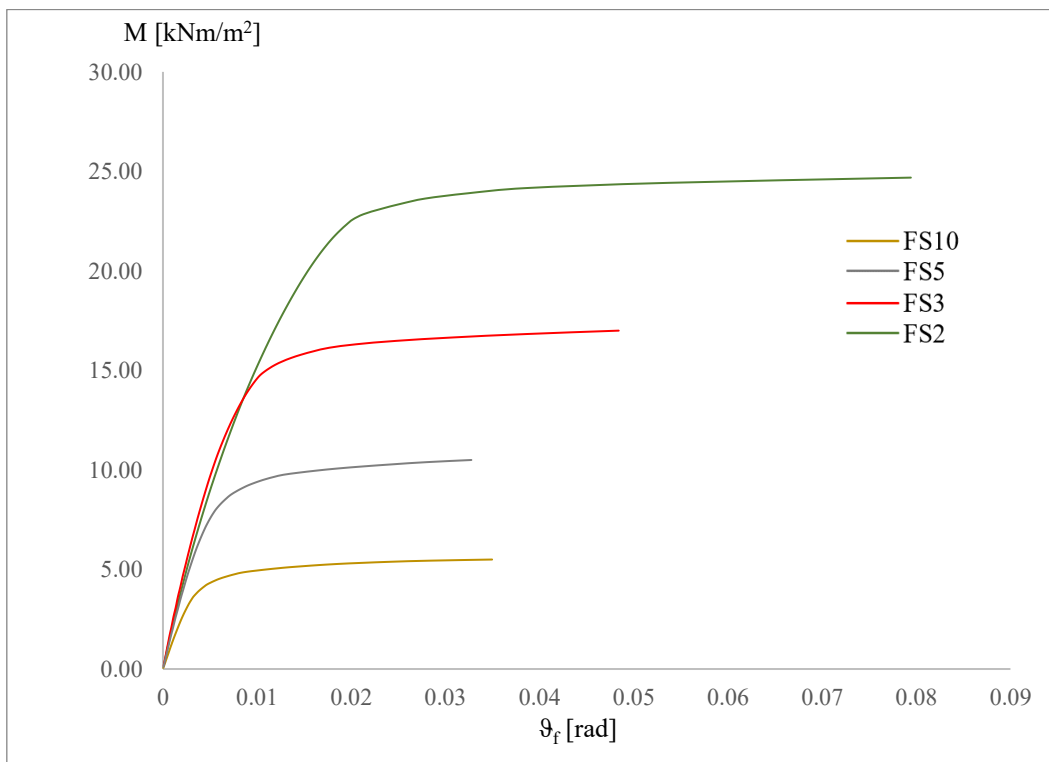


Figure 4.37 - Moment-rotation response of a strip footing on a 2-layered deposit.

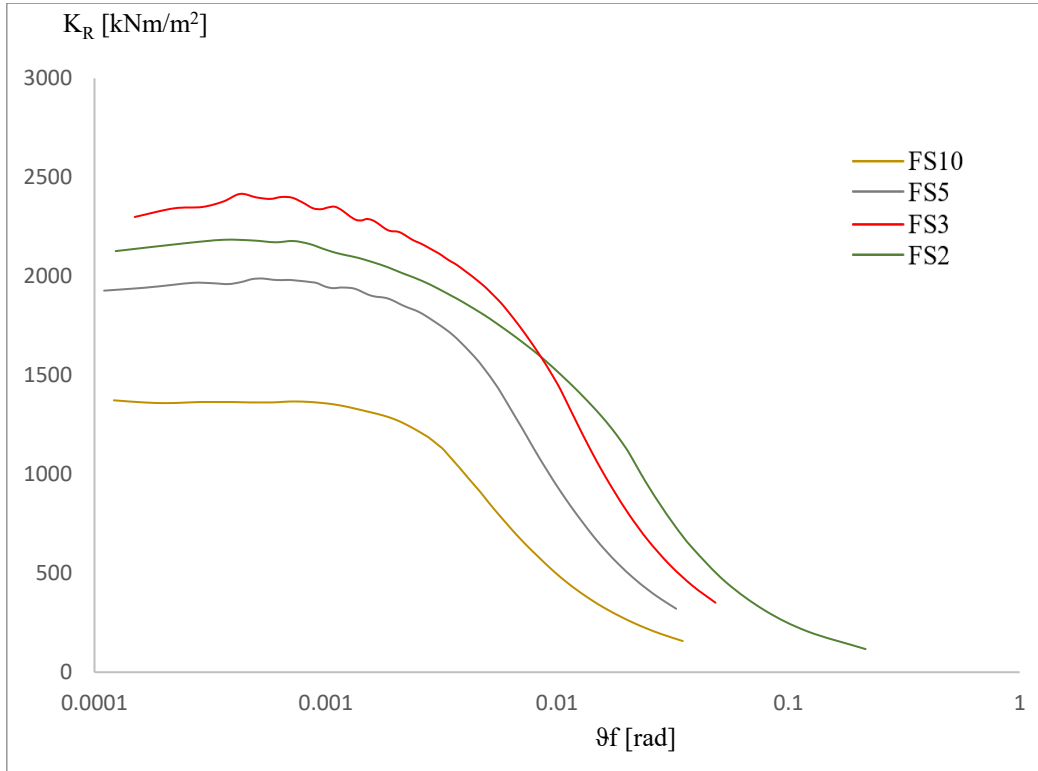


Figure 4.38- Rotational stiffness vs. rotation curves.

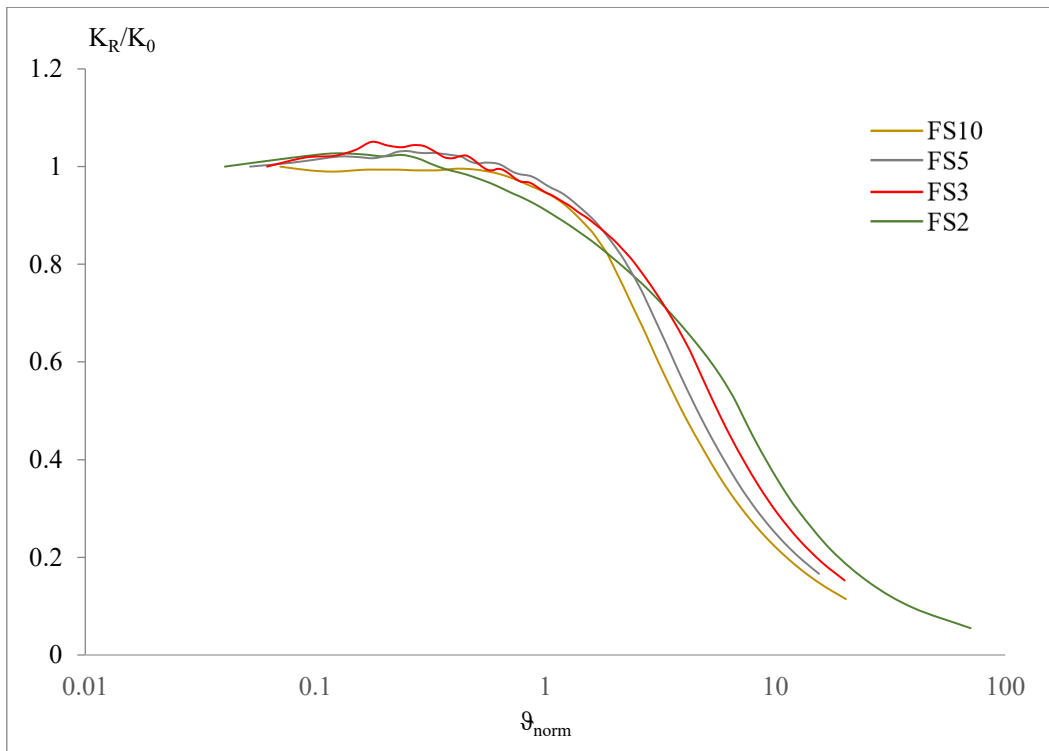


Figure 4.39- Normalised rotational stiffness vs. normalised angle of rotation.

The parametric study carried out changing the crust material in a purely cohesive one shows an evident difference in all the results for both levels of liquefaction considered in the lower layer. Looking at the $M-\vartheta_f$ plots in Figure 4.34 and Figure 4.37 the behaviour appears to be influenced by the sandy weaker layer underlying the clayey crust, showing a stronger slope of the initial trend for lower factors of safety, but in contrast, the point of the uplift initiation is clearer when the material and the geometric non-linearities are combined together.

The stiffness degradation curves show a marked initial plateau, more pronounced in correspondence of high factors of safety, in the same way as the homogeneous clayey soil (see Section 4.4) even though the initial rotational stiffness values are higher in higher factors of safety and progressively decreasing as for homogeneous sandy soils, meaning that the lower layer to has a stronger influence on the whole behaviour.

4.7 Conclusions

Through the numerical simulations that were presented that followed simplified systems in terms of loading conditions and model features, it is possible to describe the non-linear soil-foundation-structure system response to actions that simulate seismic perturbations (overturning moments).

From the results obtained in the current work it is clear that the soil-foundation behaviour is highly influenced by the combination of loads (vertical and moment) and by the mechanical properties of the supporting soil.

In the specific case of layered deposits with a partial or total liquefied lower layer, it is evident that, more than any other factor, the upper stiffer layer thickness influences the $M-\vartheta_f$ response, behaving like an isolation between the overlying system and the weaker lower layer. In fact, the higher the thickness, the more stable will be the response.

Moreover, in the same aforementioned case, the normalisation of the curves looks fairly well achieved, less in the specific case of the upper clayey soil layer.

Further research and a wider parametric study could result in a common solution approximating the response though a normalisation dependent on the factor of safety considered. However, the current results provide a useful reference point for exploring the mechanics of the problem and for the validation of more complex analyses. A larger number of numerical simulations, not only in function of a larger variety of loading

conditions for each case analysed in this work, but also for different configurations of the supporting soil, and different foundation geometries would be useful to define an analytical expression to use in design and assessment procedures. In particular, the current study only dealt with a 1m width strip footing that does not capture the deeper stresses and therefore some relationships will change with larger foundations.

Moreover, in the current study the excess pore pressure build-up ratio, U , defining the level of liquefaction with the assumptions considered and explained at the start, has been only qualitatively proposed on the basis of previous validated works but future research should deal with the development of a simplified procedure for the strength and stiffness of liquefiable soil underneath foundations.

Because of the high dependency on the soil mechanical features and on the thickness of the layers overlying the lower one, susceptible to liquefaction, together with a possible influence by the foundation size, the case study proposed in the following Chapter 5, aiming to prove the consistency in the results between the static push-over analyses and the seismic time-history numerical simulations, will be based on new $M-\theta_f$ curves built as a function of the specific investigated soil conditions and foundation geometry.

5. Chapter: Case Study

5.1 Introduction

The purpose of this chapter is to demonstrate the applicability of the moment-rotation curves for the simplified assessment of structural response of a building on a liquefiable soil deposit.

5.2 Case study inputs

The proposed case study considered a shallow founded bridge of 10 metres height characterised by a deck width of 10 metres and a flooring thickness of 0,8 metres. Two cases of investigation were considered; in the first case, referred to here as the “No Liquefaction” case, it has been supposed that the structure was supported by a quite weak homogeneous soil deposit, with purely frictional behaviour, non-susceptible to liquefaction due to the high material permeability while in the second case, the “Liquefaction” case, it has been assumed a potentially liquefiable 4 metres thick layer at 4 metres depth, overlying a gravelly soil layer, characterised by the same soil properties of the “No Liquefaction” model. In both cases of investigation, the model was assessed in the transverse direction, first, using the displacement-based assessment procedure using moment-rotation response curves, and then compared against effective stress time history analyses using three ground motion time series. The geometry of the model is shown in Figure 5.1.

The case study was deliberately developed as a simple elastic structure that strongly activated the foundation rotation mode of deformation to more easily investigate the simplified assessment procedure versus dynamic analyses. It could represent a realistic starting point for more complex future models.

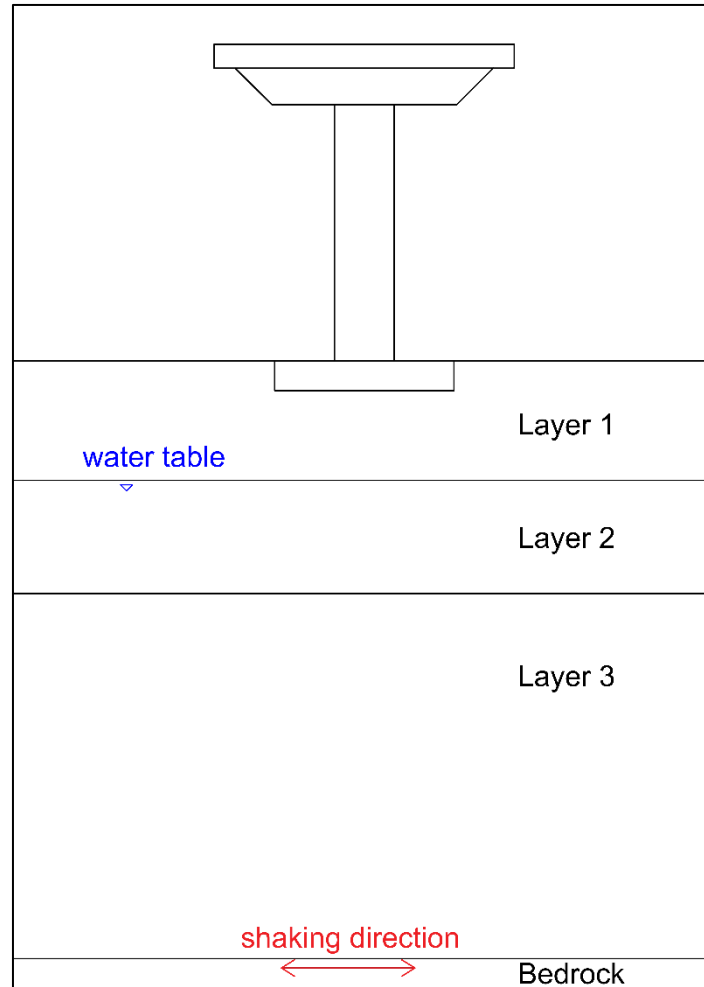


Figure 5.1- Geometry of the problem.

The seismic hazard level was defined based on the New Zealand legislation because the ground motions selected for the later dynamic analyses were taken from the database used in the study in Millen (2016) and they were properly scaled in accordance with the mentioned legislation. The seismic hazard level was set equal to 0.3 and the elastic site hazard spectrum for horizontal loading ($S_a(T)$) for a given return period was computed in accordance to New Zealand legislation NZS 1170.5:2004 (2004), as follows:

$$S_a(T) = C_h(T) \cdot Z \cdot R \cdot N \quad (5.1)$$

where $C_h(T)$ is the spectral shape factor and it varies with the site subsoil conditions, R is the return period factor, N is the near-fault factor.

The spectral shape factor was equal to 0.85 for a value of the corner period equal to 3 seconds, for sites with a shear wave velocity lower than 180 m/s. For a return period of

500 years the correspondent R factor was 1, as much as the N value for an annual probability of exceedance higher than 1/250.

Even though the hazard level followed the Standards in the NZS 1170.5:2004 (2004), and the earthquake actions were calculated through the criteria valid in New Zealand, it does not mean an inconsistency with the Italian site hazard levels, due to possible correspondence to the site specific spectral shape factors adopted in the Italian code (DM 14/01/2008 – “Norme Tecniche per le Costruzioni”).

The resulting value of the site spectral acceleration was 2.45 m/s^2 thus the elastic spectral displacements were computed as a function of $S_a(T)$ as follows:

$$S_d(T) = S_a(T) \left(\frac{T}{2\pi} \right)^2 \quad (5.2)$$

With the period T in a range between 0 and 4 seconds. Figure 5.2 illustrates a rough plot of the elastic spectral displacements, without taking into account the actual trend for low periods where the spectral acceleration is kept constant.

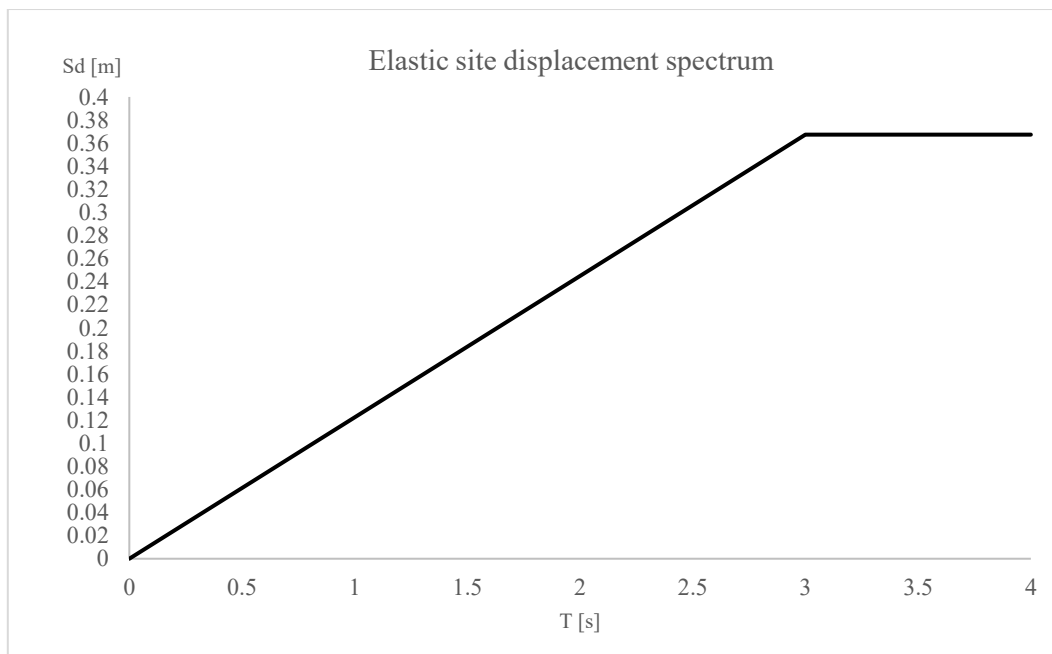


Figure 5.2 – Elastic site design spectrum.

Tables 18 and 19 summarise the soil deposit and building properties.

Soil Profile		
Parameters	Sandy Soil	
H_{tot} [m]	Total Soil Thickness	20
H_1 [m]	Layer 1 thickness	4
H_2 [m]	Layer 1 thickness	4
H_3 [m]	Layer 3 thickness	12
z_w [m]	Water Level	4
γ_{uns} [kN/m ³]	Dry Unit Weight	17
γ_{sat} [kN/m ³]	Saturated Unit Weight	19
e_0 [-]	Void Ratio	0.7
c [kPa]	Cohesion	0
ϕ' [°]	Angle of shearing resistance	30
ψ [°]	Angle of Dilatancy	-
G_0 [MPa]	Maximum Shear Modulus	65.5
ν'_{undr} [-]	Undrained Poisson's Ratio	0.495
K_0 [-]	Earth Pressure Coefficient	0.5
ζ [%]	Damping Ratio	2

Parameters	Rock	
z_R [m]	Rock Layer Level	20
γ_{uns} [kN/m ³]	Dry Unit Weight	22
γ_{sat} [kN/m ³]	Saturated Unit Weight	22
E [kN/m ²]	Elastic Modulus	8E+06
V_s [m/s]	Horizontal Shear Wave velocity	1220

Table 18-Soil deposit and rock properties.

Superstructure Parameters		
m_s [T]	Deck Mass	400
H_P [m]	Piers Average Height	10
L_D [m]	Influence Deck Length	20
W_D [m]	Influence Deck Width	10
H_D [m]	Deck Thickness	0.8
T [s]	Structure Fixed-base Natural Period	1
γ_c [kN/m ³]	Concrete Unit Weight	24
ζ [%]	Damping Ratio	5

Foundation Parameters		
m [ton]	Foundation Mass	-
D_F [m]	Depth of Embedment	1
B [m]	Width	6
L [m]	Length	6
EJ	Flexural Rigidity	1E+08
EA	Axial Rigidity	2E+06
ν [-]	Poisson's Ratio	0.25

Table 19-Building properties.

5.3 Estimation of the structure response

A displacement-based procedure for quantifying the building response for both cases of investigation based on the design spectra is here presented. It is based on the moment-rotation curves obtained from push-over analyses of the pier for both cases of investigation and detailed in section 5.4.

The traditional “fixed based” approaches used for the evaluation of the structural displacements assume that the soil and foundation behave as rigid bodies, thus the displacements are calculated as function of only the structural deformation, while the “SFSI procedures” account for the foundation rotational stiffness degradation and for the soil-foundation shear deformations during dynamic loading with a consequent modification to seismic demand on the superstructure (Paolucci et al., 2013). The displacement-based assessment approach adopted here is based on the approach presented by Millen, 2016, which is a modification of the displacement-based design procedure in Paolucci et al., 2009 that converts the non-linear behaviour into an equivalent linear response, accounting for the SFSI effects and foundation rotation. However, the procedure was modified to use the moment-rotation response curves obtained from Push-over analyses performed in PLAXIS 2D, rather than the stiffness reduction curves used by Millen, 2016.

Calculation

It should be noted that this procedure has not been calibrated for liquefiable soils thus, a slight discrepancy with the results from the dynamic analyses in Liquefaction case, detailed in section 5.5, was expected. The calculation steps followed for the assessment are outlined below:

1. Estimate the expected level of base shear, V_b . It should be estimated from the overturning moment on the foundation, M_{ot} . This value is iterated to find a compatible solution; however, an initial guess can be made as 50% of the foundation moment capacity, or by first assessing the fixed-base response of the structure.
2. Estimation of the foundation deformations. From the moment-rotation curve obtained from a push-over analysis of the soil-structure system (Section 5.4), the foundation rotation, ϑ_f , can be determined in correspondence with the foundation over-turning moment (conceptually in Figure 5.3), which can be estimated based on the base shear multiplied by the effective height.

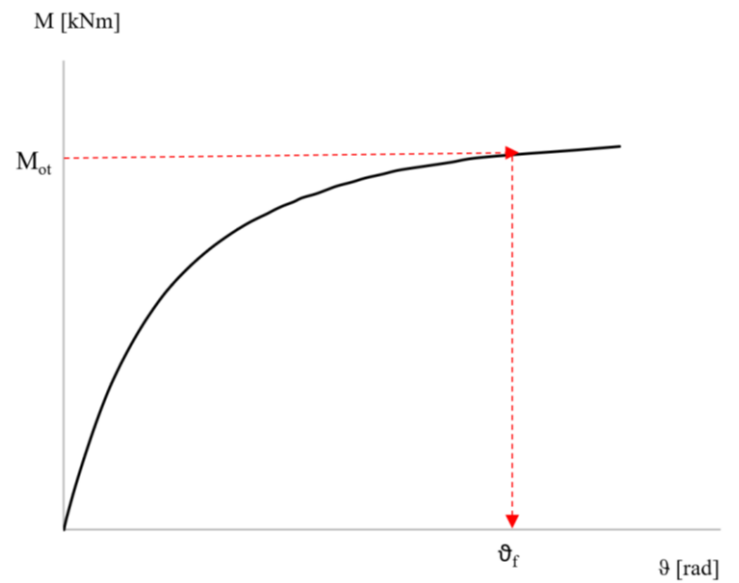


Figure 5.3 – Estimation of the foundation rotation from the M- θ curves.

The foundation rotation multiplied by the effective height corresponds to the displacement contribution from foundation rotation, $\Delta_{f,\theta}$. The initial value of the rotational stiffness, $K_{f\theta,0}$, meaning the rotational stiffness in correspondence of a very small value of the rotation (10^{-4} radians) can also be obtained directly from the push-over analyses.

3. Estimation of the superstructure deformation, Δ_{ss} as the ratio between the base shear, V_b , and the superstructure stiffness, k_{ss} , here the soil-foundation shear deformation has not been included as the soil-structure system was deliberately chosen to exhibit a large rotational response compared to the soil-foundation shear deformation. The calculation of the entire system deformation, Δ_{tot} , is therefore the sum of the foundation rotation contribution and superstructure deformations.
4. Determination of the displacement reduction factor (DRF), η_{sys} , as a combination of DRF from different mechanisms (foundation rotation, superstructure displacements) (Equation 5.3)

$$\eta_{sys} = \frac{\Delta_{ss}\eta_{ss} + \Delta_{f,\theta}\eta_{f,\theta}}{\Delta_{tot}} \quad (5.3)$$

where η_{ss} is set equal to 1 since the structure was considered elastic, and $\eta_{f,\theta}$ is computed using Equation 5.4 from Millen, 2016:

$$\eta_{f,\theta h} = \sqrt{\frac{1}{1 + 5(1 - e^{-0.15\Phi})}} \quad (5.4)$$

η_{sys} is a reduction factor that accounts for the non-linear energy dissipation from the superstructure and the foundation during seismic excitation.

The term Φ in the above expression represents the normalised angle of rotation in function of the uplift rotation and the superstructure height, differently estimated compared to the normalised angle of rotation in Chapter 4, in absence of a superstructure.

The current followed relationship is:

$$\Phi = \left(\frac{\vartheta_f}{\vartheta_{\text{uplift}}} \right)^{1-0,2\left(\frac{H}{B}\right) \times 10^{0,25}\left(\frac{H}{B}\right)} \quad (5.5)$$

5. Determination of the effective period (secant period), T_e . First the elastic spectral acceleration $S_e(T)$ was determined as a function of the site subsoil class factor, C_h , the hazard factor, Z , the return period factor, R and the near fault factor, N , according to the NZS 1170.5:2004 (2004) in correspondence of a corner period (T_c) equal to 3 seconds; then the corresponding elastic spectral displacement, $S_d(T_c)$ according to (Equation 5.6).

$$S_d(T_c) = S_e(T) \left(\frac{T_c}{2\pi} \right)^2 \quad (5.6)$$

and reduced using the system DRF.

The effective period was then computed as follows:

$$T_e = T_c \frac{\Delta_{\text{tot}}}{S_{d,r}} = T_c \frac{\Delta_{\text{tot}}}{S_d \eta_{\text{sys}}} \quad (5.7)$$

With $S_{d,r}$ the reduced corner spectral displacement.

6. Calculation of the effective stiffness, K_e , and of the base shear V_b .

$$K_e = \frac{4\pi^2 m_s}{T_e^2} \quad (5.8)$$

$$V_b = K_e \Delta_{tot} \quad (5.9)$$

7. Calculation of the new estimation of the overturning moment and a new estimation of the foundation rotation using the moment-rotation curves. If there is a discrepancy between the input values and the new ones, the procedure is repeated until the convergence is achieved.

The plots of the design displacement spectrum and of the reduced one that accounts for the SFSI effects and for the energy dissipation are shown in Figures 5.20 and 5.28.

The final results from the No Liquefaction case are here presented and compared with the Liquefaction ones and the results obtained from the expected behaviour when using the stiffness-reduction curves proposed in Millen, 2016 (for a homogeneous non-liquefiable deposit). The results (Liquefaction and No Liquefaction) are compared with the dynamic simulations results in section 5.6 of the chapter.

Parameters	No liquefaction		Liquefaction
	Millen, 2016	Push-over results	Push-over results
V_b [kN]	958	607	397
M_{ot} [kNm]	9580	6070	3970
ϑ_f [rad]	0.086	0.011	0.015
Δ_{ss} [m]	0.06	0.038	0.025
Δ_{tot} [m]	0.146	0.156	0.183

Parameters	No liquefaction		Liquefaction
	Millen, 2016	Push-over results	Push-over results
η_{sys} [-]	0.76	0.64	0.55
$S_a(T=3s)$ [m/s^2]	2.5	2.5	2.5
$S_{d,r}(T=3s)$ [m]	0.283	0.239	0.203
T_e [s]	1.55	1.97	2.7
K_e [kN/m]	6550	4076	2170

Table 20 – Simplified DBA procedure results for the estimation of the building response.

It can clearly be seen that the results obtained using the push-over curves estimate a larger foundation rotation (0.011rad) compared to (0.086rad) from Millen, 2016, and an even larger rotation for the liquefaction case (0.015 rad). The base shear values estimated with

the push-over analysis in both No liquefaction and Liquefaction cases are lower than Millen's results in correspondence of a larger rotation, showing a stronger soil stiffness decay in the numerical simulations.

5.4 Push-Over Analyses

In this section the attention is focused on a mechanism-based push over analysis in order to assess the equivalent response of the structure by using simplified procedures that consider the non-linear SFSI modifying the dynamic response of the structure.

Numerical Modelling

The numerical simulation was carried out with the commercial code PLAXIS 2D. This software, based on finite element method, is able to capture both the non-linear soil behaviour and cyclic degradation due to the application of a ground motion and account for the soil-foundation-structure non-linearity.

The “No Liquefaction” case, dealt with a homogeneous granular deposit characterised by a permeability high enough to not allow the development of liquefaction; in the second case of investigation, “Liquefaction” case, the middle layer (Layer 2) at 4 metres depth was modelled as a partially liquefied layer, for which stiffness and shear strength were degraded according to a reduction ratio later explained.

The full domain was modelled, choosing a plane strain deformation model, rather than using an axis symmetric boundary, because analyses that involve foundation rotation require the full domain to be modelled. The length of the domain was defined 10 times the width of the foundation for each side with a fully fixed boundary at the bottom and normally fixed side boundaries, in order to reproduce geostatic conditions in points far enough from the problem. The water head was defined at 4 metres depth considering all the soil layers below 4 metres were fully saturated.

For the “No liquefaction” case only one material type was modelled, using a Hardening Soil constitutive model, whose main features have been described in previous chapters. The main input parameters in the Hardening Soil model are given in Table 21.

The unloading/reloading reference stiffness was calculated as a function of the benchmark value of the maximum shear modulus, G_0 (see Table 18); it was first computed using the corresponding G_{ur}^{ref} , dividing G_0 by 2,5 (as suggested by PLAXIS manual, 2017)

and then, because E_{ur}^{ref} represents a real elastic stiffness, it was computed by the expression (5.10).

$$E_{ur}^{ref} = 2G_{ur}^{ref}(1 + \nu_{ur}) \quad (5.10)$$

The E_{50}^{ref} and E_{oed}^{ref} were determined dividing E_{ur}^{ref} by 3. The exponential power parameter for the stress-level dependency, m , defined as the slope of trend line in $\log(\sigma_3/p_{ref})$ - $\log E_{50}$ space was set equal to 0,55 because it is usually in the range of 0,4-0,7 for sands. The earth pressure coefficient was calculated through Jaky's law and an isotropic permeability was assumed for the entire deposit ($k_x = k_y$).

No liquefaction

HS model

Parameters	Definition	Value
γ_{uns} [kN/m ³]	Unsaturated Unit Weight	17
γ_{sat} [kN/m ³]	Saturated Unit Weight	19
e_0 [-]	Void Ratio	0.700
m	Power for Stress-level Dependency of Stiffness	0.55
c' [kPa]	Cohesion	0
ϕ' [°]	Angle of Internal Friction	30
ψ [°]	Angle of Dilatancy	-
E_{ur}^{ref} [MPa]	Unloading/reloading Stiffness	63
E_{50}^{ref} [MPa]	Secant Stiffness in Standard Drained Triaxial Tests	21
E_{oed}^{ref} [MPa]	Tangent Stiffness for Primary Oedometer Loading	21
ν'_{ur} [-]	Unloading/Reloading Poisson's Ratio	0.200
ν'_{undr} [-]	Undrained Poisson's Ratio	0.495
K_0 [-]	Earth Pressure Coefficient	0.5
σ_t [kPa]	Tensile Strength	0
p_{ref} [kPa]	Reference stress for stiffness	100
k [m/s]	Permeability	1E-05

Table 21-Soil parameters for HS model.

For the Liquefaction case, the middle layer (from 4 to 8 metres depth) was modelled as a partially liquefied layer. It was assumed again a Hardening Soil model for all the layers, Layer 1 and 3 were modelled with the same material parameters used in “No Liquefaction” case.

In order to reproduce the soil shear strength and stiffness degradation associated to the phenomena of liquefaction, the soil in Layer 2 was set to an approximated strength and stiffness by assuming a level of pore pressure build up.

The weaker (liquefied) layer was characterised by a degraded angle of internal friction, meaning a degradation of the bearing capacity during the shaking calculated as a function of the actual friction angle in pre-liquefaction condition by using the analytical expression suggested by Cascone and Bouckovalas,1998 (see Chapter 3) and using an excess pore pressure ratio (U) equal to 0,8, considering that the applied load from the overlying building results in higher effective stress and pore water flow to the free-field would hinder build-up of pore pressure.

The stiffness degradation has been simulated through a reduction in the horizontal shear wave velocity and thus, proportionally to the reduction of the maximum shear modulus, G_0 . The initial value of the horizontal shear wave velocity was first computed corresponding to the benchmark value of the maximum shear modulus, according to the following expression:

$$G_0 = V_s^2 \rho \quad (5.11)$$

where ρ was the dry soil density.

Then, it was reduced 4 times, following the suggestions in the study carried out in Karatzia et al.,2017 where the numerical results seem to be in a suitable agreement with the experimental results, and by the new reduced value, the degraded shear modulus $G_{,liq}$ was calculated and used to determine the input parameters in PLAXIS.

The assumed reduction in stiffness and in shear strength derived from a rough approximation of the real behaviour of a liquefied soil. The cyclic behaviour of a liquefied soil (conceptually described in Figure 5.4) is different from non-liquefiable soils. In fact, in non-liquefiable soils the initial tangent stiffness, corresponding to the maximum one, decreases with the amplitude of shear strain, as illustrated in Figure 3.10.

In liquefiable soils the increasing number of cycles leads to a pore pressure build-up therefore, for a specific cycle corresponding to a specific value of the excess pore pressure ratio, the stiffness measured at very low strains drops to very small values and then it increases at high strain levels.

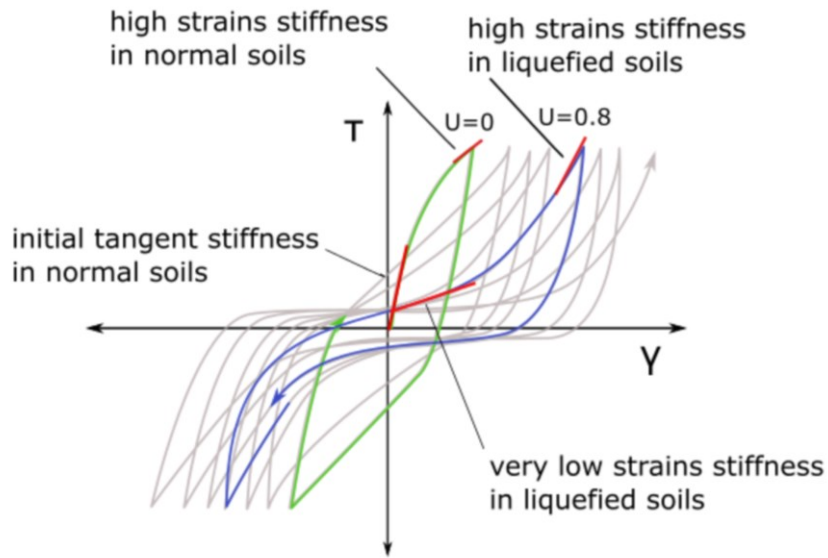


Figure 5.4 – Liquefied soil behaviour.

In order to capture this condition, an equivalent behaviour was assumed in between the two extreme stiffness levels in correspondence of $U=0.8$ and a new stiffness at very low strains was assumed for the partially liquefied. In Figure 5.5 an illustration is presented of the assumed $U=0.8$ behaviour and showing the estimated initial stiffness would be.

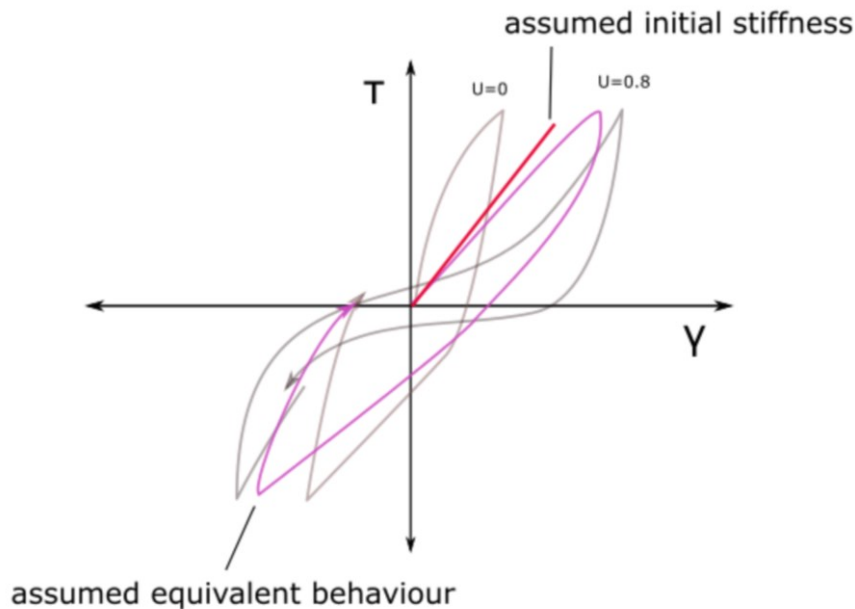


Figure 5.5 – Assumed equivalent liquefied behaviour.

In Table 22 the degraded soil parameters are summarised for Layer 2.

Liquefaction-Push Over Analysis		
HS model-Layer 2		
Parameters	Definition	Value
$E_{ur}(\text{liq})$ [MPa]	Unloading/reloading Stiffness	10
$E_{50}(\text{liq})$ [MPa]	Secant Stiffness in Standard Drained Triaxial Tests	3.3
$E_{oed}(\text{liq})$ [MPa]	Tangent Stiffness for Primary Oedometer Loading	3.3
ν'_{ur} [-]	Unloading/Reloading Poisson's Ratio	0.200
ν'_{undr} [-]	Undrained Poisson's Ratio	0.495
K_0 [-]	Earth Pressure Coefficient	0.843
$\phi'(\text{liq})$ [°]	Angle of Internal Friction	9
k [m/s]	Permeability	1E-06

Table 22- Input parameters for HS model in the liquefied layer (Layer 2).

The numerical models in both cases of investigation present also a lower thin layer which represents the upper part of the bedrock and whose parameters are shown in Table 18; this is unnecessary for the push over analyses in which it could be substituted by using a boundary conditions but it was included in the model because of subsequent dynamic analyses where the bedrock must be considered.

The interface elements were entered between all the lines forming the embedded foundation and the surrounding soil in order to allow for a proper modelling of soil-foundation interaction. They were modelled with the same properties of the adjacent material and with a null tensile strength. The roughness coefficient was set equal to 1.

The moment-rotation response was determined considering the structure subjected to a horizontal force, representing the seismic force, applied at the top corner, increasing step-by-step from zero to a value close to the ultimate condition (F_u). This mentioned value of the horizontal force was calculated dividing by the total height of the structure, H , a value of the moment close to the foundation moment capacity, M_u , that for non-liquefiable soils can be determined from the expression in Gajan et al., 2005 as follows:

$$M_u = \frac{N_{app}B}{2} \left(1 - \frac{1}{FS} \right) \quad (5.12)$$

where N_{app} is the axial load applied to the foundation from the superstructure and FS is the bearing capacity factor of safety.

The factor of safety is the ratio between the ultimate axial load and the actual axial load from the superstructure; in the two cases of investigation the applied vertical load,

corresponding to the building weight, was the same but there was a consistent change in the ultimate bearing capacity, calculated following the analytical relationships in Chapter 3, due to the degradation of the angle of shearing resistance assigned to Layer 2 in Liquefaction case.

The Table 23 summarises the resulting values.

	No Liquefaction	Liquefaction
N _{app} [kN]	3924	3924
N _u [kN]	43230	7580
FS [-]	11	1.93
M _u [kNm]	10700	5675
F _u [kN]	1070	567.5

Table 23- Ultimate capacity values.

The superstructure was assumed to behave as a linear elastic SDOF shear-type frame, whose upper beam was modelled as rigid; the entire mass of the structure was considered concentrated in the upper beam, whose geometry was simplified in a reduced length and without considering cantilevers. The actual stiffness of the structure was considered belonging to the two massless piers, characterised by a height of 10 metres.

The equivalent stiffness to assign to the piers was calculated in function of the mass and of the fundamental period of the structure (see eq. 5.13) and from it the piers flexural rigidity was determined with the formulation for a shear type frame (eq. 5.14).

$$K_{ss} = \frac{4\pi^2 m_s}{T^2} \quad (5.13)$$

$$EI_{ss} = \frac{K_{ss} h^3}{24} \quad (5.14)$$

The squared foundation was modelled as a massless body, one metre embedded in the soil. All the structural elements were modelled with plates. The geometrical features are summarised in Table 19.

The analyses were performed in 3 different stages:

- Initial phase: the calculation type was “K₀ procedure” in which there was the direct generation of initial effective stresses, pore pressure and state parameters, according

to PLAXIS manual. In this stage all the loads, structures and interfaces were deactivated;

- Phase 1: the calculation type was “Plastic” which meant an elastoplastic drained (or undrained) analysis. This phase started at the end of the initial phase and it was used to simulate the execution of the construction so the structural elements, the interface element and the vertical line load were activated. The drained conditions were set for the two cases of investigation. The numerical parameters were the default ones except for the tolerated error which was decreased to a value equal to 0,01. The displacements were reset to zero in order to avoid negative effect on further calculations;
- Phase 2: The calculation type was “dynamic”. This type of calculation allowed to follow the gradual process of deformation of the points under the footing with accuracy, avoiding the instability in the response. Using this type of calculation, the horizontal force was applied step-by-step to the system, therefore a dynamic value at each time step, equal to the input value of the force times the multiplier (chosen equal to 1) was defined. At the dynamic time equal to zero the force was equal to zero; at the maximum time step the input value of the action was equal to the maximum desired for the analysis. The total dynamic time was set proportional to the value of the applied force.

In this phase, the drainage behaviour of all the soil layers was set to “Undrained (A)” for both cases of investigation, in order to simulate a seismic condition in which the rate of loading is supposed to be higher than the rate under which pore pressures dissipate. Figure 5.6 shows the final numerical model.

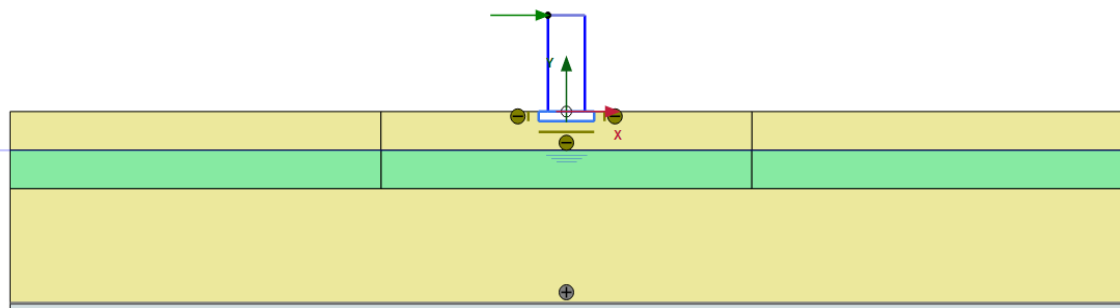


Figure 5.6- Numerical model.

Numerical results

The moment-rotation response was indirectly obtained from the numerical results of the Phase 3, the last one, in which the static vertical load and the horizontal force were

combined together; the incremental values of the foundation rotation were calculated as the difference between the incremental vertical displacements registered in the two corners (A, C in Figure 5.7) of the foundation base, divided by the base width.

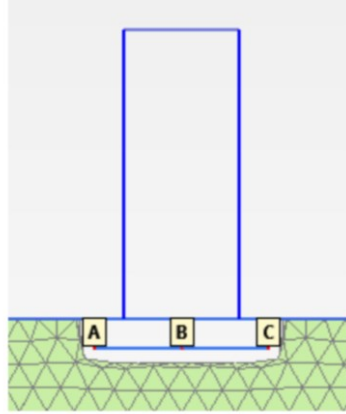


Figure 5.7- Queried points for rotation calculation.

$$\vartheta_i = \frac{(u_{yi}^L - u_{yi}^R)}{B} \quad (5.15)$$

The incremental moment was calculated multiplying the horizontal force value entered for the analysis by the height of the structure and then by the ratio between the i-step and the last step:

$$M_{f,i} = \frac{\text{Step}_i}{\text{last Step}} F_{\text{app}} H_s \quad (5.16)$$

Figure 5.8 shows the resulting plots from the two cases of investigation.

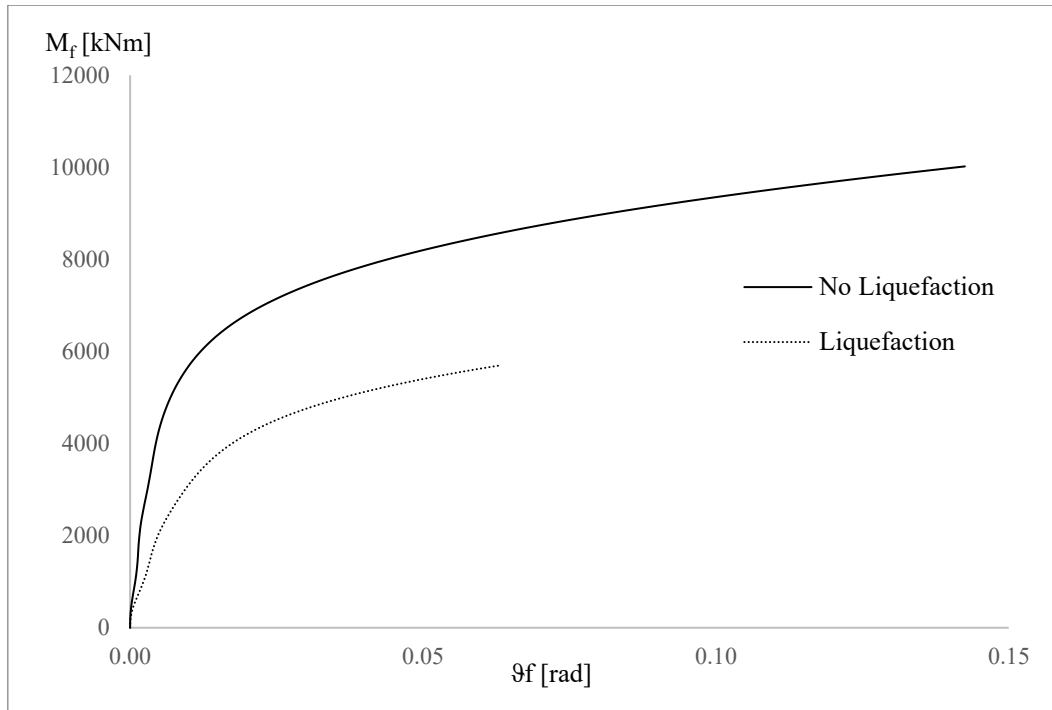


Figure 5.8 – Moment-rotation responses of the shallow founded building.

5.5 Dynamic numerical simulations

Ground motions selection

In order to assess the dynamic response of the investigated building, a set of three ground motions were selected from the NGA-West2 database (Ancheta et al., 2013) of records used in the study proposed in Millen, 2017, and scaled to a hazard level $Z = 0.3$ for use in New Zealand legislation NZS 1170.5:2004 (2004). The mentioned ground motions, with peak ground accelerations in the range of 0.27g and 0.36g, are spectrum compatible, referring to an expected elastic spectrum built, according to the New Zealand legislation NZS 1170.5:2004 (2004), in function of a seismic hazard factor (Z) equal to 0.3 and a given return period of 500 years.

Figure 5.9, Figure 5.10 and Figure 5.11 show the selected ground motions, representing the input motions in the dynamic analyses entered at the base of the model in terms of time-history accelerations.

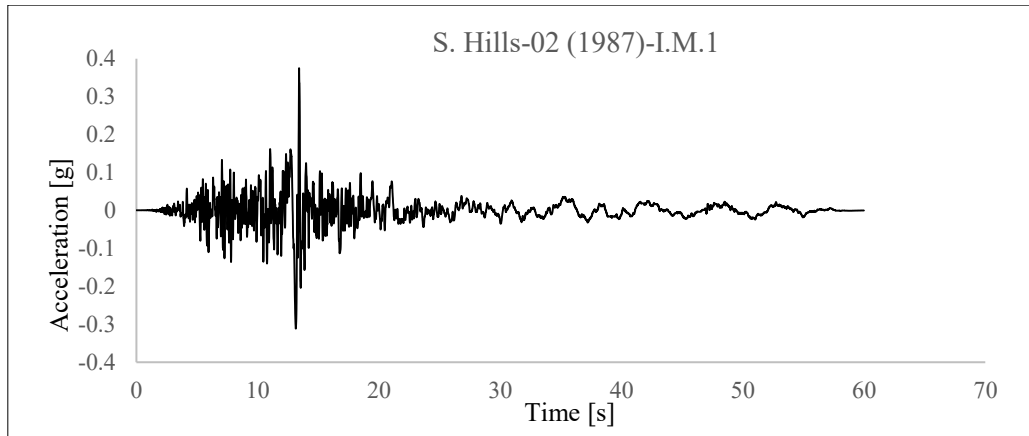


Figure 5.9-Time-history of Input Motion 1 (I.M.1).

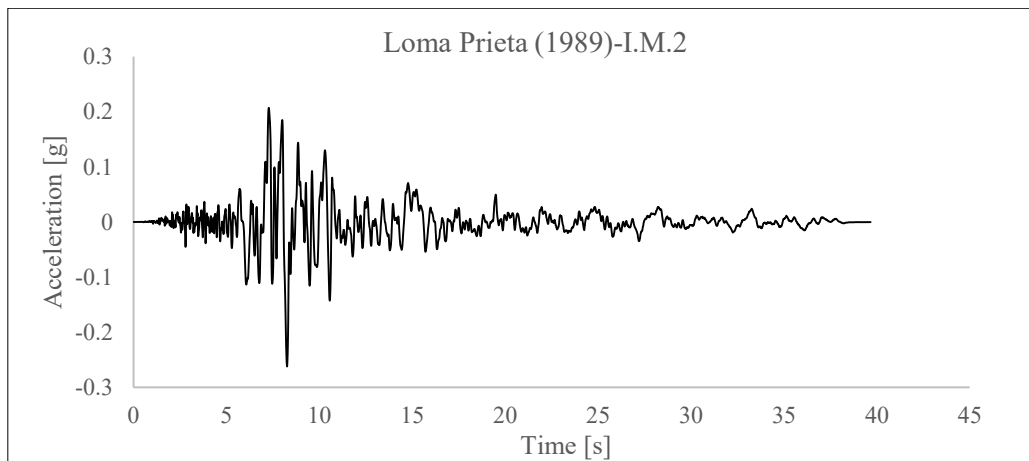


Figure 5.10- Time-history of Input Motion 2 (I.M.2).

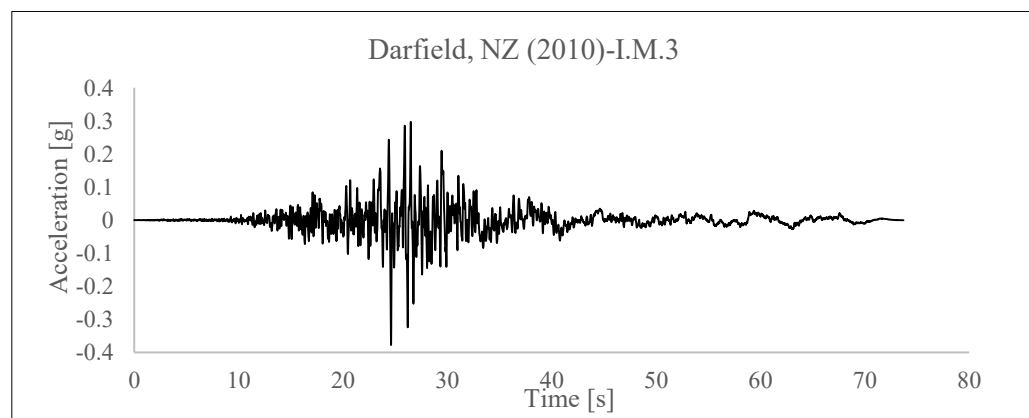


Figure 5.11- Time-history of Input Motion 3 (I.M.3).

The Seismosignal software was used to scale the input motions and obtain the correspondent elastic displacement response spectra at a damping of 5% Figure 5.12. In section 5.6 the input motion spectra are properly compared with the surface response

displacement spectra resulting from the dynamic numerical analyses in the two cases of investigation and with the design spectra, commonly used to represent seismic loading in pseudo-static seismic analysis of structures.

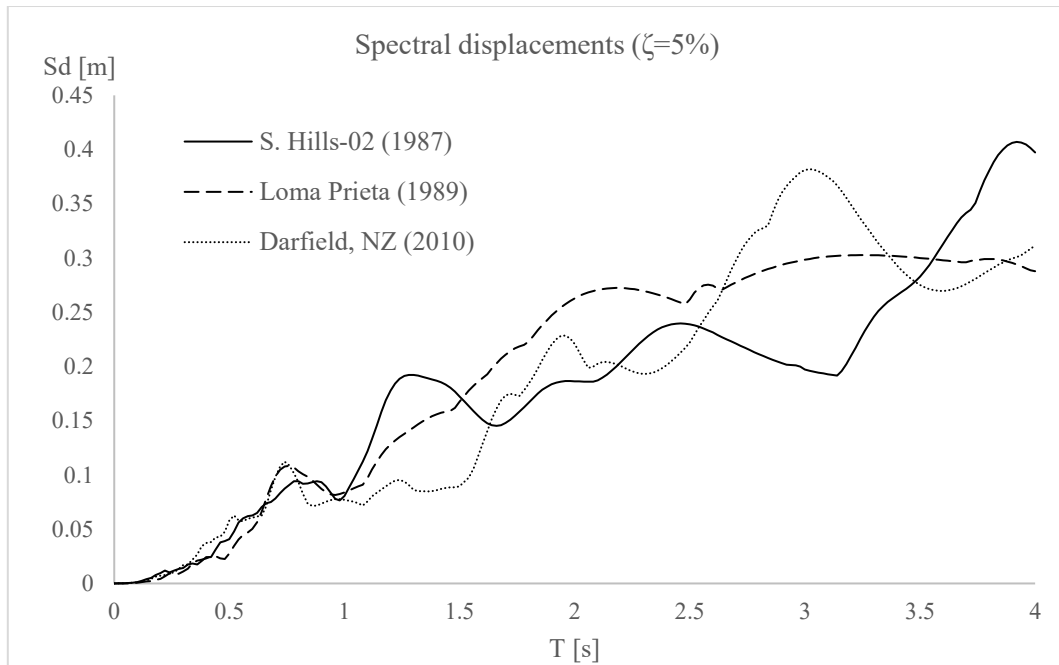


Figure 5.12- Elastic response displacement spectra at $\zeta=5\%$.

Numerical modelling

The validation of the predicted results in the previous section was achieved through dynamic analyses considering three different ground motions.

In both the push-over and dynamic analyses, the superstructure was simulated as lumped-mass concentrated at the top of the pier and pier was modelled as a deformable system with proper flexural rigidity because the flexibility of the superstructure influences the dynamic response of the whole system, transferring a more realistic load to the foundation. The shallow square foundation was modelled as a rigid body in order to simulate a reinforced concrete structural element.

The calculation process consisted of an initial condition phase, a second phase considering the presence of the building changing the soil stress and strain level and a third dynamic calculation in which the ground motion was entered and the seismic waves were propagated across the deposit. The first two phases were static thus, the same boundary conditions applied in the push-over analyses were chosen. In the third phase the lateral boundaries were set as “tied degrees of freedom” while the base boundary was set

as “compliant base”. As suggested by PLAXIS, 2017 manual an interface element at the bottom of the model was entered but not activated and the static fixities were deselected. The tied degrees of freedom for the vertical boundaries allowed the nodes at the left and at the right boundaries to be connected to each other and to follow the same displacement. The compliant base is a combination of a line prescribed displacement and a viscous boundary and allows for input of an earthquake motion while still absorbing incoming waves. In order to apply this boundary condition a thin layer of bedrock was entered in the model and modelled with a linear-elastic material absorbing the downward propagating waves and thus capturing the effect of continuation of seismic waves into the underlying deep soil.

The ground motion was introduced as a prescribed line displacement in the x-direction at the bottom of the model in terms of time-history accelerations with a multiplier factor of 0,5, meaning that only half of the motion (the upward wave) was propagating while the downward wave was absorbed by the underlying layers.

For the dynamic calculation a maximum number of steps was required in order to allow the software to determine the time-step δt according to the expression:

$$\delta t = \frac{\Delta t}{m \cdot n} \quad (5.17)$$

where Δt is the dynamic time interval parameter, that corresponds to the earthquake duration, m is the maximum number of steps that was selected equal to the number of steps composing the time-history and n is the number of sub-steps automatically determined.

Because the maximum number of steps to select in the adopted version of PLAXIS is set to 10000, the time-histories about the ground motions 1 and 3, whose number of time-steps exceeded this number, were uploaded with a duration of 50 seconds, corresponding to a total number of time-steps equal to 10000. The shorter duration only removed to low amplitude shaking at the end of the record (see Figures 5.8÷5.10) that could be expected to have no influence on the peak response of the soil-structure system.

In the No Liquefaction case of the investigation all the layers were modelled with Hardening soil with small-strain stiffness model (HSsmall) which is based on HS model but in addition allows the generation of the hysteretic damping in cyclic loading. Thus,

two additional parameters were entered together with the material properties already defined for the HS model Table 21 in the previous analyses:

- very low strain shear modulus, G_0 ;
- the shear strain level in correspondence of a decrease to about 70% of the initial shear modulus, $\gamma_{0.7}$. This parameter was assumed equal to 0.03 %, in accordance with the shear modulus decay curve in Seed and Idriss, 1991 (Mean Limit).

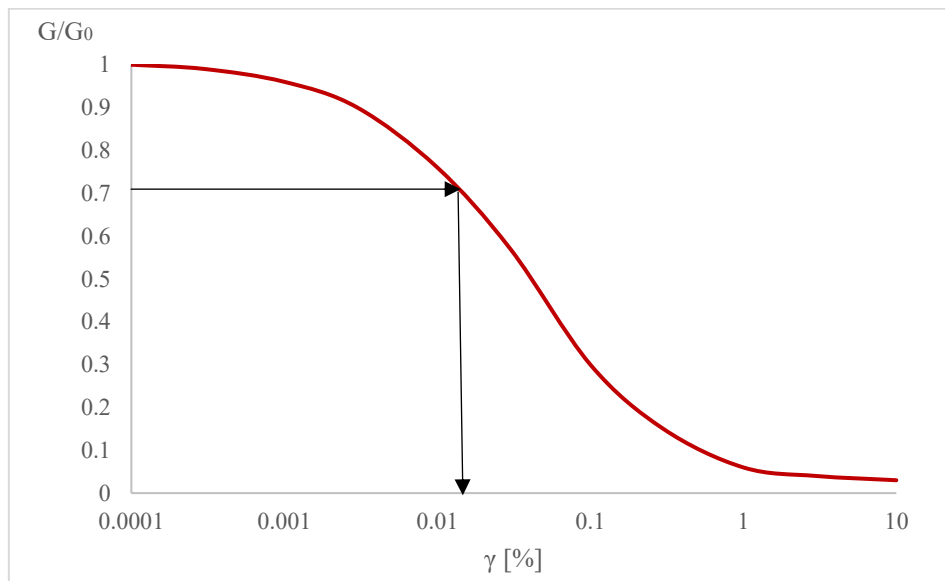


Figure 5.13 –Stiffness-strain behaviour of soil (Seed and Idriss, 1991).

In the Liquefaction case of investigation for proper modelling of the conditions of excess pore pressure generation, Layer 2 was modelled with UBC3D-PLM soil model, but only for the earthquake phase, while it was modelled with Hardening Soil model in the previous phases in order to correctly generate the initial stress state. During the dynamic calculations undrained conditions were assigned to the liquefiable soil layer.

UBC3D-PLM soil model

UBC3D-PLM soil model is a user-defined constitutive model implemented in PLAXIS which allows for proper modelling of seismic liquefaction behaviour of sands and silty clays. It is nonlinear, elasto-plastic, effective-stress based model capable of capturing evolution of excess pore pressures under undrained cyclic analysis. UBC3D-PLM model was presented by Tsegaye, 2010. The elastic behaviour is characterised by two key parameters, the shear modulus (G_e) and a bulk modulus (B_e), defined as follows:

$$G^e = K_G^e P_a \left(\frac{\sigma'}{P_a} \right) \quad (5.18)$$

$$B^e = \alpha G^e \quad (5.19)$$

where K_G^e is the elastic shear modulus multiplier, P_a is the atmospheric pressure, σ' is the mean stress in the plane of loading and α is a constant that depends on the elastic Poisson's ratio (Hardin, 1978).

The key model parameters are based on the normalised standard penetration test values ($N_{1,60}$) and they are defined as follows:

- elastic shear modulus multiplier, computed as follows:

$$K_G^e = 21,7 \cdot 15 \cdot (N_{1,60})^{0,333} \quad (5.20)$$

- elastic shear exponent, $m_e = 0,5$
- bulk modulus coefficient, computed as follows:

$$\alpha = \frac{2(1 + \nu)}{3(1 - 2\nu)} \quad (5.21)$$

- elastic bulk modulus multiplier, computed as follows:

$$K_B^e = \alpha K_G^e \quad (5.22)$$

- elastic bulk exponent, $n_e = 0,5$
- plastic bulk modulus multiplier, computed as follows:

$$K_G^p = K_G^e \cdot (N_{1,60})^2 \cdot 0,003 + 100 \quad (5.23)$$

- plastic bulk exponent, $n_p = 0,4$
- friction angle at constant volume, φ_{cv}
- peak friction angle, computed as follows:

$$\varphi_p = \varphi_{cv} + \frac{N_{1,60}}{5} \quad (5.24)$$

- failure ratio, computed as follows:

$$R_f = 1 - \frac{N_{1,60}}{100} \quad (5.25)$$

Other additional parameters (fac_{hard} and fac_{post}) are required to be defined in order to modify the material response before and after liquefaction triggering.

For this study the value of $N_{1,60}$ to assign to the liquefiable layer was unknown, however it was back-calculated as a function of the reference value of the maximum shear modulus used in the previous analyses. In particular it has been considered that $K_G^e \cdot p_{ref}$ is approximately equal to G_0^{ref} (with $p_{ref} = 100$ kPa) thus K_G^e was calculated and by the expression defined for K_G^e , $N_{1,60}$ was determined. Table 24 summarises the input parameters for the UBC3D-PLM Soil Model.

Liquefaction- Dynamic Analysis		
UBC3D-PLM Soil Model		
Parameters	Definition	Value
γ_{uns} [kN/m ³]	Unsaturated Unit Weight	17
γ_{sat} [kN/m ³]	Saturated Unit Weight	19
e_0 [-]	Void Ratio	0.700
$N_{1,60}$	Normalised, Corrected SPT value	3
c' [kPa]	Cohesion	0
ϕ_{cv} [°]	Friction Angle at constant volume	30
ϕ_p [°]	Peak Friction Angle	30.3
K_G^e	Elastic Shear Modulus Multiplier	625.7
m_e	Elastic Shear Exponent	0.5
K_B^e	Elastic Bulk Modulus Multiplier	834.3
n_e	Elastic Bulk Exponent	0.500
K_G^p	Plastic Bulk Modulus	116.8
n_p	Plastic Bulk Exponent	0.4
R_f	Failure Ratio	0.93
σ_t [kPa]	Tensile Strength	0
k [m/s]	Permeability	1.00E-06
fac_{hard}	Densification Factor	1
fac_{post}	Post-Liquefaction Factor	1

Table 24 - UBC3D-PLM Soil Model Parameters.

Definition of the Rayleigh damping

Different from the previous analyses, a Rayleigh damping was required to be defined both for the soil and for the structural elements in order to have a more realistic behaviour towards the seismic excitation.

Rayleigh damping is expressed through the damping matrix C , proportional to a linear combination of mass (M) and stiffness (K) matrixes as follows:

$$[C] = \alpha[M] + \beta[K] \tag{5.26}$$

Where α and β are mass-proportional and stiffness-proportional Rayleigh damping coefficients, respectively. PLAXIS 2D is able to generate the mentioned coefficients through the definition of damping ratios, ζ , and target frequencies. It was first defined the target damping ratios, then the first target frequency corresponding to the predominant frequency of the whole soil layer or structure and the second target frequency as the closest odd number obtained from the ratio between the fundamental frequency of the input signal at the bedrock and the fundamental frequency of the whole soil layer or structure (Hudson, Idriss and Beirkae, 1994).

The fundamental frequency of the deposit, representing the frequency in correspondence of the expected maximum amplification, was calculated in function of the average value of the shear wave velocity in the whole deposit, V_s , and of the layer thickness, H as follows:

$$f = \frac{V_s}{4H} \tag{5.27}$$

The fundamental frequencies of the input signals at the bedrock were taken from the Fourier spectra.

Table 25 presents the input values of frequencies and damping required for α and β determination.

	Soil			Building		
	I.M.1	I.M.2	I.M.3	I.M.1	I.M.2	I.M.3
ζ [%]		2			5	
f [Hz]-Target 1		2.2			1	
f signal [Hz]	4.55	1.4	2.63	4.55	1.4	2.63
f [Hz]-Target 2	3	1	2	4.55	2	3

Table 25 – Input parameters for Rayleigh coefficients determination (I.M. is for Input Motion).

Mesh definition

A proper way to define the finite element size in dynamic analyses is related to the wavelength associated to the maximum frequency component of the input motion. In particular the element size should be small enough to capture high-frequency motions of small wavelengths. It is suggested (Kuhlemeyer and Lysmer, 1973) to set the upper limit of the element size equal to 1/8 of the smallest wavelength thus,

$$l_e \leq \frac{\lambda_{\min}}{8} = \frac{V_{s,\min}}{8f_{\max}} \quad (5.28)$$

Considering that at a reference value of 100 kPa of the stress level the maximum shear modulus was equal to 65.5 MPa, and that the correspondent horizontal shear wave velocity was about 194 m/s, a Vs profile was defined with soil deposit depth and a minimum value of 105 m/s was found for the shear wave velocity; moreover, the maximum frequency considered was equal to 4.55 Hertz and taken from Input Motion 1. Therefore, the maximum element size resulted equal to 2.88 metres. The adopted version of PLAXIS 2D did not allow to define the average element size thus, a fine density was selected keeping attention in refining in an area close to the foundation and subsequently it was checked that the biggest element into the mesh was characterised by a size lower than the computed threshold. It was found out that the elements far from the problem were characterised by a size exceeding the upper limit while the elements close to the problem respected the imposed limit.

5.6 Dynamic analyses results

The numerical results were expressed in terms of building total displacement, Δ_{tot} , and in terms of foundation rotation, ϑ_f for a comparison with the push-over results.

The building total displacement was calculated for each time step, δt , as the difference between the registered horizontal roof displacement and the horizontal displacement measured in a surface point far enough from the building. The foundation rotation was determined following the same procedure explained in the previous section.

No Liquefaction

Figures 5.14÷5.19 show the plots about the No liquefaction case obtained from the three input ground motions (I.M.1, I.M.2, I.M.3) and the Table 26 presents a comparison between the predicted and the actual results.

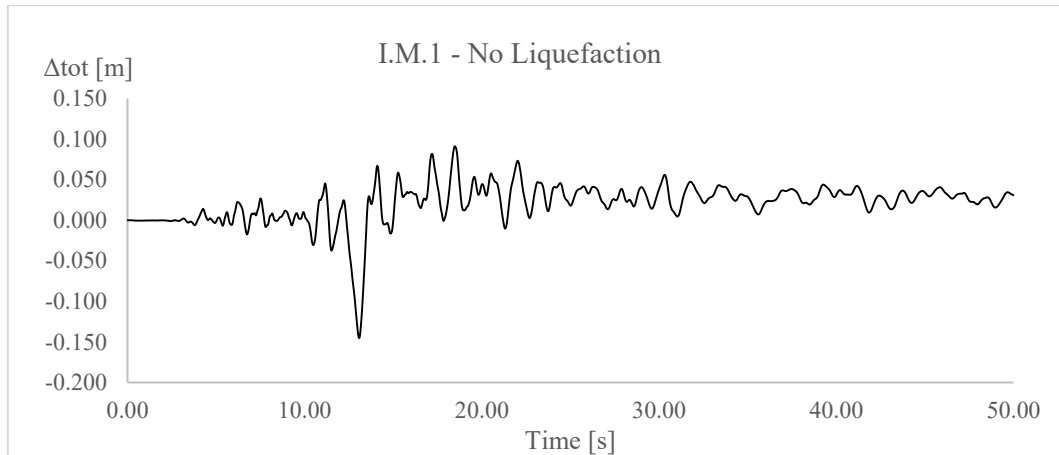


Figure 5.14 – No Liquefaction: Building total displacement registered for Input Motion 1 (I.M.1).

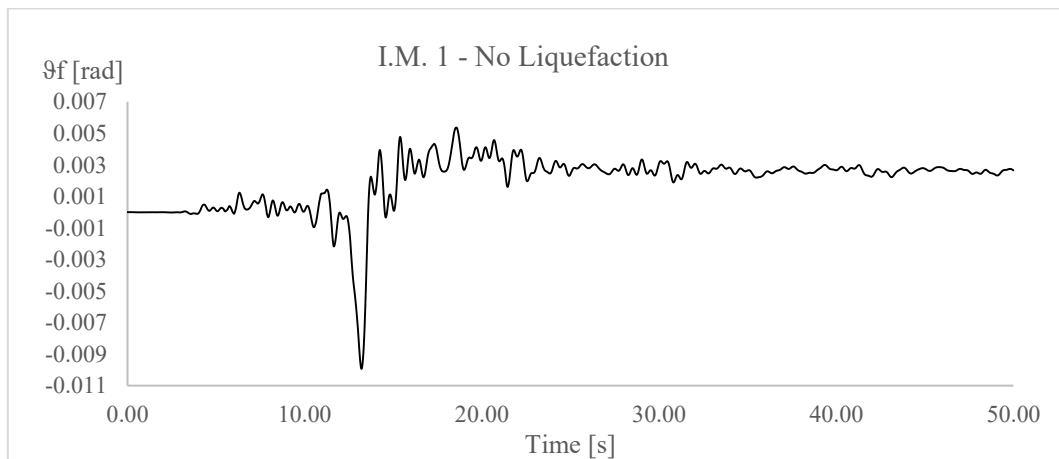


Figure 5.15 – No Liquefaction: Foundation rotation registered for Input Motion 1 (I.M.1).

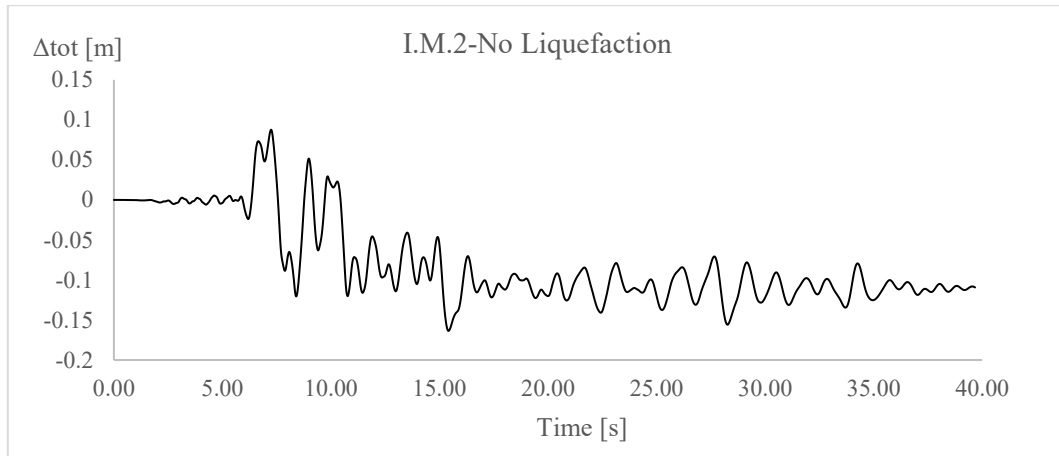


Figure 5.16 – No Liquefaction: Building total displacement registered for Input Motion 2 (I.M.2).

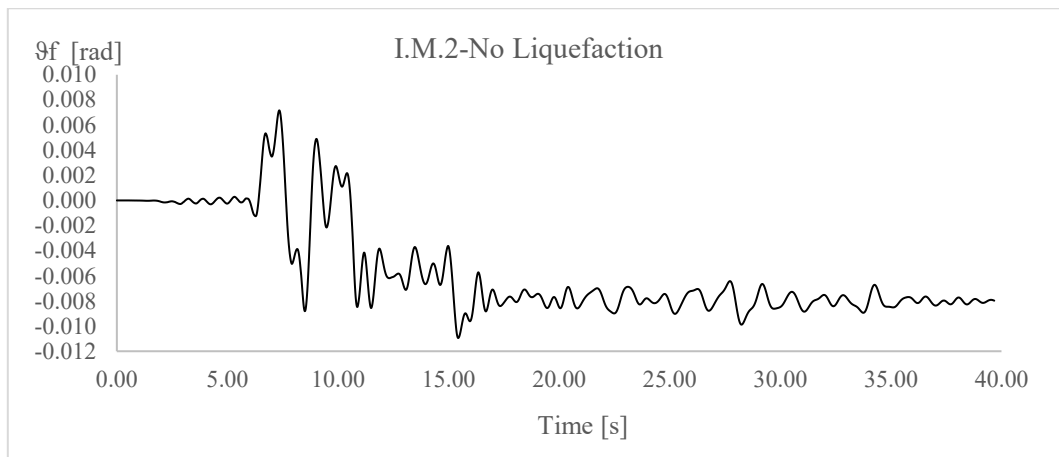


Figure 5.17 – No Liquefaction: Foundation rotation registered for Input Motion 2 (I.M.2).

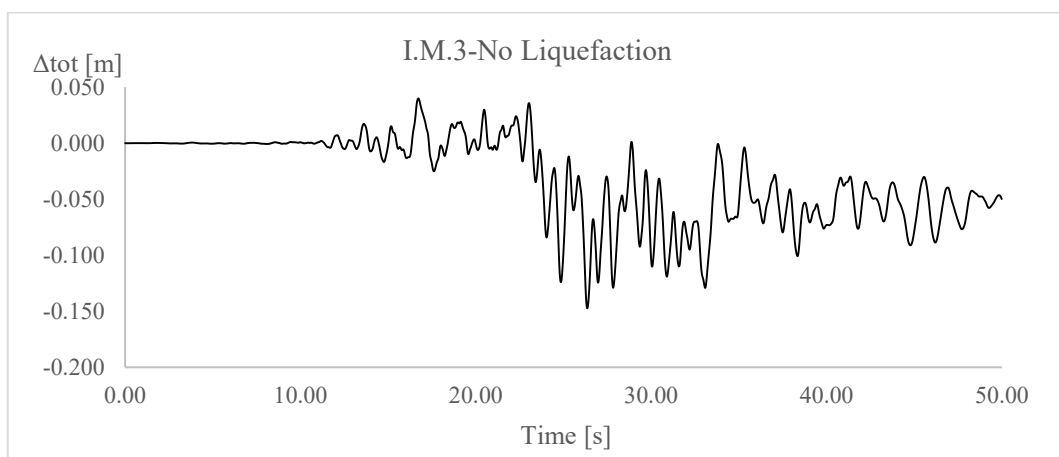


Figure 5.18 – No Liquefaction: Building total displacement registered for Input Motion 3 (I.M.3).

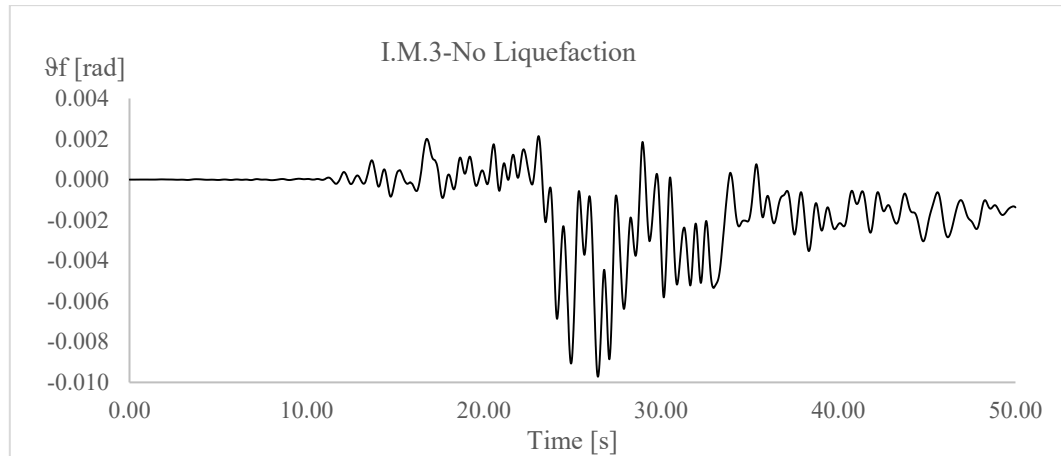


Figure 5.19 – No Liquefaction: Foundation rotation registered for Input Motion 3 (I.M.3).

Parameters	No liquefaction				
	Millen, 2016	Push-over	I.M.1	I.M.2	I.M.3
$ \vartheta_f $ [rad]	0.086	0.0118	0.0098	0.011	0.0097
$ \Delta_{tot} $ [m]	0.146	0.156	0.143	0.163	0.145
T_c [s]	1.55	1.97	-	-	-

Table 26 – Push-over vs. Dynamic analyses results.

Table 27 shows the differences in percentage between the results from the displacement-based assessment and the results from the dynamic analysis.

Parameters	No liquefaction				
	Millen, 2016	Push-over	Percentage difference I.M.1	Percentage difference I.M.2	Percentage difference I.M.3
$ \vartheta_f $ [rad]	0.086	0.0115	15%	5%	16%
$ \Delta_{tot} $ [m]	0.146	0.156	8%	4%	7%

Table 27 – Push-over vs. Dynamic analyses percentage differences.

In “No Liquefaction” case it is immediately apparent the good agreement between the push-over procedure results and the dynamic study ones, both in terms of foundation rotation and superstructure deformation.

The input motion response displacement spectra at a damping level of 5 % were plotted against the resulting site spectra and compared in Figure 5.20; moreover, the reduced elastic design spectrum built on the basis of the resulting parameters from the displacement-based assessment procedure is presented together with the original one.

The reduced design spectral displacements are lower than the original 5% damped spectral response because they take into account the effects of foundation energy dissipation related to the non-linear decay of the rotational stiffness due to non-linear soil-foundation deformations such as soil yielding and the foundation uplift and shear deformations. It could be interpreted as a beneficial effect in considering SFSI in the design and assessment of building response because of the potential of all the non-linear mechanisms at the base that contribute in reducing the shaking energy entering the structure, however it can result in larger displacements.

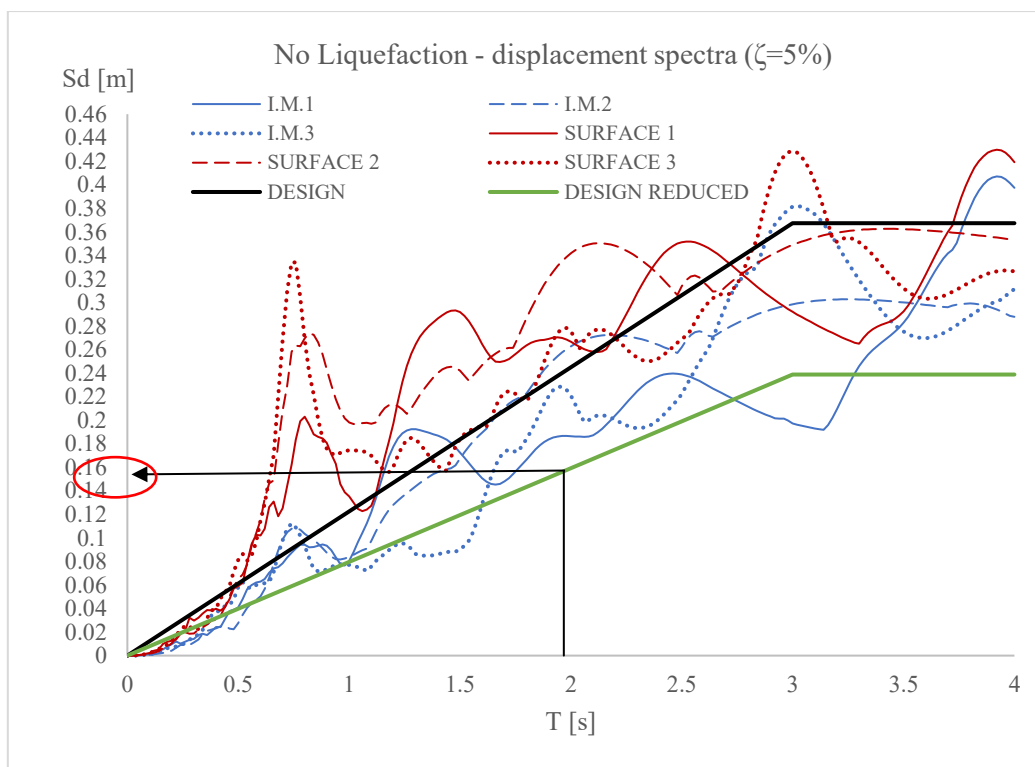


Figure 5.20 – No Liquefaction: Elastic bedrock and site response displacement spectra at $\zeta=5\%$ vs. design spectra.

Liquefaction

Figures 21÷26 show the results from the Liquefaction case in correspondence of the three input motions, while

Table 28 presents a summary of the maximum values obtained in terms of building deformation and foundation rotation and a comparison with the predicted values from the push-over analyses.

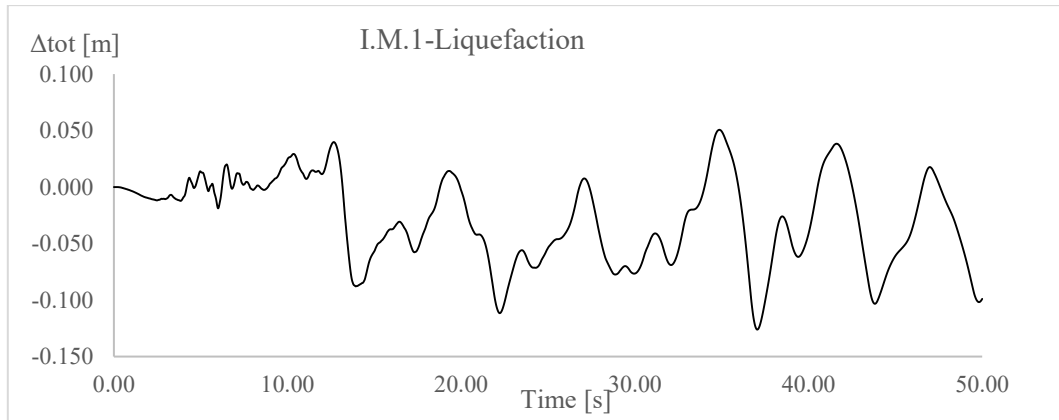


Figure 5.21 – Liquefaction: Total displacement registered for Input Motion 1 (I.M.1).

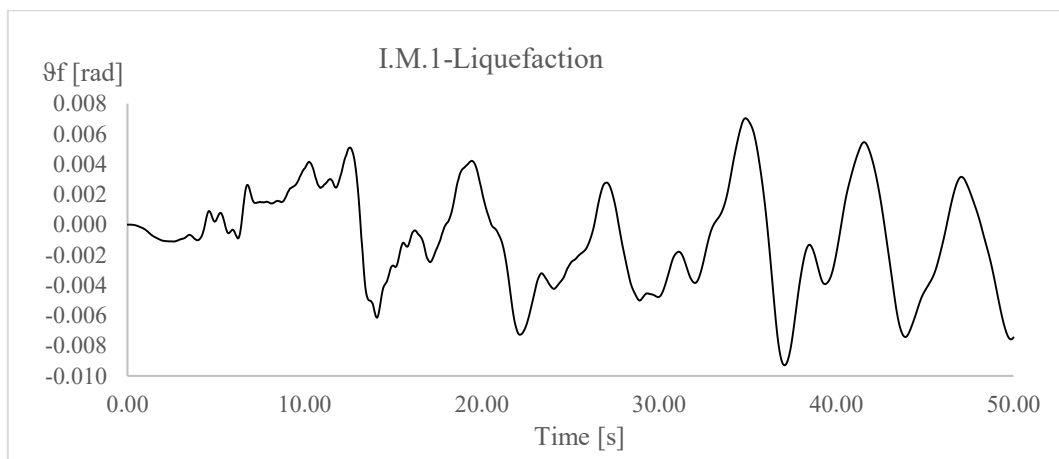


Figure 5.22 – Liquefaction: Foundation rotation registered for Input Motion 1 (I.M.1).

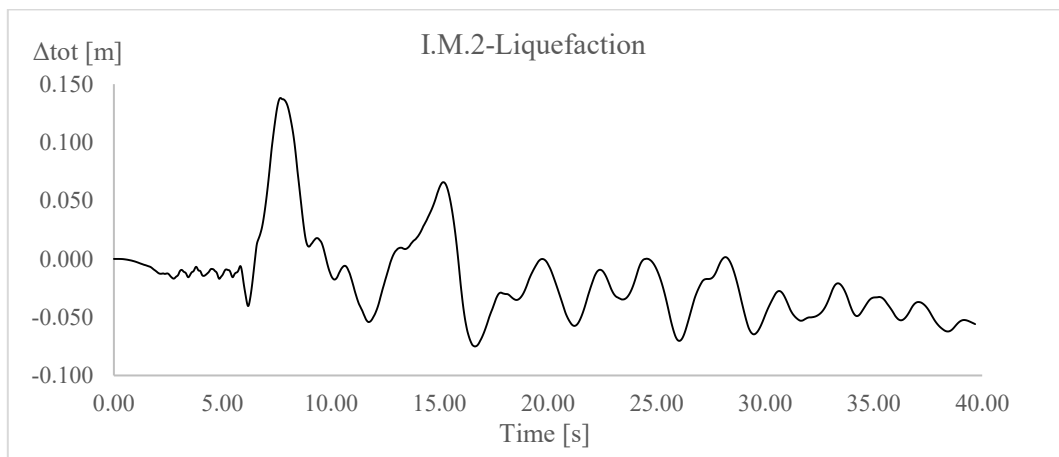


Figure 5.23 – Liquefaction: Total displacement registered for Input Motion 2 (I.M.2).

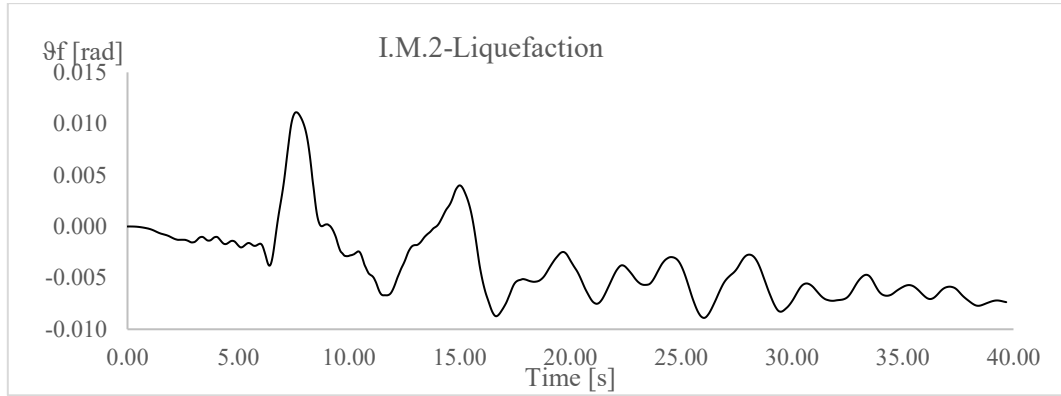


Figure 5.24 –Liquefaction: Foundation rotation registered for Input Motion 2 (I.M.2).

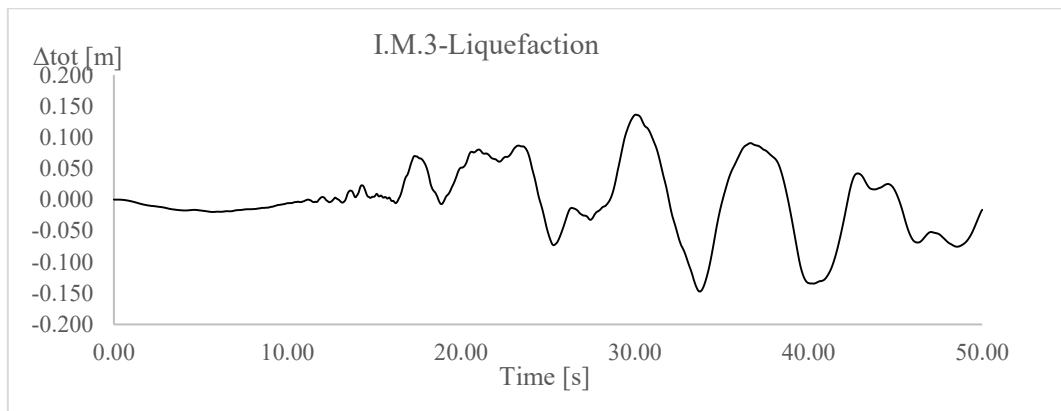


Figure 5.25 –Liquefaction: Total displacement registered for Input Motion 3 (I.M.3).

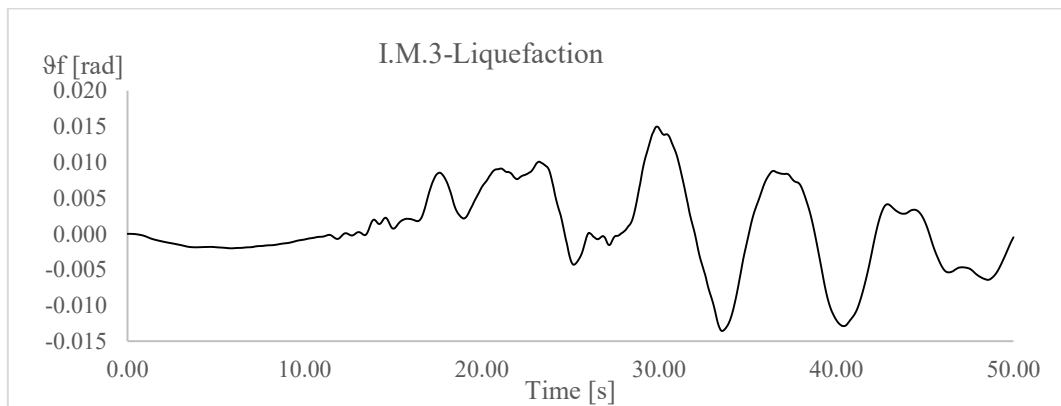


Figure 5.26 –Liquefaction: Foundation rotation registered for Input Motion 3 (I.M.3).

Parameters	Liquefaction			
	Push-over	I.M.1	I.M.2	I.M.3
$ \theta_f $ [rad]	0.015	0.009	0.011	0.0147
$ \Delta_{tot} $ [m]	0.183	0.124	0.135	0.149
T_e [s]	2.69	-	-	-

Table 28 – Push-over vs. Dynamic analyses results.

Parameters	Push-over	Percentage difference	Percentage difference	Percentage difference
		I.M.1	I.M.2	I.M.3
$ \vartheta_f [\text{rad}]$	0.015	-40%	-26%	-2%
$ \Delta_{\text{tot}} [\text{m}]$	0.183	-32%	-26%	18%

Table 29 – Push-over vs. Dynamic analyses percentage differences.

The resulting data in Table 28 show a slight overestimation in the equivalent response deformations (an average value of about 23%) from the push-over analyses with respect to the dynamic analyses results. It suggests that the presence of the liquefied layer induces an additional shaking energy dissipation. In fact, the surface response spectra show a lower response than the non-liquefied response, however, this reduction in seismic demand due to the site response was not accounted for in the displacement-based assessment procedure. What has been said could justify the lower values from the dynamic analyses and the site response analysis should be considered in the further development of a displacement-based assessment procedure for liquefiable soils, as the liquefiable layer could provide a kind of ‘base isolation’ to the building.

Comparison between the no liquefaction and the liquefaction cases

The displacement and rotation plots from the two cases of investigation show an evident difference in the oscillation periods, lengthened in liquefaction case (see the example in Figure 5.27 for ground motion I.M.1).

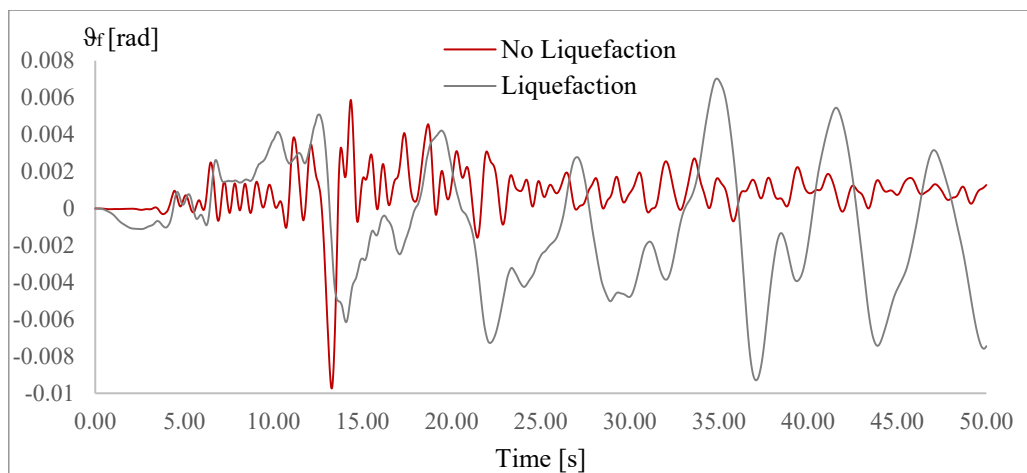


Figure 5.27 – Example of foundation rotation demonstrating the period change from No Liquefaction case to Liquefaction case.

It suggests that liquefaction and the correspondent reduction in stiffness produces a change in the natural period of the SFS system and thus in the predominant frequency. The input motion displacement spectra at a damping level of 5 % were plotted against the resulting site spectra and compared in Figure 5.28; moreover, the reduced elastic design spectrum built on the basis of the resulting parameters from the DBA, displacement-based assessment procedure is presented together with the no reduced one.

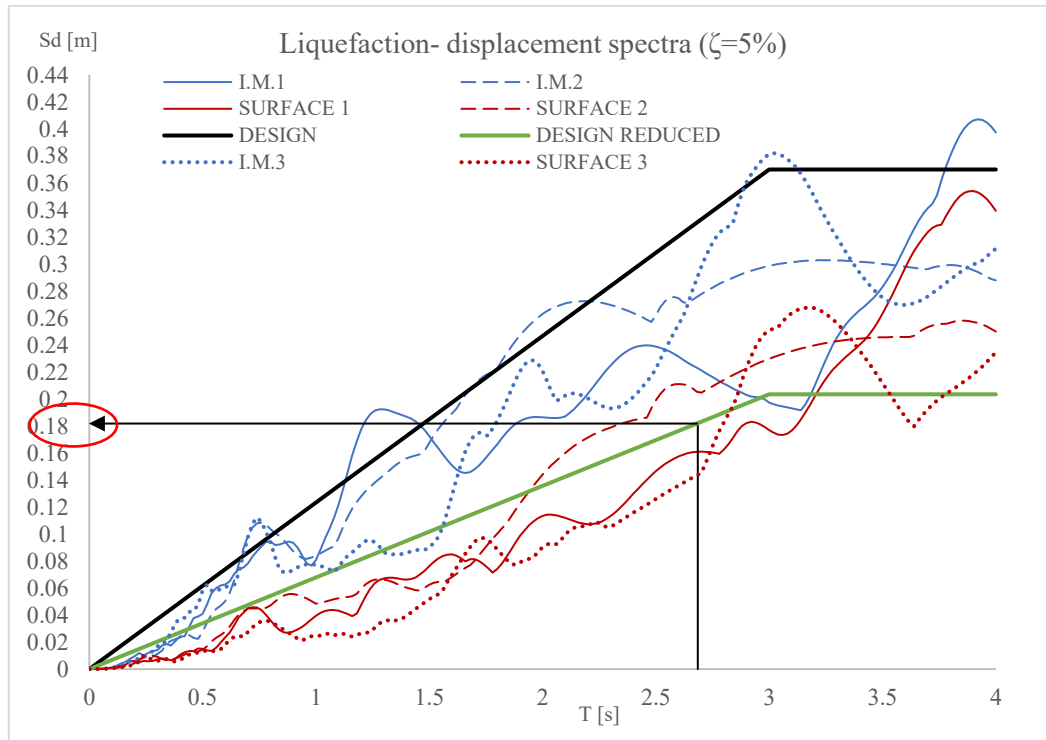


Figure 5.28 – Liquefaction: Elastic bedrock and site response displacement spectra at $\zeta=5\%$ vs. design spectra.

In contrast with the response spectra obtained from No Liquefaction case, the spectral displacements in Liquefaction case are de-amplified in the considered period interval, meaning the additional increase in damping in the liquefied layer. Looking at the design spectra, the reduced design spectral displacements should be lower, in consistency with what was obtained for the No liquefaction case. It means that the determined displacement reduction factors (DRF) in the analytical procedure explained in the previous section are overestimated in this specific case; it was expected because the DRF have been calibrated for non-liquefiable soils thus, they do not account for the additional energy dissipation in liquefaction. Moreover, the design site spectral acceleration, $S_a(T)$ used for the computation of the design spectral displacements, $S_d(T)$, referred to a site where the mean

value of the shear wave velocity was the one calculated in the homogeneous deposit (No Liquefaction case) without considering a decrease due to liquefaction that consequently affects the value of the site spectral acceleration.

Nevertheless, it could represent a benefit from the design point of view because the displacements would be computed in favour of safety.

5.7 Conclusions

The above case study demonstrates the key benefits and current shortfalls of the use of moment-rotation curves for the assessment of buildings on liquefiable soil. As for soils not susceptible to liquefaction, the push-over analysis through numerical simulations represents a good and simplified way to assess the response of structures to seismic loading in place of seismic analyses through time-histories simulations, often very complex. The consistent results with effective stress time history analyses warrant the further development of this approach, including a parametric study helpful to understand how the soil parameters, the layers thickness and the water level together with the shaking parameters influence the superstructure response.

6. Chapter: Final conclusions

In this thesis, a study related to the numerical modelling of liquefaction induced effects on shallow foundations, with a focus on the foundation rotational behaviour was performed.

After a state-of-the-art review about the topic, a first study was carried out based on bearing capacity problems solved both through finite element analyses and analytical formulations, available in literature. The aim was to validate the soil-foundation numerical models in the finite element code PLAXIS 2D, especially in the case of layered soil deposits characterised by a lower liquefiable layer below a surface crust. Moreover, simplified assumptions were taken into account to simulate the degraded strength and stiffness typical of granular saturated soils involved in the liquefaction phenomena. This is a difficult process as it is still difficult to quantify the excess pore-pressure build up and the consequent loss of shearing resistance and stiffness during seismic loading. This is a topic still object of study in this field of research.

A simplified parametric study was developed by changing the material properties and thickness of the upper layer (named the “crust”) in a 2-layered deposit model together with the foundation size, showing excellent agreement between the numerical results and the analytical solutions.

The quantification of the maximum tolerable applied vertical load on the foundation was also helpful for the main purpose of this thesis, the evaluation of moment-rotation response of shallow foundations on deposits susceptible to liquefaction.

A set of pseudo static push-over analyses were, then, performed with PLAXIS 2D with the scope to understand and quantify the cyclic response and the soil-foundation-structure system behaviour. Starting from the execution of numerical analyses involving homogeneous cohesive soils and homogeneous frictional soils, the moment-rotation response of a unit width shallow foundation was determined together with the estimation of the rotational stiffness degradation due to the increase in the applied moment until the ultimate condition was achieved. Subsequently a study dealing with a 2-layered soil deposits with a lower partially or totally liquefied layer was carried out. In these mentioned pseudo static push-over analyses simplified assumptions about the development of liquefaction during cyclic loading were considered, modelling the lower layer material with reduced strength and stiffness parameters, as well as in the bearing

capacity problems, in proportion with an increase of the excess pore pressure ratio, r_u . A parametric study was then performed changing the stiffer upper layer thickness and the crust material, together with the level of liquefaction developed in the lower layer.

It was concluded that:

- The moment-rotation response of shallow foundations on liquefiable soils is highly influenced by the mechanical properties and the thickness of the upper layer, named “crust”; for instance, for a certain foundation width, by doubling the crust thickness the deposit bearing capacity and the ultimate moment capacity increase moving towards values typical of a deposit characterised by a homogeneous soil with the crust properties. This is due to the stress bulb in correspondence of eminent foundation overturning being small enough to rest within the upper stiffer layer without mobilising the lower layer bearing capacity. As long as the foundation contact area reduces, meaning an increase of the vertical load-associated factor of safety, the ultimate moment capacity is governed by the crust properties, even with increasing liquefaction extent.
- Through the numerical results about the moment-rotation response it was found out that the ultimate moment capacity could be properly estimated through the Deng et al. (2014) contact area-based formulation (see Equation 4.5) or in cases where the crust is sufficient the equation based on the factor of safety (Equation 4.7, Deng and Kutter, 2012) and using only the crust properties assuming non-degradation in lower layers.
- The plots of the rotational stiffness degradation for different load conditions (factors of safety) show how the behaviour after the uplift initiation is influenced by the material mechanical features; in particular, the models dealing with a sandy crust produce rotational stiffness degradation curves where the uplift point is less evident than in the case of clayey crust, and the stiffness decay is more accentuated. Moreover, it was observed that the increase of the vertical applied load led to a reduction in rotational uplift, hindering the foundation detachment from the soil surface.

The combination of different actions (vertical load and tilting moment), their intensity and the material properties, together with the stiffer upper layer thickness make a normalisation of the degraded rotational stiffness curves very difficult to achieve through a common solution. The results obtained in this thesis with simplified soil models and foundation geometry, represent a reference point for exploring the

mechanism of the problem. Further research and a wider parametric study is required based on the change of the crust thickness, foundation size, number of layers involved and intermediate levels of liquefaction between the $V_{s,1}/V_{s,liq}$ of 4 and $V_{s,1}/V_{s,liq}$ of 10. Moreover, an accurate study focused on the quantification of the excess pore pressure build-up during cyclic loading would represent a helpful way to model the level of liquefaction in a soil layer; the current assumptions were only a qualitative estimation of the stiffness and strength of the liquefied soil.

Normalisation of the rotational stiffness curves by the numerical initial rotational stiffness and the numerical uplift rotation is fairly well achieved in many cases, providing a useful starting point for the validation of more complex analyses and for the achievement of a common analytical solution to use in design and assessment procedures.

Finally, the consistency in the results between the static push-over analyses and the seismic time-history numerical simulations was demonstrated. In particular a displacement-based procedure was followed to assess the response of a shallow founded bridge on a layered deposit, susceptible and not to liquefaction. The superstructure deformations and the foundation rotation, were estimated both through the pseudo-static push over analyses and the dynamic simulations, providing a significative agreement in the results, including the case of liquefaction. The few differences in the results of the global superstructure deformation are possibly related to the large number of variables in play, as explained before, together with parameters like the displacement reduction factor (DRF defined in Equation 5.3) accounting for all the possible mechanisms involved in the global system response. In fact, the mentioned parameters used in the procedure were previously validated only for non-liquefiable soils, meaning that the liquefaction induces further mechanisms that need to be modelled with a new factor. However, the current results show that the use of simplified numerical approaches to assess the structure behaviour on a liquefiable deposit during shaking, can provide reasonable estimations of the response and justify the further development of the displacement-based procedures to help engineers interpret complex dynamic simulations.

7. References

- Been, K. and Jefferies, M. (1985). A state parameter for sands. *Géotechnique*, 35(2): 99–112. <https://doi.org/10.1680/geot.1985.35.2.99>.
- Bouckovalas, G. (2017). Performance-based design of bridge piers in liquefiable sites with shallow foundation and limited ground improvement. *The 3rd International Conference on Performance Based Design (PBD-III)*, (1994).
- Bray, J. D., & Dashti, S. (2010). Liquefaction-induced movements of buildings with shallow foundations. *Fifth International Conference on Recent Advances in Geotechnical Earthquake Engineering and Soil Dynamics*.
- Chatzigogos, C.T., Figini, R., Pecker, A. and Salenċon, J. (2011). A macro-element formulation for shallow foundations on cohesive and frictional soils. *International Journal for Numerical and Analytical Methods in Geomechanics*, 35(8):902–931. DOI: 10.1002/nag.934.
- Dashti S. and Bray J.D. (2013). Numerical Simulation of Building Response on Liquefiable Sand. *Journal of Geotechnical and Geoenvironmental Engineering*, 139(8): 1235-1249.
- Deng, L. and Kutter, B. L. (2012). Characterization of rocking shallow foundations using centrifuge model tests. *Earthquake Engineering and Structural Dynamics*, 41(5):1043–1060. DOI: 10.1002/eqe.1181.
- Deng, L., Kutter, B. L. and Kunnath, S. K. (2014). Seismic Design of Rocking Shallow Foundations: Displacement-Based Methodology. *Journal of Bridge Engineering*, 19(11):04014043–11. DOI: 10.1061/(ASCE)BE.1943.5592.0000616.
- Gajan, S., Kutter, B. L., Phalen, J. D., Hutchinson, T. C., and Martin, G. R. (2005). Centrifuge modeling of load-deformation behavior of rocking shallow foundations. *Soil Dynamics and Earthquake Engineering*, 25(7-10):773–783. DOI: 10.1016/j.soildyn.2004.11.019.
- Gazetas, B. G. (1992). Formulas and charts for impedances of surface and embedded foundations.
- Gazetas G., Anastasopoulos I., Adamidis O., Kontoroupi Th. “Nonlinear Rocking Stiffness of Foundations”, *Soil Dynamics & Earthquake Engineering*, Vol. 47, pp.83-91, 2013.
- Ishihara, K. (1993). Liquefaction and flow failure during earthquakes. *Géotechnique*, 43(3): 351–451. <https://doi.org/10.1680/geot.1993.43.3.351>.
- Karamitros, D.K., Bouckovalas, G.D. and Chaloulos, Y.K. (2013b). Numerical analysis of liquefaction-induced bearing capacity degradation of shallow foundations on a two-layered soil profile. *Soil Dynamics and Earthquake Engineering*, 44:90-101.

- Karamitros, D.K., Bouckovalas, G.D. and Chaloulos, Y.K. (2013c). Seismic settlements of shallow foundations on liquefiable soil with a clay crust. *Soil Dynamics and Earthquake Engineering*, 46:64-76.
- Karimi, Z. and Dashti, S. (2016). Seismic performance of shallow founded structures on liquefiable ground: validation of numerical simulations using centrifuge experiments. *Journal of Geotechnical Geoenvironment Engineering* 142(6): 13 pp.
- Karatzia, X., Mylonakis, G., & Bouckovalas, G. (2017). 3D Dynamic Impedances of Surface Footings on Liquefiable Soil: Equivalent Linear Approach. *16th World Conference on Earthquake Engineering*.
- Kramer, S. L. (1996). *Geotechnical Earthquake Engineering*. Prentice Hall, 1 edition, ISBN: 0133749436.
- Kramer, S. L. and Wang, C.-H. (2015). Empirical Model for Estimation of the Residual Strength of Liquefied Soil. *Journal of Geotechnical and Geoenvironmental Engineering*, 141(9):04015038–15, DOI: 10.1061/(ASCE)GT.1943- 5606.0001317.
- Kramer, S. L., Sideras, S. S., & Green, M. W. (2016). The timing of liquefaction and its utility in liquefaction hazard evaluation. *Journal of Geotechnical and Geoenvironmental Engineering*.
- Lade, P.V. (1999) Instability of granular materials. In *Physics and Mechanics of Soil Liquefaction* (eds. P.V. Lade and J.A. Yamamuro).
- May, R. (2015). The Seismic Design of Shallow Foundations: A State of the Art Exploration. *Earthquakes Risk and Engineering towards a Resilient World, 9-10 July, Cambridge*, (July).
- Meyerhof, G.G. and Hanna, A.M. (1978). Ultimate bearing capacity of foundations on layered soils under inclined load. *Canadian Geotechnical Journal*, 15(4): 565-572.
- May, R. (2015). The Seismic Design of Shallow Foundations: A State of the Art Exploration. *Earthquakes Risk and Engineering towards a Resilient World, 9-10 July, Cambridge*, (July).
- Millen, M. D. L., Pampanin, S., Cubrinovski, M. and Carr, A. J. (2016). A performance assessment procedure for existing buildings considering foundation deformations. In 2016 NZSEE Conference: pp 1–8.
- Millen, M. D. L., Pampanin, S., & Cubrinovski, M. (2018). Displacement-based design of soil-foundation-structure systems. *Proceedings of the Institution of Civil Engineers - Geotechnical Engineering*.
- Mylonakis, G., Nikolaou, S., & Gazetas, G. (2006). Footings under seismic loading: Analysis and design issues with emphasis on bridge foundations, 26, 824–853. <https://doi.org/10.1016/j.soildyn.2005.12.005>

- Paolucci, R., Figini, R., & Petrini, L. (2013). Introducing dynamic nonlinear soil-foundation-structure interaction effects in displacement-based seismic design.
- PLAXIS 2D (2017) Material Models Manual. Information available on <https://www.plaxis.com>.
- PLAXIS 2D (2017) Reference Manual. Information available on <https://www.plaxis.com>.
- Robertson, P. K. (2009a). Evaluation of flow liquefaction and liquefied strength using the cone penetration test. *Journal of Geotechnical and Geoenvironmental*. [http://doi.org/10.1061/\(ASCE\)GT.1943-5606.0000286](http://doi.org/10.1061/(ASCE)GT.1943-5606.0000286).
- Schanz, T., & Vermeer, P. A. (1998). On the Stiffness of Sands. *Pre-Failure Deformation Behaviour of Geomaterials*.
- Shahir, H. and Pak, A. (2010). Estimating liquefaction-induced settlement of shallow foundations by numerical approach. *Computers and Geotechnics*, 37(3):267–279, DOI: 10.1016/j.compgeo.2009.10.001.
- Vesic, A. S. (1973). Analysis of ultimate loads of shallow foundations. *Journal of the soil mechanics and foundations division*.
- Viana da Fonseca, A. & Soares, S. M. da C. (2014). Critical state soil mechanics assessment of instability and liquefaction locus of a sandy soil from Coimbra, *VII Congresso Luso-Brasileiro de Geotecnia* (www.cobramseg2014.com.br), CD, Ref. 4469, Goiânia, GO, Brasil.
- Viana da Fonseca, A., Millen, M., Gómez-Martínez, F., Romão, X., Quintero, J., Gómez, F., Costa, P., Rios, S., Kosič, M., Dolšek, M., Logar, J., Oztoprak, S. Bozbey, I., Kelesoglu, K., Ozcep, F., Flora, A., Rasulo, A., Modoni, G., Croce, P. (2017). State of the art review of numerical modelling strategies to simulate liquefaction-induced structural damage and of uncertain/random factors on the behaviour of liquefiable soils. Deliverable D3.1 of the European H2020 LIQUEFACT research project. October 2017, www.liquefact.eu
- Youd, T. L., Idriss, I. M., Andrus, R. D., Arango, I., Castro, G., Christian, J. T., Dobry, R., Finn, L., Harder, L. F. J., Hynes, M. E., Ishihara, K., Mitchell, J. K., Moriwaki, Y., Power, M. S., Robertson, P. K., Seed, R. B. and Stokoe, K. H. (2001). Liquefaction resistance of soils: summary report from the 1996 NCEER and 1998 NCEER/NSF workshops on evaluation of liquefaction resistance of soils. *Journal of Geotechnical and Geoenvironmental Engineering*, pages 1–17.

Figures

Figure 2.1- (a) Liquefaction induced rigid tilting after 1964 Niigata earthquake; (b) Liquefaction in a residential area of Christchurch, from Diaz, 2016; (c) 5-storey building tilting after Adapazari earthquake, Turkey, from Bray et al., 2001.	9
Figure 3.1- Continuous foundation on layered soil: stronger over weaker.	25
Figure 3.2- Variation of K_s with ϕ_1 and q_2/q_1	26
Figure 3.3 – Right and wrong geometry of the mesh at the foundation contour.	30
Figure 3.4- Numerical model of the soil-foundation system $H=6$ meters.	31
Figure 3.5- Numerical model of the soil-foundation system $H=10$ meters.	31
Figure 3.6- Numerical model of the soil-foundation system $H=14$ meters.	31
Figure 3.7- Load-displacement response for different geometries of the FE model.	33
Figure 3.8- Load-displacement response in a clayey soil vs Analytical elastic stiffness.	35
Figure 3.9- Load-displacement response in a sandy soil (Foundation width=4 m).	36
Figure 3.10 – Non-liquefied and liquefied soil behaviour.	38
Figure 3.11 – Example of the assumed equivalent liquefied behaviour.	39
Figure 3.12- Numerical model of the layered deposit. H crust=1,5 meters.	40
Figure 3.13- Numerical model of the layered deposit. H crust=3 meters.	40
Figure 3.14- Load-displacements curve for two layered deposits with liquefied layers.	42
Figure 4.1- Mechanisms of foundation rotations.	45
Figure 4.2- Cross section of the problem.	46
Figure 4.3- Forces and displacements for the macroelement model (adapted from Chatzigogos, 2011).	48
Figure 4.4 – (a) Output of the numerical analysis; (b) State of stress below the foundation.	55
Figure 4.5- Moment-rotation behaviour and theoretical uplift value.	55
Figure 4.6 – Moment-rotation response of a shallow foundation on a linear elastic half-space.	56
Figure 4.7 – Verification of the footing flexural rigidity.	57
Figure 4.8 – Comparison between numerical results and analytical solution.	58
Figure 4.9- Moment-rotation response of a strip footing on a cohesive soil.	63
Figure 4.10- Moment-rotation response of a strip footing on a cohesive soil.	63
Figure 4.11- Rotational stiffness vs. rotation curves.	64

Figure 4.12- Normalised rotational stiffness vs. normalised angle of rotation.	65
Figure 4.13- Inelastic response (FS=20) vs. Elastic response.	66
Figure 4.14- Moment-rotation response of a strip footing on a purely frictional soil....	70
Figure 4.15- Rotational stiffness vs. rotation curves for homogenous sandy soil.....	71
Figure 4.16- Normalised rotational stiffness vs. normalised angle of rotation.	72
Figure 4.17- Normalised rotational stiffness by the analytical elastic stiffness vs. normalised angle of rotation.	73
Figure 4.18- Comparison between clay and sand rotational stiffness degradation.	74
Figure 4.19- Flow chart of the procedure followed in the 2-layered deposit.	76
Figure 4.20- Comparison between homogeneous deposit and layered deposit.....	79
Figure 4.21 - Moment-rotation response of a strip footing on a 2-layered deposit.....	83
Figure 4.22- Rotational stiffness vs. rotation curves.	84
Figure 4.23- Normalised rotational stiffness vs. normalised angle of rotation.	85
Figure 4.24 - Moment-rotation response of a strip footing on a 2-layered deposit.....	86
Figure 4.25 – Comparison between $M-\theta_f$ in the homogeneous sand deposit with $M-\theta_f$ in layered deposit with $H_{crust}=3$ m and $V_{s1}/V_{sliq}=4$	87
Figure 4.26- Rotational stiffness vs. rotation curves.	88
Figure 4.27- Normalised rotational stiffness vs. normalised angle of rotation.	88
Figure 4.28 - Moment-rotation response of a strip footing on a 2-layered deposit.....	89
Figure 4.29- Rotational stiffness vs. rotation curves.	90
Figure 4.30- Normalised rotational stiffness vs. normalised angle of rotation.	90
Figure 4.31 - Moment-rotation response of a strip footing on a 2-layered deposit.....	91
Figure 4.32- Rotational stiffness vs. rotation curves.	92
Figure 4.33- Normalised rotational stiffness vs. normalised angle of rotation.	92
Figure 4.34 - Moment-rotation response of a strip footing on a 2-layered deposit.....	93
Figure 4.35- Rotational stiffness vs. rotation curves.	93
Figure 4.36- Normalised rotational stiffness vs. normalised angle of rotation.	94
Figure 4.37 - Moment-rotation response of a strip footing on a 2-layered deposit.....	94
Figure 4.38- Rotational stiffness vs. rotation curves.	95
Figure 4.39- Normalised rotational stiffness vs. normalised angle of rotation.	95
Figure 5.1- Geometry of the problem.	100
Figure 5.2 – Elastic site design spectrum.	101
Figure 5.3 – Estimation of the foundation rotation from the $M-\theta$ curves.	104
Figure 5.4 – Liquefied soil behaviour.	110
	141

Figure 5.5 – Assumed equivalent liquefied behaviour.	110
Figure 5.6- Numerical model.....	113
Figure 5.7- Queried points for rotation calculation.	114
Figure 5.8 – Moment-rotation responses of the shallow founded building.....	115
Figure 5.9-Time-history of Input Motion 1 (I.M.1).	116
Figure 5.10- Time-history of Input Motion 2 (I.M.2).	116
Figure 5.11- Time-history of Input Motion 3 (I.M.3).	116
Figure 5.12- Elastic response displacement spectra at $\zeta=5\%$	117
Figure 5.13 –Stiffness-strain behaviour of soil (Seed and Idriss, 1991).	119
Figure 5.14 – No Liquefaction: Building total displacement registered for Input Motion 1 (I.M.1).....	124
Figure 5.15 – No Liquefaction: Foundation rotation registered for Input Motion 1 (I.M.1).	124
Figure 5.16 – No Liquefaction: Building total displacement registered for Input Motion 2 (I.M.2).....	125
Figure 5.17 – No Liquefaction: Foundation rotation registered for Input Motion 2 (I.M.2).	125
Figure 5.18 – No Liquefaction: Building total displacement registered for Input Motion 3 (I.M.3).....	125
Figure 5.19 – No Liquefaction: Foundation rotation registered for Input Motion 3 (I.M.3).	126
Figure 5.20 – No Liquefaction: Elastic bedrock and site response displacement spectra at $\zeta=5\%$ vs. design spectra.....	127
Figure 5.21 – Liquefaction: Total displacement registered for Input Motion 1 (I.M.1).	128
Figure 5.22 –Liquefaction: Foundation rotation registered for Input Motion 1 (I.M.1).	128
Figure 5.23 –Liquefaction: Total displacement registered for Input Motion 2 (I.M.2).	128
Figure 5.24 –Liquefaction: Foundation rotation registered for Input Motion 2 (I.M.2).	129
Figure 5.25 –Liquefaction: Total displacement registered for Input Motion 3 (I.M.3).	129

Figure 5.26 –Liquefaction: Foundation rotation registered for Input Motion 3 (I.M.3).
..... 129

Figure 5.27 – Example of foundation rotation demonstrating the period change from No
Liquefaction case to Liquefaction case. 130

Figure 5.28 – Liquefaction: Elastic bedrock and site response displacement spectra at
 $\zeta=5\%$ vs. design spectra..... 131

Tables

Table 1 – Footing features.	27
Table 2 – Materials properties.	28
Table 3 – Analytical and numerical solutions for $H_{crust}= 1,5$ meters.	41
Table 4 – Analytical and numerical solutions for $H_{crust}= 3$ meters.	41
Table 5 – Soil input parameters.	52
Table 6 – Soil/foundation interface input parameters.	53
Table 7- Cohesive soil input parameters.	60
Table 8 – Input parameters for the foundation loads.	61
Table 9 – Frictional soil input parameters in PLAXIS 2D.	68
Table 10 - Input parameters for the foundation loads.	69
Table 11- Input material parameters of the lower liquefied layer.	77
Table 12- Input parameters for the foundation loads in Stiff sand over partially liquefied layer deposit ($H_{crust}=1,5$ m).....	80
Table 13- Input parameters for the foundation loads in Stiff sand over partially liquefied layer deposit ($H_{crust}=3$ m).....	80
Table 14- Input parameters for the foundation loads in Stiff sand over totally liquefied layer deposit ($H_{crust}=1,5$ m).....	80
Table 15- Input parameters for the foundation loads in Stiff sand over totally liquefied layer deposit.....	81
Table 16-Input parameters for the foundation loads in stiff clay over partially liq. layer deposit ($H_{crust}=1,5$ m).	81
Table 17- Input parameters for the foundation loads in stiff clay over totally liq. layer deposit ($H_{crust}=1,5$ m).	81
Table 18-Soil deposit and rock properties.	102
Table 19-Building properties.....	102
Table 20 – Simplified DBA procedure results for the estimation of the building response.	106
Table 21-Soil parameters for HS model.	108
Table 22- Input parameters for HS model in the liquefied layer (Layer 2).....	111
Table 23- Ultimate capacity values.	112
Table 24 - UBC3D-PLM Soil Model Parameters.	121

Table 25 – Input parameters for Rayleigh coefficients determination (I.M. is for Input Motion).....	122
Table 26 – Push-over vs. Dynamic analyses results.....	126
Table 27 – Push-over vs. Dynamic analyses percentage differences.....	126
Table 28 – Push-over vs. Dynamic analyses results.....	129
Table 29 – Push-over vs. Dynamic analyses percentage differences.....	130

Ringraziamenti

Ringrazio i miei genitori per tutto il supporto dato e per quello che continueranno a darmi nel raggiungimento e superamento dei miei obiettivi, per aver sempre soddisfatto le mie esigenze e per non avermi fatto mancare mai niente.

Ringrazio la mia famiglia, i miei zii e cugini per l'affetto, la generosità e la costante disponibilità.

Ringrazio i miei bellissimi e intelligentissimi nipoti, che ormai hanno le capacità per leggere, augurando loro tantissimi successi e una vita piena di gioie.

Ringrazio Vincenzo per tutto l'amore che mi offre, per essere la mia spalla, il mio braccio ma soprattutto il mio cuore, per la generosità incondizionata e per essere il miglior compagno di viaggio che si possa avere.

Ringrazio Carmen, ormai sorella, per il bene che mi offre da tutta la vita, nonostante migliaia di chilometri di distanza e non troppi pixel a disposizione.

Ringrazio Anna, un'amica sincera, un punto fermo su cui poter contare e grande esempio di maturità e responsabilità.

Ringrazio Peppe e Gimmy, due amici tanto strani quanto fidati, per tutto il bene che mi offrono nonostante i lunghi periodi di assenza, ma soprattutto per i meravigliosi racconti che narrano periodicamente.

Ringrazio i miei compagni di viaggio, Giuliana, Federica, Federica, Antonio, Giuseppe e Paolo per aver condiviso tutte le avventure e aver reso le disavventure meno difficili da affrontare.

Ringrazio Ilenia e Isa per essere state le coinquiline migliori che potessi desiderare, per l'armonia e la continua accoglienza e disponibilità.

